Impurities in Silicon Nanocrystals: The intentional and the inherent

A DISSERTATION
SUBMITTED TO THE FACULTY OF THE GRADUATE SCHOOL
OF THE UNIVERSITY OF MINNESOTA
BY

David J. Rowe

IN PARTIAL FULFILLMENT OF THE REQUIREMENTS
FOR THE DEGREE OF
DOCTOR OF PHILOSOPHY

Prof. Uwe R. Kortshagen, Adviser

April 2013

ACKNOWLEDGEMENTS

Without the effort of an uncountable amount of people, this research would not have been possible. Despite not having the words to thank everyone as properly and eloquently as I would like, please know that I deeply appreciate everything which was done for me throughout the course of my education.

To Rebecca Anthony, Tyson Baldridge, Adam and Abby Boies, Brian and Ariel Chatman-Kleczewski, Greg Cibuzar, Ross Cram, Travis Daul, Holly Edgett, Mark Erickson, Prof. Harold Evensen, Federico Galli, John Gardner, Prof. Steven Girshick, Ryan Gresback, Lissy Gorning, Bob Hafner, Prof. Joachim Heberlein, Zak Holman, Dave Hultman, Robert Jones, Nic Kramer, Rob and Kim Krsek, Jake and Chelsea Leachman, Mike Leveille, Rick Liptak, Chin-Yi Liu, Meenakshi Mamunuru, Mike Manno, Ryan Mello, Karon Mooney, Gary Olin, Prof. Steven Penoncello, Prof. Rui Pereira, DartKen Poon, Andy and Shannon Reyment, Jason Trask, Lance Wheeler, Katie Wanie, Lee Wienkes, Jeslin Wu, and Pete Zimmerman, thank you for surrounding me with people who made my life so much easier than it needed to be.

To the students and post-docs of Prof. Kortshagen's group, HTPL, and MRSEC IRG-4, thank you for providing me with an outlet to learn more while simultaneously teach more.

To my thesis committee, Prof. Chris Hogan, Prof. Traian Dumitrica, and Prof. Steven Campbell, thank you for your support, guidance, and willingness to accept the challenge of reading this lengthy document.

To Prof. Uwe Kortshagen, thank you for turning me into a successful scientist despite my fervent attempts to resist. I feel I may never truly realize the effort you gave towards this.

To Mom and Dad, Lorra, Scott, and Judy, thank you for helping me to become someone that I'm proud to be. Without your support I wouldn't be where I am today. And to the new additions to my family, Steve, Tina, Helen, Lonna, Butch, Erin, Carly, Shane, and Tyler, thank you for accepting me into your lives despite the fact that I was a graduate student.

To my nieces, Paige, Lydia, and Katy, thank you for reminding me I'm part of a world bigger than that enclosed by my laboratory walls. I hope I'll be able to repay you when the time comes.

And finally, to my remarkably intelligent and beautiful wife, Sarah, who deserves more gratitude than I can ever express. Your versatility continues to amaze me. You've been my life coach, therapist, enabler, best friend, dining partner, counselor, social advisor, leader, sidekick, equal, travel companion, proof-reader, copy editor, and sounding board. I am unfathomably lucky to have you by my side.

ABSTRACT

Silicon nanocrystals (SiNCs) have become an important class of materials in the fields of photovoltaics, thermoelectrics, lighting, and medicine. Impurities within SiNCs dramatically alter the electrical and optical properties of the host material, whether the impurity is intentionally added in an attempt to manipulate properties, or is inherent to the material and its natural state. Despite such remarkable changes, impurity incorporation within SiNCs remains poorly understood, since concepts applied to understanding impurities in bulk materials may not completely translate to nanomaterials. Understanding the effect of SiNC impurities requires new technologies to produce materials suitable for study combined with new insights to expound the differences in the nanoscale physics. Nonthermal plasma-assisted gas-phase synthesis provides an excellent route to producing and investigating impurities within SiNCs due to the unique chemical reaction environment of the plasma. The robustness of such a technique allows for the production of very pure SiNCs or SiNCs with added impurities simply by adding different chemicals to the plasma. The chapters in this document focus on the effect that different impurities have on the properties of SiNCs. Chapter 2 focuses on heavily P-doped SiNCs exhibiting the first known observation of a unique electrical and optical property known as localized surface plasmon resonance (LSPR) within free-standing SiNCs. Chapter 3 explains the synthesis of B- and P-doped SiGeNC alloys and their deposition into thin films for thermoelectric applications. Chapter 4 highlights research which uses P-doped SiNCs to form emitter layers for pn-junction type solar cells, including device fabrication and optical characterization. Chapter 5 examines *inherent* impurities in the form of dangling bond defects which may be responsible for the quenching of SiNC photoluminescence, and their evolution during the process of air-ambient oxidation. Several appendices at the end of the document detail some of the fabrication processes used throughout this work, as well as brief reports of some side projects that may be of interest to researchers intent on studying SiNC synthesis and deposition technologies.

TABLE OF CONTENTS

LIST OF TABLES

LIST OF FIGURES

1. *IMPURITIES IN SILICON NANOCRYSTALS – A BRIEF INTRODUCTION*

1.1. IMPURITIES AND SEMICONDUCTOR NANOCRYSTALS

Semiconductors, by their very nature, are remarkable materials, exhibiting conductive properties like a metal, but also nonconductive properties like an insulator. The unique material properties of semiconductors have made them the foundation of modern electronics, enabling transistors, diodes, microprocessors, lasers, solar cells, radios, telephones, and computers. One of the most common semiconductors in the world is silicon. Silicon (Si) has become the basis for almost all microelectronic devices and the production of Si wafers sustained a $10.3B industry in 2011.[1] Crystalline Si holds 80-90% of the market share in photovoltaics,[2] despite its large optical absorption length compared to other semiconductors which allow for thinner absorbing layers. The *prosperity* of Si in industry is in large part due to a natural abundance of Si in the earth's crust, second only to oxygen.[3] However, the *versatility* of Si, and semiconductors in general, mainly resides in the ability to manipulate the electrical, optical, and mechanical properties through the addition of impurities. The importance of impurities depends on the fact that often a very small impurity concentration significantly affects the host material's properties.

Impurities can be categorized into two types – *intentional* impurities and *inherent* impurities. *Intentional* impurities are purposely added to a pure substance in order to precisely manipulate its properties. The addition of impurities in low concentrations is commonly known as "doping" and is one of the main reasons semiconductors are so useful in electronics due to the dramatic effect on material properties. As an example, doping Si between concentrations of 1 in 100 to 1 in 1 billion causes the electrical conductivity changes by a factor of 10^6! Alternatively, adding high concentrations of impurities may change the structure of the material, resulting in the formation of a compound known as an alloy. Alloys are usually more common in metallurgical applications; however an important semiconductor alloy for transistors and thermoelectrics is silicon-germanium. In contrast to *intentional* impurities, one can generally think of *inherent* impurities as

the innate, natural result of synthesis or long-term environmental exposure without the directed, deliberate addition of a new material. Since they are usually difficult to avoid, inherent impurities usually carry a negative, though misguided, connotation. For instance, oxygen (O) is an inherent impurity because Si oxidizes upon exposure to air, but biological applications of Si nanocrystals (SiNCs) require an oxide shell for water solubility and bio-compatibility.

In addition to impurities, semiconductor properties are dramatically affected as the size of the material is reduced to the nanoscale (1-50 nm), attributable to two main factors – one geometrical and one electrical. Considering geometry, nanoparticles consist of almost as many surface atoms as core atoms. As a result, the chemical nature of the surfaces becomes important due to the increased contribution to the nanoparticle. Simultaneously, as materials are scaled down, their dimensions begin to approach the characteristic length for electron delocalization, known as the exciton Bohr radius. Below this characteristic length, electrons begin to crowd each other, and modification to bulk energy states is required to accommodate this crowding. This effect is known as quantum confinement and results in "pure" nanoscale materials exhibiting notable differences in mechanical, electrical, and optical properties from their bulk counterparts, which can be tuned simply by adjusting the size of the particle.

As a result of the potential to exploit remarkable size-dependent properties and recent advances in microscopy and material characterization techniques, the study of semiconductor nanocrystals (NCs) has witnessed dramatic advances over the past several years. Significant attention has been devoted to Group II-VI and IV-VI compounds which are easily synthesized in liquid-phase reactions at low temperatures and produce excellent size control and small size distribution,[4] yet concerns over availability and environmental toxicity of the constituent elements inhibit the proliferation of such materials. However as mentioned before, Si is widely abundant, fairly benign, and benefits from a well-established infrastructure. In fact, recent reports suggest SiNCs as a very important nanomaterial, with focus on the remarkable optical properties such as highly-efficient photoluminescent quantum yield (PLQY),[5] multiple carrier generation[6] and multi-

exciton generation.[7] Successful application of SiNCs to devices such as lasers,[8] memory storage,[9] hybrid-organic solar cells,[10–12] and light-emitting diodes (LEDs)[13] demonstrate excellent versatility. These results have driven rapid research and as a result, SiNCs are an intensely studied material – a Scopus database search for "silicon nanocrystals" returned 1880 articles, a similar Google search returned over 122,000 results!

Despite such attention, the effect of impurities, i.e. doping, alloying, surface chemistry, is still relatively unknown for SiNCs, as well as semiconductor NCs in general. Conventional doping methods developed in the microelectronics industry, such as ion-implantation, spin-on dopants, and dopant gas diffusion, are generally designed for wafer-based materials, and the transition to nanomaterials is not straightforward. For example, dopant diffusion is usually carried out in a furnace at temperatures above 1000 °C, however, semiconductor NCs have been observed to melt, sinter, and change surface termination at temperatures much lower than this.[14,15] In addition to unforeseen effects, physically fundamental processes inhibit NC doping. Attempts to dope NCs result in a phenomenon termed "self-purification" where dopant atoms segregate to the NC surface in an effort to lower the free energy of the particle. The segregated dopant is typically electrically inactive, resulting in undoped or lowly doped NCs.[16,17] This effect is thermodynamically driven at high synthesis temperatures where chemical equilibrium occurs.[18] At lower temperatures, such as those commonly used in colloidal synthesis, kinetics limits the flux of dopant atoms to the NC surface.[19] Similarly, alloyed NCs may phase segregate into separate materials. Despite the importance of dopants located at or near the NC surface, the effect of such impurities still remains relatively unknown. "Surface doping" has been coined to describe how an impurity at the NC surface effectively changes the semiconductor's electronic properties without providing a free charge carrier as it would in a bulk semiconductor.[20]

In order to further study the effects of impurities within SiNCs, repeatable robust synthesis methods are necessary, allowing for precise control over size and composition. In 1990, luminescent SiNCs were first formed by anodically etching Si wafers to form porous,

nanostructured Si.[21] Since then, a myriad of techniques have been described for SiNCs synthesis. Solid phase formation of SiNCs via sputtering of Si-rich oxide and subsequent annealing produces SiNCs embedded in an oxide matrix with excellent surface passivation, i.e. low defect concentration. This technique has been used to study optical emission from SiNCs[22] as well as thin film SiNC pn-junction photovoltaics.[23–26] Furthermore, co-sputtering a dopant target allowed for SiNC doping at least at low dopant concentrations.[23,27–29] The success of the technique relies on the excellent surface passivation, due to the embedded nature of the material, which inhibits phase segregation of the dopant to the SiNC surface. However, a major drawback of this technique is the time required for sputtering and the high temperatures (>1000 °C) needed for NC formation. Only a few successful demonstrations of liquid-phase SiNC synthesis have been reported since the melting temperature (and thus the crystallization temperature) for Si is quite high compared to the decomposition temperatures for all known solvents used in liquid-phase reactions. Baldwin *et al.* synthesized SiNCs via Si halide reduction with sodium naphthalenide with a size distribution of 5.2 nm ± 1.9 nm.[30] Alternatively, using a solid-liquid hybrid technique via femtosecond laser ablation of a submerged Si wafer, Tan *et al.* synthesized SiNC terminated with acrylic acid with a size distribution of 1.9 nm ± 0.4 nm.[31]

On the whole however, gas-phase synthesis techniques provide more favorable SiNC synthesis routes as they accommodate for higher temperatures necessary for rapid crystallization. As a result, numerous reports outline successful gas phase SiNC synthesis techniques, such as laser pyrolysis,[32] laser photolysis,[33] thermal pyrolysis,[34] hot wire chemical vapor deposition (HW-CVD) of SiH_4,[35] laser-, photo-induced-, microwave-, and catalytic-CVD.[36–40] Nevertheless, these techniques suffer from a lack of repulsive forces between NCs during growth, in contrast to the steric repulsions found in liquid-phase synthesis. As a result, the high temperatures needed for crystallization amplify NC collisions and interactions, leading to coagulation and significant broadening of size distributions.[41]

In the last fifteen years, nonthermal plasmas emerged as a technique capable of producing high-quality semiconductor NCs in the gas-phase while avoiding some of the common drawbacks for other gas-phase synthesis techniques. In 1997 Gorla *et al.* demonstrated production of spherical SiNCs and GeNCs in the gas phase with a continuous flow, inductively-coupled radio-frequency (RF) plasma,[42] while in 2003, Bapat *et al.* reported the production of faceted SiNCs using an inductively-coupled RF plasma.[43] However, control over particle size, shape, and monodisperity remained challenging with inductively coupled plasmas due to necessarily high plasma densities.[44] As an alternative, Mangolini, Thimsen, and Kortshagen reported in 2005 of a continuous flow, *capacitively-coupled* RF plasma reactor.[45] In a capacitively coupled plasma, the plasma density can be more easily tuned offering better control of NC properties.[44]

In any plasma synthesis technique, an applied voltage ionizes a carrier gas to form an oscillating, high-energy free electron gas. A semiconductor precursor dissociates within the plasma due to energetic collisions, and chemical radicals cluster together and nucleate to form nanoparticles which may or may not crystallize. In the abovementioned schemes, argon or helium acts as the carrier gas. The plasma dissociates silane (SiH_4) gas which produces silicon-hydrogen (Si_x-H_y) radicals, in turn leading to nucleation of Si clusters. Electron-ion recombination and H-Si surface reactions occurring at the cluster-gas interface lead to large temperature spikes which crystallize the cluster.[46] From this point on, NC growth occurs slowly through coagulation and surface reactions with neutral clusters and radicals. Charging of the NCs within the plasma creates a repulsive force which reduces agglomeration and leads to narrow, Gaussian size distributions. The SiNCs typically consist of an H-terminated surface due to excess H from the SiH_4. In general, impurity doping results from adding phosphine (PH_3) or diborane (B_2H_6) gas for n- or p-type doping, respectively. Likewise, alloying can be achieved by adding germane (GeH_4) into the precursor flow stream. Recent demonstrations of this technique illustrate its robustness and versatility for synthesizing semiconductor NCs - highly luminescent SiNCs,[5] in-flight alkene-passivated SiNCs,[47] germanium NCs (GeNCs),[48] indium phosphide NCs,[49] gallium nitride NCs,[50] silicon-germanium alloy NCs (SiGeNCs),[48] and boron- and phosphorus-doped SiNCs.[51]

Several variations of this technique illustrate its technological importance and adaptability. Large scale production of SiNCs was shown possible via very-high-frequency (VHF)[52] and microwave[53] nonthermal plasma techniques. As mentioned above, dissociation and particle formation from SiH_4 and GeH_4 produce H-terminated NCs, however there is no fundamental chemical process which prohibits using other non-hydrogenated precursors for group IV NC synthesis. Halogenated precursors such as silicon tetrachloride ($SiCl_4$),[54] silicon tetrabromide ($SiBr_4$),[55] and germanium tetrachloride ($GeCl_4$)[56] have also been used to produce NCs using RF and VHF nonthermal plasmas.

1.2. General Description of NC Synthesis Technique

The reactor used in this work was modeled after the plasma assisted synthesis technique originally developed by Mangolini, Thimsen and Kortshagen in 2005.[45] The general configuration of the reactor is shown schematically in Figure 1.1, however specific alterations will be discussed in individual chapters as required. Specifically, a capacitively-coupled, nonthermal radio-frequency (RF) argon plasma dissociates hydrogenated semiconductor precursors. Table 1.1 outlines the properties of the gases used. Thermal-based mass flow controllers (MKS 1179 and MKS 1479) deliver gas flows to a manifold which pre-mixes the gases before injection into a low-thermal-expansion glass tube (1" O.D. / 0.85" I.D.) where the plasma reaction takes place. The pressure inside the reactor is measured using a convection-enhanced Pirani gauge (Granville-Phillips Convectron 275). Typical reactor pressures for NC synthesis span between 0.8-5 Torr.[1] Low pressure is achieved by a single, dual-stage rotary vane vacuum pump (Leybold D40B, Alcatel 2033, or Alcatel 2063), which evacuates the chamber to less than 10 mTorr before gas delivery. Three purge-fill cycles with nitrogen gas (N_2) minimize contamination before NC synthesis, and provide safe conditions upon which to vent the reactor to ambient during sample removal or reactor maintenance. Two copper ring electrodes placed one inch apart deliver RF

[1] A distinction should be made here between *measured pressure* and *actual pressure*. A convection enhanced Pirani gauge is used to monitor pressure in the synthesis region, which depends on the convective heat transfer coefficient of the gas. The gauge is calibrated to nitrogen but the reaction occurs under > 95% argon, so a correction was used to convert the *measured pressure* to the *actual pressure*.

power to the plasma from a 13.56 MHz 600 W power supply (Advanced Energy RFX600). A custom-modified RF antenna tuner (MFJ Enterprises 962D) provides impedance matching for the plasma reactor. Previous reports form our group explain that over 55 W is necessary to produce NCs,[57] however recent work confirms the actual power delivered to the plasma is only a fraction of the nominal power often reported in the literature.[58] Experience proves that the nominal power threshold for NC production depends on the reactor geometry and matching network electronics. Nevertheless, nominal power remains a qualitative process parameter to report. In this study, typical nominal powers ranging between 70 – 130 W produced NCs.

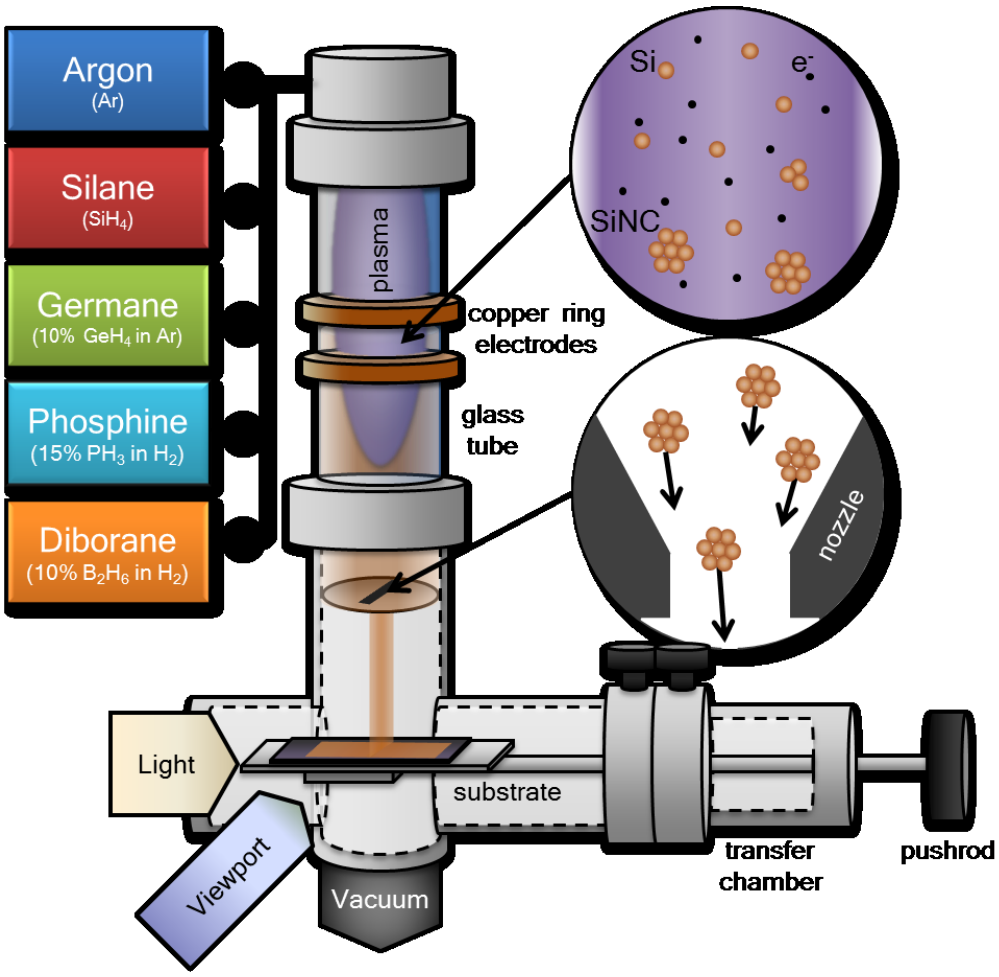

Figure 1.1. Plasma reactor schematic. Plasma-assisted, continuous flow semiconductor NC reactor and film deposition chamber, with magnified diagrams of the plasma discharge and the NC deposition nozzle.

Table 1.1. Process gases used in this work.

	Gas composition	*Structure*	*Symbol*	*Toxic Hazard*	*Fire Hazard*
Silane	100%		SiH_4	Slightly	Yes
Germane	10% in Argon	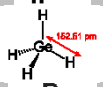	GeH_4	Yes	Yes
Phosphine	15% in Hydrogen	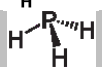	PH_3	Yes	Yes
Diborane	10% in Hydrogen	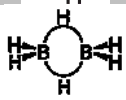	B_2H_6	Yes	Yes
Argon	100%		Ar	In high levels	No
Hydrogen	n/a		H_2	Low	Yes

In general, NCs were collected either as thin films or as powder samples using a spray-coating method, known more formally as inertial impaction. A tapered rectangular nozzle restricts the gas flow after the NC synthesis region and creates a pressure drop between the synthesis region and the deposition chamber. As gas accelerates through the nozzle, drag forces subsequently accelerate the NCs to sufficient velocity that they travel ballistically from the nozzle exit to a substrate placed 5-10 mm downstream. For powder collection, a substrate placed beneath the nozzle exit collects macroscopic amounts of NCs. For NC film deposition, a manual linear feedthrough moves the substrate through the rectangular particle beam forming a thin film comprised of interconnected NCs. The feedthrough connects to the reactor through a load-lock twin gate-valve system and retracts into a small removable chamber for air-free removal and transport. Twin gate valves allows for air-free transport of the removable chamber while maintaining reactor integrity against ambient contamination. The standoff distance from the nozzle exit to the substrate offers control over the film porosity.[59] Adjustment of the nozzle opening provides additional control of the pressure in the synthesis region. More specifically, the flow restriction created by varying nozzle sizes changes the pressure upstream of the nozzle, independent of the Ar flow rate. The NC impact velocity is large enough that NCs adhere to the substrate, however is low enough such that no NC deformation is observed. This configuration results in randomly packed spheres and provides the highest possible density of ~ 63%. The details of impaction theory are well developed, and interested readers are directed towards texts

by Hinds[41] and Friedlander[60] for rigorous treatments, as well as a recent article by Girshick outlining advanced techniques of aerosol-based nanoparticle deposition.[61] For this work, additional focus on thin film impaction can be found in Chapters 3 and 4, where device fabrication required high quality film deposition.

Lastly, several safety and design features of the reactor should be mentioned because they impose unique research constraints. Firstly, using toxic, explosive, and/or pyrophoric gases require implementation of advanced safety features. Toxic gases such as GeH_4, PH_3, and B_2H_6 are purchased as diluted mixtures, 10% in Ar, 15% in H_2, and 10% in H_2, respectively. The diluent reduces potential exposure concentrations, and in the case of hydrogen, diffuses more rapidly than other gases for quicker detection. Negative-pressure cabinets house gas cylinders, monitoring the flow and providing automatic lockout in the event of a building power failure. A pyrolizing furnace, i.e. burn-box, safely decomposes unreacted gases before exhausting the effluent. To even further reduce toxic exposure in the event of a gas leak, the entire reactor must be housed within a negative-pressure fume hood, placing limitations on the physical footprint of the reactor. Several separate reactors now share the gas lines, requiring far less reconfiguration in between experiments which in turn reduces the potential for gas leaks. Finally, a remote user interface, shown in Figure 1.2, allows for safe operation of the gas lines and pneumatic valves from outside the fume hood, minimizing the time a user could be exposed to potential leaks. The author recently developed and built this interface in collaboration with Lee Weinkes, a Ph.D. candidate from the Department of Physics, and Rick Liptak, a post-doctoral researcher from the Department of Electrical and Computer Engineering.

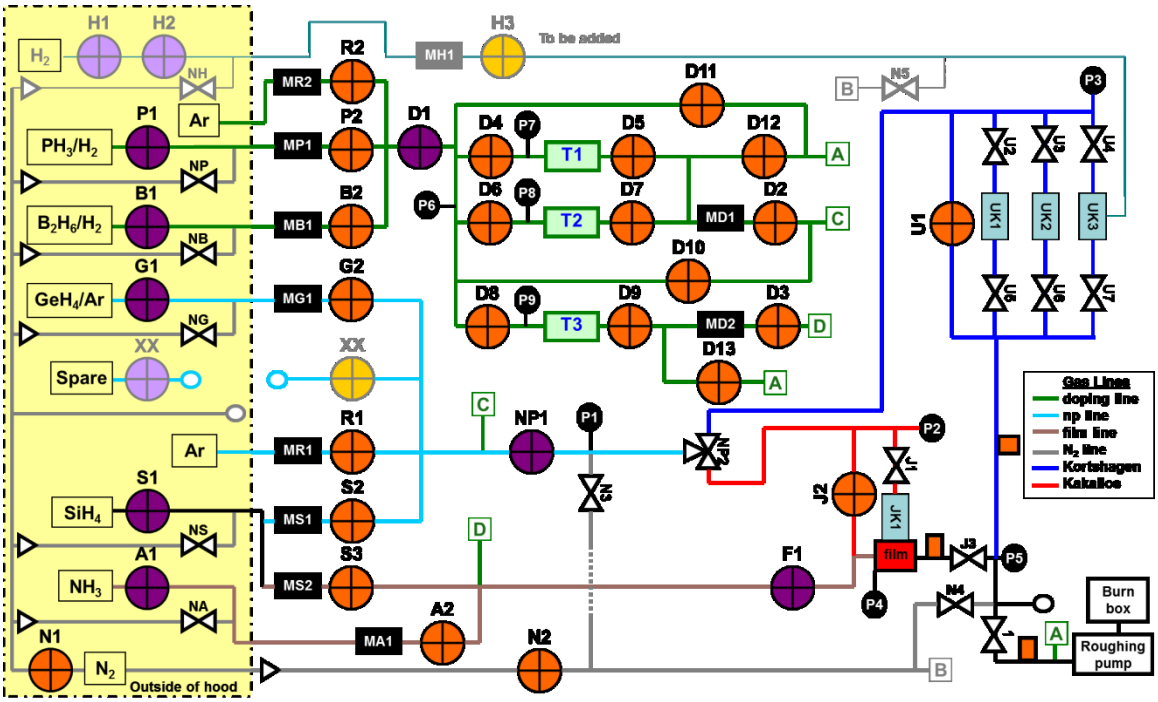

Figure 1.2. Schematic of remote user interface for re-designed NC doping system. Yellow rectangles – gas sources, crossed circles – pneumatic valves controlled by electrical switches, blue rectangles – plasma reactors, white bowties – manual valves, black rectangles – mass flow controllers, black circles – pressure gauges, green rectangles – tanks for premixing of dopants. Additional capability was accommodated for future experiments.

1.3. Document Outline

The preceding chapter has laid the foundation for this thesis by highlighting the motivation to understand semiconductor NC doping, the challenges involved in studying such material systems, and the technology employed to do so. The following chapters will each focus on a different case of impurities in SiNCs. Chapters 2-4 are centered on the *intentional* addition of impurities, either through doping, or alloying of SiNCs. Chapter 2 focuses on the synthesis and characterization of very-highly-doped SiNCs with P. Such NCs exhibit an optical property known as localized surface plasmon resonance (LSPR) in the infrared region of the electromagnetic spectrum and are the first demonstration of SiNCs to exhibit this remarkable optical property. The chapter describes the synthesis conditions necessary for production of SiNCs exhibiting LSPR, and uses compositional and structural characterization techniques to help identify the

exact role of the dopants. Portions of this chapter were published in Nano Letters (10.1021/nl4001184, 2013) in collaboration with Jong Seok Jeong and Prof K. Andre Mkhoyan from the Department of Chemical Engineering and Material Science at the University of Minnesota. Chapter 3 explains the synthesis of doped SiGeNC alloys for thermoelectric applications in collaboration with Tyson Baldridge and Prof. Mool Gupta, from the Department of Electrical and Computer Engineering at the University of Virginia. Thin film deposition and compositional characterization of the doped alloys were performed at the University of Minnesota and will be reported. Additionally, a summary of preliminary results reported by the University of Virginia will be included. Portions of this chapter were submitted to the Journal of Physical Chemistry Letters for publication. Chapter 4 highlights research which uses P-doped SiNCs to form emitter layers for pn-junction type solar cells. Important aspects of this research include thin film deposition; NC film post processing, such as annealing and etching; photovoltaic device fabrication; and optical characterization. Chapter 5 examines *inherent* impurities in the form of dangling bond defect evolution during oxidation of SiNCs; research performed in collaboration with Dr. Rui Pereira from the Department of Physics at the University of Aviero in Portugal. Portions of this chapter were published in Physical Review B (10.1103/PhysRevB.83.155327, 2011) and (10.1103/PhysRevB.86.085449, 2012). Following Chapter 5, a comprehensive bibliography is included. Finally, for the interested reader, several appendices outline device fabrication procedures and include results from tangential investigations on NC technology, regarding inkjet deposition of semiconductor NCs, metal-induced crystallization of NC films, and plasma-assisted synthesis of boron phosphide nanoparticles.

1.4. REFERENCES

(1) The Information Network *The Global Market for Equipment and Materials for IC Manufacturing*; 2012.

(2) Platzer, M. D. *U . S . Solar Photovoltaic Manufacturing : Industry Trends , Global Competition , Federal Support*; 2012.

(3) *2010 Solar Technologies Market Report*; 2011.

(4) Murray, C. B.; Norris, D. J.; Bawendi, M. G. *Journal of the American Chemical Society* **1993**, *115*, 8706–8715.

(5) Jurbergs, D.; Rogojina, E.; Mangolini, L.; U; Kortshagen, U. R. *Applied Physics Letters* **2006**, *88*, 233116.
(6) Govoni, M.; Marri, I.; Ossicini, S. *Nature Photonics* **2012**, *6*, 672–679.
(7) Beard, M. C.; Knutsen, K. P.; Yu, P.; Luther, J. M.; Song, Q.; Metzger, W. K.; Ellingson, R. J.; Nozik, A. J. *Nano Letters* **2007**, *7*, 2506–2512.
(8) Pavesi, L.; Dal Negro, L.; Mazzoleni, C.; Franzò, G.; Priolo, F. *Nature* **2000**, *408*, 440–4.
(9) Tiwari, S.; Rana, F.; Hanafi, H.; Hartstein, A.; Crabbé, E. F.; Chan, K. *Applied Physics Letters* **1996**, *68*, 1377.
(10) Liu, C.-Y.; Holman, Z. C.; Kortshagen, U. R. *Advanced Functional Materials* **2010**, *20*, 2157–2164.
(11) Liu, C.-Y.; Holman, Z. C.; Kortshagen, U. R. *Nano Letters* **2009**, *9*, 449–452.
(12) Liu, C.-Y.; Kortshagen, U. R. *Nanoscale* **2012**, *4*, 3963–8.
(13) Cheng, K.-Y.; Anthony, R.; Kortshagen, U. R.; Holmes, R. J. *Nano letters* **2011**, *11*, 1952–6.
(14) Goldstein, A. N.; Echer, C. M.; Alivisatos, A. P. *Science* **1992**, *256*, 1425–7.
(15) Holm, J.; Roberts, J. T. *Journal of Physical Chemistry C* **2009**, *113*, 15955–15963.
(16) Norris, D. J.; Efros, A. L.; Erwin, S. C. *Science* **2008**, *319*, 1776–9.
(17) Dalpian, G.; Chelikowsky, J. *Physical Review Letters* **2006**, *96*, 1–4.
(18) Petropoulos, J. P.; Cristiani, T. R.; Dongmo, P. B.; Zide, J. M. O. *Nanotechnology* **2011**, *22*, 245704.
(19) Erwin, S. C.; Zu, L.; Haftel, M. I.; Efros, A. L.; Kennedy, T. A.; Norris, D. J. *Nature* **2005**, *436*, 91–4.
(20) Borgarello, E.; Kiwi, J.; Graetzel, M.; Pelizzetti, E.; Visca, M. *Journal of the American Chemical Society* **1982**, *104*, 2996–3002.
(21) Canham, L. T. *Applied Physics Letters* **1990**, *57*, 1046.
(22) Godefroo, S.; Hayne, M.; Jivanescu, M.; Stesmans, A.; Zacharias, M.; Lebedev, O. I.; Van Tendeloo, G.; Moshchalkov, V. V *Nature nanotechnology* **2008**, *3*, 174–8.
(23) Park, S.; Cho, E.; Song, D.; Conibeer, G.; Green, M. A. *Solar Energy Materials and Solar Cells* **2009**, *93*, 684–690.
(24) Perez-Wurfl, I. H.; Hao, X.; Gentle, A.; Kim, D.; Conibeer, G.; Green, M. A. *Applied Physics Letters* **2009**, *95*, 153506.
(25) Di, D.; Perez-Wurfl, I.; Conibeer, G.; Green, M. A. *Solar Energy Materials and Solar Cells* **2010**, *94*, 2238–2243.
(26) Conibeer, G.; Green, M.; Cho, E.-C.; König, D.; Cho, Y.-H.; Fangsuwannarak, T.; Scardera, G.; Pink, E.; Huang, Y.; Puzzer, T.; Huang, S.; Song, D.; Flynn, C.; Park, S.; Hao, X.; Mansfield, D. *Thin Solid Films* **2008**, *516*, 6748–6756.
(27) Fujii, M.; Yamaguchi, Y.; Takase, Y.; Ninomiya, K.; Hayashi, S. *Applied Physics Letters* **2004**, *85*, 1158.
(28) Ito, M.; Imakita, K.; Fujii, M.; Hayashi, S. *Journal of Physics D: Applied Physics* **2010**, *43*, 505101.
(29) Hao, X. J.; Cho, E.-C.; Flynn, C.; Shen, Y. S.; Conibeer, G.; Green, M. a *Nanotechnology* **2008**, *19*, 424019.
(30) Baldwin, R. K.; Pettigrew, K. A.; Ratai, E.; Augustine, M. P.; Kauzlarich, S. M. *Chemical communications* **2002**, 1822–3.

(31) Tan, D.; Xu, B.; Chen, P.; Dai, Y.; Zhou, S.; Ma, G.; Qiu, J. *RSC Advances* **2012**, 8254–8257.
(32) Lacour, F.; Guillois, O.; Portier, X.; Perez, H.; Herlin, N.; Reynaud, C. *Physica E: Low-dimensional Systems and Nanostructures* **2007**, *38*, 11–15.
(33) Batson, P.; Heath, J. *Physical Review Letters* **1993**, *71*, 911–914.
(34) Littau, K. A.; Szajowski, P. J.; Muller, A. J.; Kortan, A. R.; Brus, L. E. *The Journal of Physical Chemistry* **1993**, *97*, 1224–1230.
(35) Salivati, N.; Shuall, N.; Baskin, E.; Garber, V.; McCrate, J. M.; Ekerdt, J. G. *Journal of Applied Physics* **2009**, *106*, 063121.
(36) Puigdollers, J.; Voz, C.; Orpella, A.; Martín, I.; Soler, D.; Fonrodona, M.; Bertomeu, J.; Andreu, J.; Alcubilla, R. *Journal of Non-Crystalline Solids* **2002**, *299-302*, 400–404.
(37) Golusda, E.; Hessenthaler, P.; Mollekopf, G.; Stafast, H. *Applied Surface Science* **1993**, *69*, 258–261.
(38) Iiduka, R.; Heya, A.; Matsumura, H. *Solar Energy Materials and Solar Cells* **1997**, *48*, 279–285.
(39) Jana, T.; Ray, S. *Thin Solid Films* **2000**, *376*, 241–248.
(40) Song, Y. J.; Lee, H.-G.; Teng, L.; Anderson, W. A. *MRS Proceedings* **2011**, *638*, F14.22.1.
(41) Hinds, W. C. *Aerosol Technology: Properties, Behavior, and Measurement of Airborne Particles*; John Wiley and Sons, Inc, 1999; Vol. 2nd.
(42) Gorla, C. R.; Liang, S.; Tompa, G. S.; Mayo, W. E.; Lu, Y. *Journal of Vacuum Science & Technology A: Vacuum, Surfaces, and Films* **1997**, *15*, 860.
(43) Bapat, A.; Perrey, C. R.; Campbell, S. A.; Barry Carter, C.; Kortshagen, U. *Journal of Applied Physics* **2003**, *94*, 1969.
(44) Kortshagen, U. *Journal of Physics D: Applied Physics* **2009**, *42*, 113001.
(45) Mangolini, L.; Thimsen, E.; Kortshagen, U. R. *Nano Letters* **2005**, *5*, 655–659.
(46) Mangolini, L.; Kortshagen, U. R. *Physical Review E (Statistical, Nonlinear, and Soft Matter Physics)* **2009**, *79*, 26405.
(47) Mangolini, L.; Kortshagen, U. R. *Advanced Materials* **2007**, *19*, 2513–2519.
(48) Pi, X. D.; Kortshagen, U. R. *Nanotechnology* **2009**, *20*.
(49) Gresback, R.; Hue, R.; Gladfelter, W. L.; Kortshagen, U. R. *Nanoscale research letters* **2011**, *6*, 68.
(50) Anthony, R.; Thimsen, E.; Johnson, J.; Campbell, S.; Kortshagen, U. *Mater. Res. Soc. Symp. Proc.* **2006**, *892*, 5–8.
(51) Pi, X. D.; Gresback, R.; Liptak, R. W.; Campbell, S. A.; Kortshagen, U. R. *Applied Physics Letters* **2008**, *92*, 2008–2010.
(52) Gupta, A.; Swihart, M. M. T.; Wiggers, H. *Advanced functional materials* **2009**, *19*, 696–703.
(53) Knipping, J.; Wiggers, H.; Rellinghaus, B.; Roth, P.; Konjhodzic, D.; Meier, C. *Journal of Nanoscience and Nanotechnology* **2004**, *4*, 1039–1044.
(54) Gresback, R.; Nozaki, T.; Okazaki, K. *Nanotechnology* **2011**, *22*, 305605.
(55) Shen, P.; Uesawa, N.; Inasawa, S.; Yamaguchi, Y. *Journal of Materials Chemistry* **2010**, *20*, 1669.
(56) Gresback, R.; Holman, Z.; Kortshagen, U. R. *Applied Physics Letters* **2007**, *91*, 93119.
(57) Anthony, R.; Kortshagen, U. *Physical Review B* **2009**, *80*, 1–6.

(58) Galli, F. Charge and Energy Interactions between Nanoparticles and Low Pressure Plasmas, 2010.
(59) Holman, Z. C.; Kortshagen, U. R. *Nanotechnology* **2010**, *21*, 335302.
(60) Friedlander 1927-, S. K. (Sheldon K. *Smoke, dust, and haze : fundamentals of aerosol dynamics*; New York : Oxford University Press: New York, 2000.
(61) Girshick, S. L. *Journal of Nanoparticle Research* **2008**, *10*, 935–945.

2. LOCALIZED SURFACE PLASMON RESONANCE FROM HEAVILY DOPED SINCS[‡]

2.1. INTRODUCTION

A localized surface plasmon resonance (LSPR) describes the collective oscillation of free charge carriers, which are dielectrically confined in a nanoparticle, in response to an external electromagnetic field.[1] Nanoparticles exhibiting LSPR display remarkable light scattering and absorption properties, stimulating intense research due to their applications in bio-sensing,[2] spectroscopy enhancement,[3] sub-wavelength microscopy,[4] and photovoltaics.[5] Among plasmonic materials, noble metals receive significant attention owing to their large free charge carrier concentration, N_{fc} ~ 10^{22}–10^{23} cm^{-3}, resulting in resonances within the visible spectral range.[1] However, recent efforts are exploring the potential of heavily doped semiconductor NCs for LSPRs in the infrared spectral range.[6–10] Despite silicon's importance for electronic and photonic applications, no LSPRs have been reported for doped SiNCs.

LSPRs enable one to tailor the optical response of nanomaterials through N_{fc}, morphology, and dielectric environment. However, unlike in metals, N_{fc} in semiconductors can be tailored by tuning the doping concentration or by other parameters such as temperature and/or charge injection, potentially enabling dynamic control of the LSPR response.[11,12] The lower N_{fc} in semiconductors (10^{18}–10^{21} cm^{-3}) shift LSPR frequencies into the near-infrared (NIR) through the terahertz (THz) region. The scarcity of tunable optical materials in this region is referred to as the "THz gap" in photonics, causing THz technology to develop slowly.[13] Unfortunately, effectively doping semiconductor NCs remains far from trivial. Dopant segregation to the NC surface may severely reduce the dopants' ability to provide free charge carriers.[14] At high synthesis temperatures, "self-purification" may occur, as NCs expel dopant atoms to the surface to lower the NCs' free energy.[15] At lower temperature, dopant incorporation requires favorable surface

[‡] Portions of this chapter have been published in the manuscript by David J. Rowe, Jong Seok Jeong, K. Andre Mhkoyan, and Uwe Kortshagen in *Nano Letters* (doi:10.1021/nl4001184, 2013).

conditions for dopant atoms to attach and be covered by additional atoms before becoming embedded in the NC.[16] Both processes may impose upper limits for N_{fc} and limit the potential of some semiconductors to display LSPRs. Vacancy doping elegantly circumvents some problems associated with impurity doping in compound semiconductors;[6–9] however, in group IV NCs, free charge carriers are generally not formed through vacancies,[17,18] thereby requiring substitutional doping.

Figure 2.1 displays the conditions under which mid-IR LSPRs in P-doped SiNCs may show expected resonant frequencies. Briefly, the LSPR frequency, f_{LSPR}, is derived beginning with the classical dipole polarizability, α, for a sub-wavelength sphere of diameter, d:[1]

$$\alpha(\omega) = \frac{\pi}{2} d^3 \frac{\varepsilon(\omega) - \varepsilon_m}{\varepsilon(\omega) + 2\varepsilon_m} \tag{2-1}$$

where ε_m is the dielectric constant of the surrounding medium, and the complex dielectric function, $\varepsilon(\omega)$. Resonance in the polarizability occurs when the so-called Fröhlich condition is met, such that the denominator diminishes:

$$\mathrm{Re}[\varepsilon(\omega)] + 2\varepsilon_m = 0 \Rightarrow \mathrm{Re}[\varepsilon(\omega)] = -2\varepsilon_m \tag{2-2}$$

If we use the classical Drude model to describe the complex dielectric function, we have:

$$\varepsilon(\omega) = \varepsilon_\infty - \frac{{\omega_p}^2}{\omega^2 + i\gamma\omega} = \mathrm{Re}[\varepsilon(\omega)] + i\,\mathrm{Im}[\varepsilon(\omega)] = \left(\varepsilon_\infty - \frac{{\omega_p}^2}{\omega^2 + \gamma^2}\right) + i\left(\frac{{\omega_p}^2 \gamma}{\omega(\omega^2 + \gamma^2)}\right) \tag{2-3}$$

where ε_∞ is the high frequency dielectric constant and taken as 11.7 for Si. Here, the bulk plasma frequency is defined as $\omega_p^2 = N_{fc}e^2/\varepsilon_o m_e^*$, where e is the electronic charge, m_e^* is the free carrier effective mass taken as that of a free electron ($m_e^*/m_o \sim 1$), ε_o is the free space permittivity, N_{fc} is the free carrier concentration in the SiNCs, and γ is the collisional frequency resulting from

surface and grain boundary scattering. When we insert the real part of the complex dielectric function at the LSPR frequency, ω_{LSPR} into Equation 2-2 we find:

$$\varepsilon_\infty - \frac{{\omega_p}^2}{{\omega_{LSPR}}^2 + \gamma^2} = -2\varepsilon_m \tag{2-4}$$

After inserting the expression for the plasma frequency, we rearrange equation Equation 4 to find the LSPR frequency:

$$\omega_{LSPR} = \sqrt{\frac{N_{fc}e^2}{\varepsilon_o m_e^*(\varepsilon_\infty + 2\varepsilon_m)} - \gamma^2} \tag{2-5}$$

Ignoring the effect of interfacial scattering and accounting for $\omega = 2\pi f$, we estimate the LSPR frequency as found in Equation 2-6, which is the form plotted in Figure 2.1.

$$f_{LSPR} = \frac{1}{2\pi}\sqrt{\frac{N_{fc}e^2}{\varepsilon_o m_e^*(\varepsilon_\infty + 2\varepsilon_m)}} \tag{2-6}$$

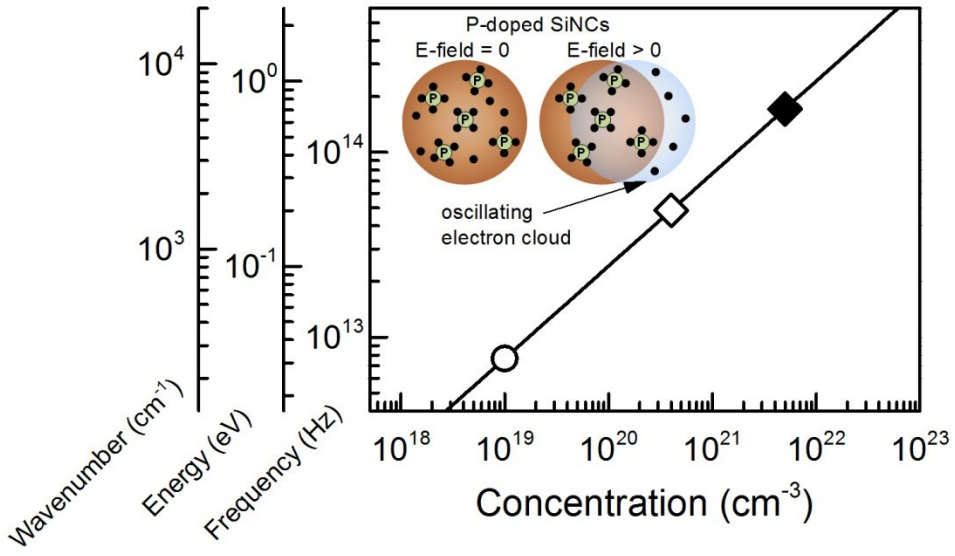

Figure 2.1. Predicted LSPR frequency. LSPR frequency, f_{LSPR}, for a spherical nanoparticle of sub-wavelength diameter, neglecting scattering estimated from the free charge carrier concentration, N_{fc}, given by Equation 2-6. Conversion to wavenumber (cm^{-1}) and energy (eV) are included for reference. Symbols identify the lower limit of N_{fc} given by Luther *et al.*[6] (circle) and the upper limits given by Nobili *et al.*[19] for laser annealed (filled diamond) and thermally annealed (open diamond) P-doped Si samples. (inset) Schematic of P-doped SiNC exhibiting LSPR under an applied electric field. The LSPR mode is supported by donated electrons from electrically active P atoms.

Luther *et al.*[6] suggested that < 10 carriers per 10 nm NC may be insufficient to support LSPRs, placing a lower limit for N_{fc} in SiNCs at $1x10^{19}$ cm^{-3} with ~ 0.02 at% of dopant. Electrically activated P concentrations in Si strongly depend on the activation process, giving a range for the upper limit of N_{fc}. Nobili *et al.*[19] measured N_{fc} as high as $5x10^{21}$ cm^{-3} with ~ 10 at% of dopant for ion-implanted Si annealed with a pulsed laser, and showed that N_{fc} decreased to $4x10^{20}$ cm^{-3} with 0.8 at% of dopant when subsequently annealed at 1273 K for 5 minutes. Pi *et al.*[20] achieved doping concentrations in SiNCs in the 0.1-10 at% range with nonthermal plasma synthesis, as first proposed by Mangolini *et al*.[21] Pi *et al.*[20] pointed out that P is taken up by the SiNC core with approximately 10-20% efficiency using a SiH_4/PH_3 plasma. Hence, it is reasonable to expect that a fractional PH_3 flow rate, defined as $X_{PH3} = [PH_3]/([PH_3]+[SiH_4])x100\%$, on the order of several 10% is required to achieve LSPR from SiNCs. For bulk Si, such large X_{PH3} appears unreasonably high, likely deterring such conditions for SiNC production and explaining the lack of LSPR observations in SiNCs.[20,22–25]

This chapter describes the production of degenerately doped SiNCs which exhibit tunable LSPRs in the energy range of 0.07-0.3 eV, or mid-infrared wavenumbers of 600-2500 cm^{-1}. It begins with a description of the nonthermal plasma technique used to dissociate gaseous Si and P precursors to simultaneously nucleate SiNCs and introduce P as an n-type dopant. From this follows a description of the conditions required to produce sufficiently high densities of free carriers to support an LSPR mode, a detailed materials characterization of the resulting SiNCs, and a discussion about the nature of P doping in SiNCs. Additionally, the chemical composition of the SiNCs was examined during the process of oxidation. The chapter concludes with a description of preliminary attempts at producing B-doped SiNCs and P-doped GeNCs which also exhibit LSPR and the results of those experiments.

2.2. Experimental Methods

2.2.1. Synthesis

The synthesis of highly crystalline, spherical SiNCs is modeled after the nonthermal plasma technique described in Chapter 1,[21] and standard conditions for producing highly P-doped SiNCs are given in Table 2.1. Briefly, to synthesize heavily P-doped SiNCs, PH_3 gas, diluted to 15% in H_2, is introduced into an RF capacitively-coupled nonthermal Ar:SiH_4 plasma, operating at a nominal power of 110-130 W. Typical flow rates are 0.5 standard cubic centimeters per minute (sccm) of SiH_4, 17 sccm of Ar, and 0-4 sccm of PH_3 diluted to 15% in H_2. The key parameter, the fractional PH_3 flow rate defined as $X_{PH3}=[PH_3]/([PH_3]+[SiH_4])x100\%$, is varied by changing the PH_3 flow rate while maintaining constant Ar and SiH_4 flow rates. Powder samples of P-doped SiNCs are collected directly from the gas-phase by spray coating NCs onto a clean substrate mounted onto a manual feed-through located inside the reactor. This technique is also known as inertial impaction, and is achieved by throttling the gas flow with a convergent, rectangular nozzle. Collisions with the accelerating gas flow transfer momentum to the SiNCs which then travel ballistically until they impact on the substrate. The substrate is placed in the path of the particle beam exiting the nozzle for a specified collection time. The feed-through is then retracted into a portable loadlock and transferred air-free to a N_2-purged glovebox for further characterization and

processing. In addition to accelerating the SiNCs, the rectangular nozzle controls the gas pressure in the plasma region by restricting flow. By adjusting the width of the nozzle opening, the pressure changes independently of the Ar gas flow. This method is used to produce samples at reactor pressures between 0.8 and 1.6 Torr. During the synthesis process, an amorphous layer of Si grows on the inner surface of the glass tube where SiH_4 dissociation occurs. Only when a clean, fresh tube is used are undoped SiNCs fabricated, suggesting that dopant which is incorporated in the amorphous film can be re-distributed among SiNCs when no additional PH_3 gas is added. Tubes are cleaned between runs using a potassium hydroxide bath to remove any grown Si films, and to reduce cross-contamination between production runs.

Table 2.1. Standard synthesis conditions for heavily P-doped SiNCs

	Unit	***Value***	***Notes***
Ar Flow	sccm	14-17	100% Ar
SiH_4 Flow	sccm	0.5	100% SiH_4
PH_3 Flow	sccm	0-5	15% in H_2
Pressure	Torr	0.8-1.6	actual
Power	W	110-130	nominal
Tube Diameter	inch	1	O.D., quartz
Deposition Time	min	0.5-1	

2.2.2. FOURIER TRANSFORM INFRARED SPECTROSCOPY (FTIR)

FTIR measurements were done using a Bruker Alpha IR spectrometer equipped with a diffuse reflectance (DRIFTS) accessory with a deuterated triglycine sulfate (DTGS) detector. All measurements were performed in a N_2 purged glovebox at room temperature. Samples were prepared by impacting SiNC films directly from the aerosol phase onto 1' x 1' chips of aluminum coated Si wafer, and transferred via a portable load lock, air free, to the glovebox. A bare, clean aluminum coated chip was used as a reference. A reflective substrate is required for DRIFTS measurements. All spectra were recorded from 400 cm^{-1} to 7500 cm^{-1} at 2 cm^{-1} resolution, and averaged over 24 scans.

2.2.3. X-RAY DIFFRACTION (XRD)

The crystalline diffraction pattern was measured using a Bruker diffractometer with a 2.2-kW sealed Cu x-ray source and a Hi-Star 2-D Area Detector. Samples were prepared by impacting SiNC films directly from the aerosol phase onto glass microscope slides. Several samples were collected per slide and analyzed by targeting the thickest regions of deposition. Diffraction patterns were recorded at ambient room conditions. Two frames of 30° each were collected, the first being centered at $2\theta = 36°$ and $\omega = 18°$, and each for 2-5 minutes, so as to provide a pattern with good signal to noise ratio. The mean NC diameter was calculated using the Scherrer equation.

2.2.4. SCANNING ELECTRON MICROSCOPY/ENERGY DISPERSIVE X-RAY SPECTROSCOPY (SEM/EDX)

Samples are transferred from the glovebox to a JEOL 6500 SEM equipped with a ThermoFisher Scientific NORAN System 6 EDX. X-rays are collected through a polymer-based window by a crystalline Si detector. Accelerating voltages between 5-10kV are used to maximize dead time while minimizing the damage to the sample. The accelerating voltage is adjusted so that the aluminum layer is not measured, such that the electron beam only probed SiNCs. From these measurements, we estimate the fractional P and O concentration ratio, defined as X_P=[P]/([P]+[Si]) and X_O=[O]/([O]+[Si]), respectively. The same samples that were used for FTIR measurements were subsequently used here.

2.2.5. SCANNING TRANSMISSION ELECTRON MICROSCOPY (STEM)

For TEM and STEM studies, samples are prepared by impacting a sub-monolayer of SiNCs directly onto a copper TEM grid covered with a holey carbon film. The samples are then transferred into a microscope under minimal ambient exposure. Characterization of SiNCs, including high-resolution bright field (BF)-TEM and high angle annular dark field (HAADF)-STEM imaging and EDX is conducted *in-situ* using an FEI Tecnai G2 F-30 (S)TEM with a Schottky field-emission electron gun operated at 300 and 200 kV accelerating voltages, described in detail by

Behr, Mkhoyan and Aydil.[26] The microscope is equipped with an EDAX Tecnai 30T/30ST 136-5 EDX Spectrometer. Jong Seok Jeong (JSJ) performed the TEM/STEM/EDX imaging and measurements. Additional size distribution analysis and counting statistics were performed by the author and JSJ using ImageJ.

2.2.6. *SiNC SURFACE ETCHING AND NC CORE ANALYSIS*

To analyze the SiNC core, the outer SiNC shell needed to be removed. Freshly prepared NC samples produced with varying X_{PH3} are immediately examined with SEM-EDX in order to measure X_O and X_P. Other samples prepared under identical conditions are stored in a N_2 purged glovebox for 90 hours or oxidized under ambient room conditions for 116 hours before being examined with SEM-EDX. The oxidized samples are subsequently etched with vapor of hydrofluoric acid in order to remove the Si oxide and any P incorporated therein, and then re-examined using SEM-EDX to provide an estimate of X_P in the NC core.

2.3. RESULTS & DISCUSSION – LSPR OBSERVATION

Figure 2.2 shows the IR absorbance spectra of samples produced with varying X_{PH3} for three different pressures in the plasma reactor. From the data one can see a broad absorption consistent with LSPR shifting from 400-1500 cm^{-1} as X_{PH3} increases. This broad absorption feature is superimposed with surface vibrational modes which are easily identified at low X_{PH3}. The sharpest peaks are associated with H bonded to Si - surface hydride stretching modes $Si\text{-}Si_{4-x}\text{-}H_x$ at 2138 cm^{-1}, 2101 cm^{-1}, 2081 cm^{-1} for x = 3,2,1, respectively; and higher order deformation modes at 1000-800 cm^{-1} and 750-550 cm^{-1}.[27] Additionally, a small peak at 2276 cm^{-1} grows with increasing X_{PH3}, which can be attributed to $Si\text{-}P_x\text{-}H_y$ surface vibrations.[28] Such an observation is consistent with increasing P segregation at the SiNC surface, and agrees with models describing dopant segregation in NCs.[16] While this so-called $Si\text{-}P_x\text{-}H_y$ peak occurs in the same wavenumber range of 2200-2300 cm^{-1} as some more commonly observed $O\text{-}Si\text{-}H_x$ peaks,[29] the almost complete absence of surface –OH (~3700 cm^{-1}) and Si-O-Si bridging (~1050 cm^{-1}) absorptions seems to rule out back-bonded O as the source of the peak.[30]

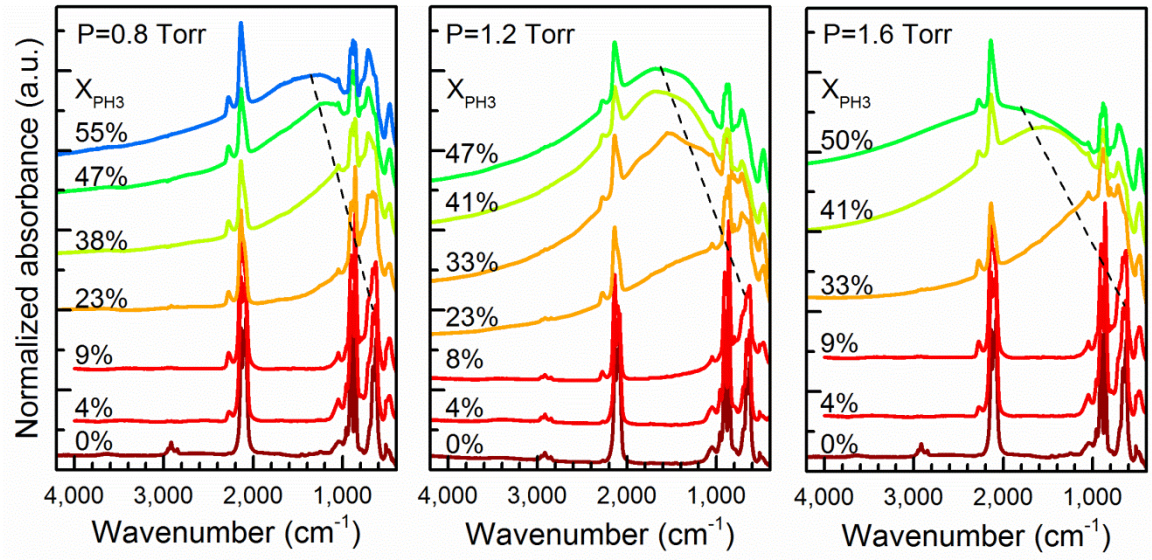

Figure 2.2. FTIR of P-doped SiNCs exhibiting LSPR. Normalized FTIR absorbance spectra of P-doped SiNCs for a range of X_{PH3} for P = 0.8, 1.2, and 1.6 Torr. As X_{PH3} increases a broad absorption feature develops and blue-shifts (a dashed line is added as a guide to the eye). Relevant surface vibrations are also identified as sharper features superimposed on the broad absorption. Spectra are offset vertically for clarity.

As shown in Figure 2.2, P-doped SiNCs produced at a higher pressure exhibit LSPRs varying controllably through 600-2000 cm^{-1}. By inspection of the three plots, two key conclusions can be made. First, one sees that higher pressures lead to a larger blue-shift of the LSPR peak for a similar range of X_{PH3} (indicated by the dashed line). Secondly, at higher pressure, the X_{PH3} required for the same blue-shift is generally reduced. Since the Ar flow rate remained essentially constant during the experiments, an increase in pressure indicates an increase in the residence time of the SiNCs in the plasma. Moreover, elevated pressures generally lead to increased particle heating in a plasma due to the increased rate of surface reactions. From this, one may conclude that SiNCs held at higher temperatures within the plasma exhibit LSPRs with higher frequencies. Further implications of this result will be discussed in a later section regarding annealing after production.

Additional data confirm a shift of the broad absorption with changes in the dielectric environment, consistent with an LSPR mode. Equation 2-6 shows that the LSPR frequency depends inversely on the dielectric environment surrounding the SiNCs. A SiNC film has voids

between the NCs with $\varepsilon_m = 1$. By infilling these voids with high dielectric constant solvents, the LSPR frequency should red-shift. As shown in Figure 2.3, the addition of solvent to a SiNC film exhibiting LSPR induces a red-shift in the broad absorption frequency. Acrylonitrile ($\varepsilon_m = 33$) and 2-octanone ($\varepsilon_m = 9.5$) were each dispensed (5 μL) on top of separate SiNC films while continuously recording IR spectra inside a N_2-purged glovebox. The progression of the solvent evaporation is shown by the reduction of strong, sharp molecular absorption at ~3000 cm^{-1}, and the gradual appearance of the broad LSPR mode around 1500 cm^{-1} now slightly red-shifted from its original position. As the solvent evaporates further from the film, the degree of infilling reduces and the effective dielectric constant of the medium shifts back towards $\varepsilon_m = 1$. As a result, the broad feature returns to the original position when the film was dry, as indicated by the dashed vertical line.

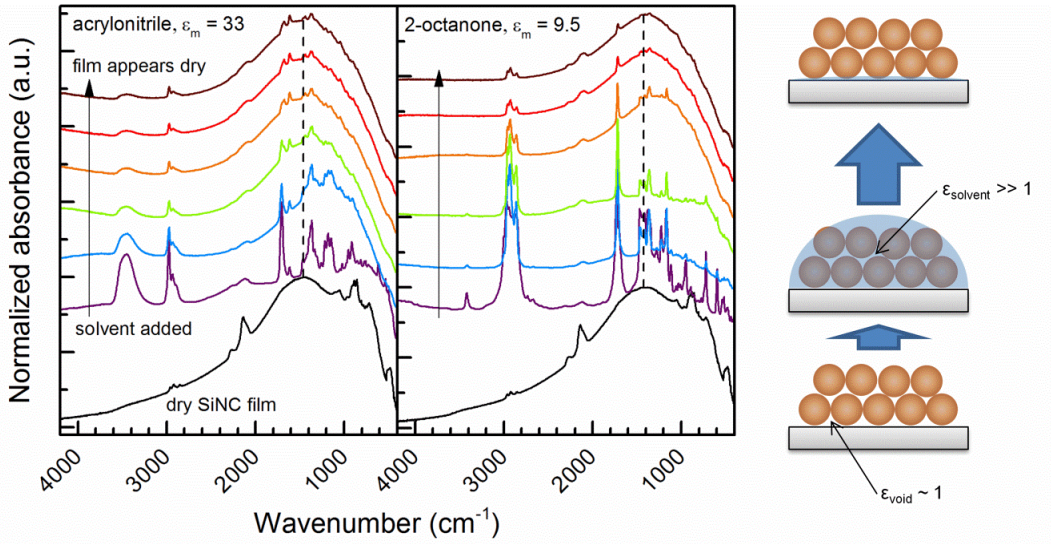

Figure 2.3. FTIR of P-doped SiNCs exhibiting LSPR under addition of high dielectric constant solvents. The lowest spectrum in each plot shows the film in a solvent-less state. Upon the addition of solvent, the LSPR modes are initially overwhelmed by the solvent vibrations, but eventually appear, and blue-shift back to the original frequency when the film appears dry to the naked eye. Spectra are normalized and offset for clarity.

Performing SiNC synthesis under X_{PH3} as high as 60% is unprecedented and thus calls for detailed materials characterization as unwanted stable Si-P compounds may form as synthesis byproducts and degrade the doping effectiveness. Figure 2.4(a-f) shows TEM images and size histograms for undoped, lightly doped, and heavily doped SiNCs (X_{PH3} = 0, 8.2 and 47 at%,

respectively). Bright-field (BF) TEM images reveal that particles have a crystalline core with approximately a 1 nm thick amorphous shell, regardless of X_{PH3}. Furthermore, BF-TEM images reveal increased twinning in SiNCs produced under large X_{PH3}. However, when numerous NCs are imaged, isolated examples of twinning are found even in undoped NCs. Figure 2.5 represents a general survey of samples produced under X_{PH3} = 0%, 8.2% and 47%, and shows the increased likelihood of twinning with X_{PH3}.

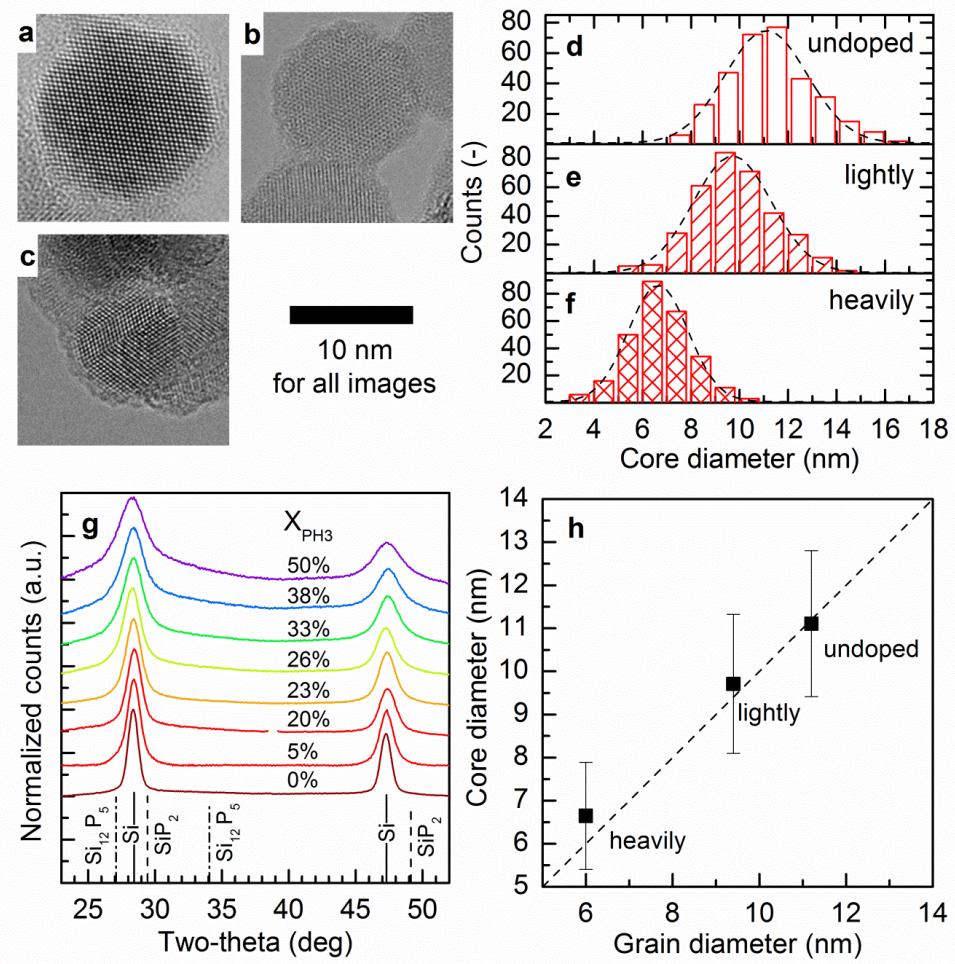

Figure 2.4. P-doped SiNC crystal structure. (a-c) BF-TEM images of SiNCs and (d-f) corresponding histograms for core diameters of undoped, lightly, and heavily P-doped SiNCs (X_{PH3} = 0%, 8.2% and 47%, respectively). Mean core diameter is estimated from a Gaussian fit to the histogram data (dashed line). (g) XRD patterns of SiNCs with increasing X_{PH3} indicate that diamond cubic Si is the only phase present. Diffraction patterns are offset vertically for clarity, and the angles for reflections from Si-P compounds are included for comparison. (h) Comparison between the grain diameter measured by XRD and the core diameter measured by TEM. The dashed line indicates 1:1 agreement between two measurement techniques. Error bars specify the standard deviation from Gaussian fits of the histograms shown in (d-f).

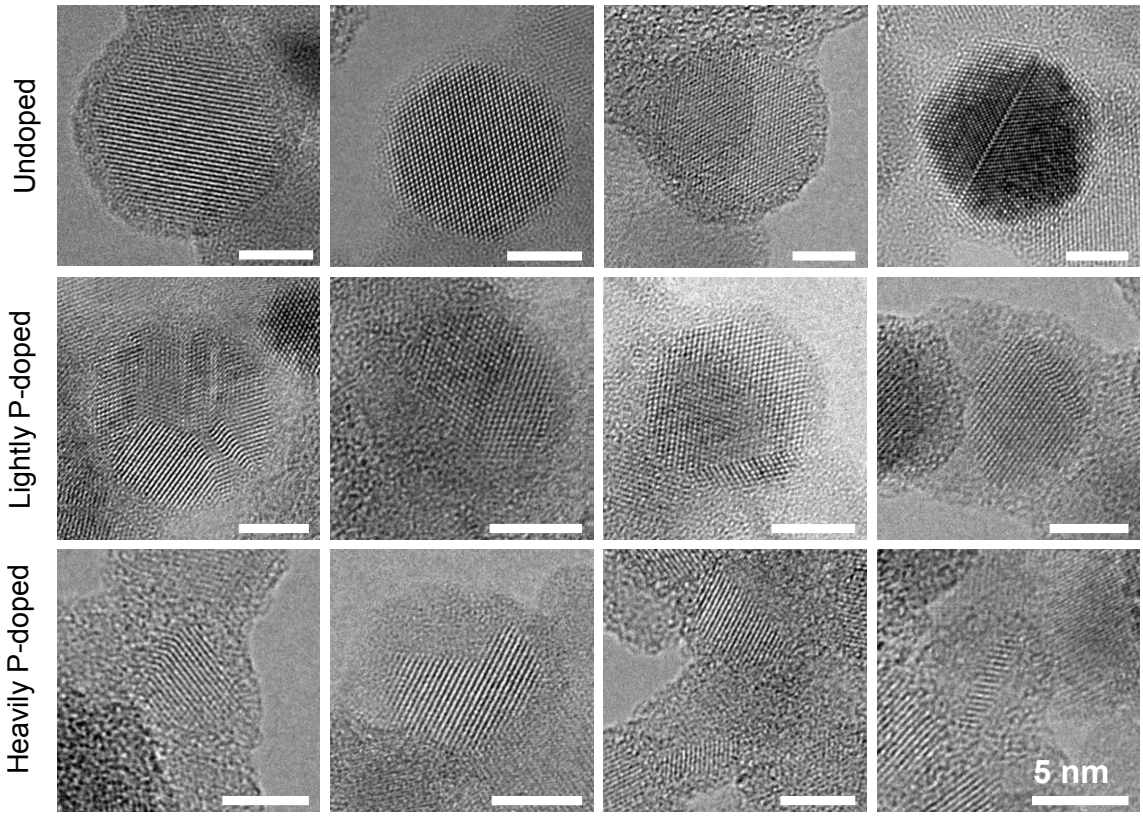

Figure 2.5. P-doped SiNC twinning. BF-TEM images of representative SiNCs produced for undoped, lightly and heavily P-doped SiNCs (X_{PH3} = 0%, 8.2% and 47%, respectively). All scale bars are 5 nm.

In Figure 2.4(g), X-ray diffraction (XRD) patterns further confirm the exclusive presence of Si by the absence of higher order diffraction peaks from Si-P compounds. We attribute the diffraction peak broadening as X_{PH3} increases to a decrease in SiNC diameter, consistent with TEM data. Figure 2.4(h) compares the NC diameter as derived from TEM images (core diameter) with the diameter derived from XRD data (grain diameter). Though twinning leads to a slight underestimation of particle size with XRD, both diagnostics show good agreement and reveal that the NC size strongly decreases with increasing X_{PH3}. This size decrease likely results from the PH_3 delivery in a 15:85 dilution in H_2, which reduces the NC growth rate through *in-situ* etching.[31] Furthermore, smaller SiNCs and grain boundaries from twinning result in an increasing number of plasmon scattering interfaces, explaining the observed LSPR broadening at large X_{PH3} in Figure 2.2.[6]

Though Figure 2.4(g) indicates that the SiNCs consist only of diamond cubic Si, additional studies were carried out to explore the magnitude and distribution of P within the SiNCs, as this should help to identify the concentration of electrically active dopants participating in the LSPR. The presence of surface Si-P_x-H_y vibrations shown in the FTIR data from Figure 2.2 indicates at least some P segregation to the SiNC surface. Additionally, STEM-EDX measurements further suggest that P is either incorporated into the SiNCs and/or condensed on the SiNC surfaces, as shown in Figure 2.6(a). However, the measurement resolution was insufficient to quantify the dopant concentration in the SiNC core, which would elucidate the nature of the free carrier density. In order to further probe the atomic P concentration, X_P = [P]/([P]+[Si])x100%, in the SiNC core, we adapted a technique previously used by Pi *et al.*,[20] where X_P is measured before and after wet chemical etching of P incorporated in a native oxide shell allowed to form on the SiNCs (detailed process found in Section 2.2.6). The etching process removes the native oxide, and presumably any other species that were located on the SiNC surface before the oxide shell grew. Figure 2.6(b) shows the SEM-EDX spectra measured for "as-produced" SiNCs with varying X_{PH3}, with C, O, Si, and P Kα lines identified at 0.277, 0.525, 1.74, and 2.01 keV, respectively. Contamination from O and C are estimated at less than 3 at% and are the result of air exposure during sample transfer. After converting the raw intensity spectra shown in Figure 2.6(b) to X_P as shown in Figure 2.6(c), the data suggests 60-75% of P was condensed on the NC surface and removed during the etching process. By comparing core X_P to X_{PH3}, one estimates the overall conversion efficiency of the gaseous PH_3 precursor to core P incorporation of ~10%, consistent with previous studies.[20,22]

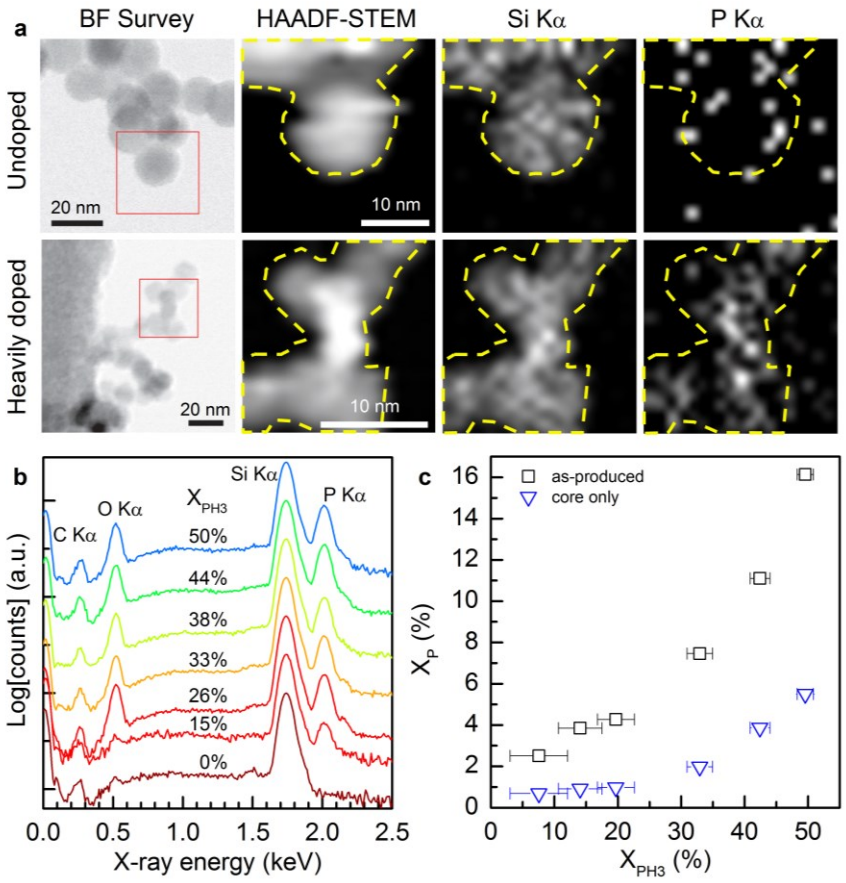

Figure 2.6. P incorporation in SiNCs. (a) BF-TEM images for survey, HAADF-STEM images and corresponding EDX maps for Si Kα and P Kα lines for undoped and heavily P-doped SiNCs. The red boxes indicate the analysis area. (b) Semi-log plot of SEM-EDX spectra for varying X_{PH3} of "as-produced" SiNCs. Spectra are offset vertically for clarity. (c) Estimated X_P from SEM-EDX spectra for "as produced" samples (squares) and for samples after surface P had been removed to probe the SiNC core (inverted triangles).

To understand the NC doping process in a nonthermal plasma, it is important to realize that nanoparticles are selectively heated to temperatures far exceeding the gas temperature by the combination of energetic surface reactions and slow convective cooling in the low pressure environment.[32] Excursions from an average temperature are more pronounced for smaller nanoparticles, as fewer atoms absorb the energy released by stochastically occurring surface reactions. When SiNCs are small and intermittently achieve high temperatures, Si atoms easily arrange to form crystalline cores. As the SiNCs grow, the thermal energy available for diffusion decreases, resulting in increased defect formation as Si and P atoms randomly attach to the NC

surface. This may explain the amorphous shell observed in TEM in Figures 2.4(a-c), which cannot be explained completely as an oxide layer.

Based on this picture, it is reasonable to conclude that free carriers may be trapped, and therefore electrically inactive, by defect states located near the NC surface created during the stochastic heating, shown schematically in Figure 2.7(a). Recently, low temperature annealing of SiNCs (<473 K) has proven sufficient for reducing defect concentrations by an order of magnitude.[33] As shown in Figure 2.7(b), when we annealed P-doped SiNCs, a clear LSPR blue-shift occurs at temperatures as low as 423 K, consistent with an increase in N_{fc} from 6.2×10^{20} cm^{-3} to 1.05×10^{21} cm^{-3} according to Figure 2.1. Furthermore, since elevated pressures generally lead to increased particle heating in a plasma due to the increased rate of surface reactions, this model also explains the blue-shift observed for samples shown in Figures 2.2. In the case of samples made under higher pressure, the increased residence time at a higher gas temperature in the plasma may have acted as *in-situ* annealing, and led to the reduction of surface defect states.

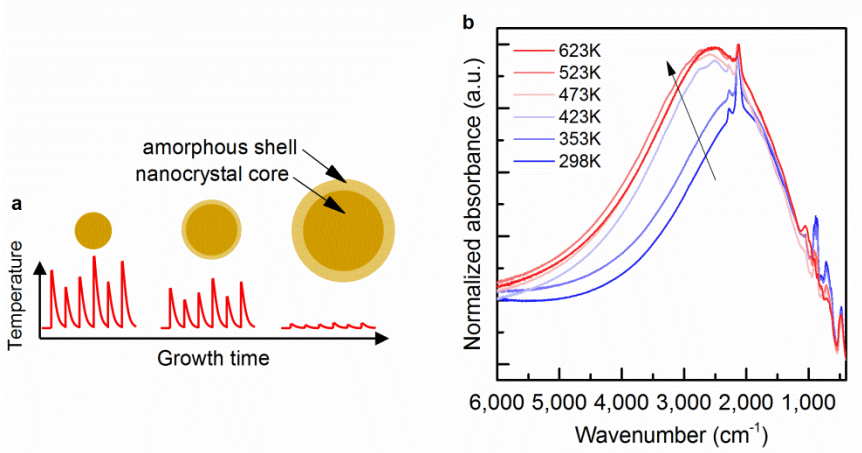

Figure 2.7. SiNC heating. (a) Schematic describing the mechanism of selective nanoparticle heating. When the SiNC is small, the thermal capacitance is low, and stochastically occurring surface reactions cause large fluctuations in the particle temperature. As the particle grows the temperature fluctuations decrease and thermal energy available for dopant activation decreases. (b) Blue-shift of highly P-doped SiNCs upon subsequent low-temperature annealing procedures. The addition of small amounts of thermal energy is sufficient to activate free carriers causing a blue-shift in the LSPR frequency.

Figure 2.8 summarizes the results of this study. It displays the measured LSPR peak positions versus the P concentration in the SiNC core. Predicted LSPR frequencies are shown for the measured P concentrations, ranging between environments with effective medium dielectric constants of N_2 (ε_m=1) and Si (ε_m=11.7). If the dielectric constant of the medium is taken as that of N_2 (ε_m=1) the observed LSPR frequencies are significantly lower than the predicted frequencies. However, in powder samples, the nearby SiNCs likely need to be accounted for in the dielectric constant of the medium. When Si (ε_m=11.7) is used for a medium the observed shift of the LSPR peak is more consistent with the expected square root dependence on $N_{fc.}$ However, these predictions are expected to overestimate the LSPR frequencies due to three likely inaccurate assumptions inherent to the model: (1) all core P is electrically activated and there are no trapped carriers, which likely overestimates N_{fc}, (2) interfacial scattering is negligible, and (3) plasmon coupling effects between nearby SiNCs is ignored. Each of these assumptions yields a larger LSPR frequency than may be found in our SiNCs, consistent with the data presented in Figure 4(c).

In conclusion, all results presented here are consistent with the first observation of LSPR in substitutionally P-doped SiNCs. We have shown that very large X_{PH3} is required during plasma synthesis to produce sufficient electrically activated free carriers for supporting LSPR modes. Furthermore, SiNCs produced under these conditions using the nonthermal plasma synthesis retain a diamond-cubic structure despite large concentrations of P. This facile synthesis approach allows for LSPR tunability in the mid-IR region and may enable Si-compatible IR photonics at the nanoscale.

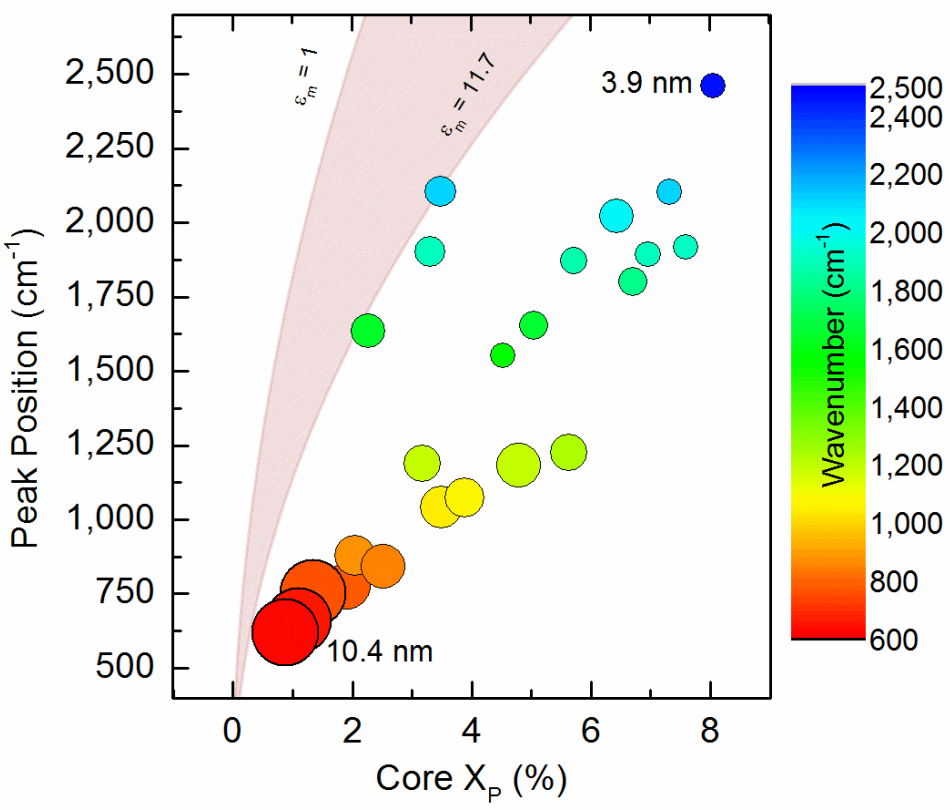

Figure 2.8. Summarized LSPR data for several P-doped SiNC samples vs. core X_P. For emphasis, the bubble size indicates the diameter of the SiNC core and the color corresponds to peak LSPR frequency. The largest and smallest NC diameter, 10.4 nm and 3.9 nm respectively, are labeled for reference. The predicted LSPR frequency range formed by assuming $\varepsilon_m = 1$ (N_2) and $\varepsilon_m = 11.7$ (Si) are shown for reference.

2.4. Results & Discussion – Oxidation of Heavily P-doped SiNCs

In the previous section, the oxidation process presumably captured surface impurities which were removed after etching, however the oxidative properties of such heavily doped SiNCs remains a fairly unexplored field. In order to identify X_O and X_P throughout the oxidation process, SEM-EDX was used to measure SiNC samples immediately after production, and after 90 hours of storage in a N_2 purged glovebox. Immediately after production, the EDX data shows that all samples consisted of X_O ~ 4%, as shown in Figure 2.9. We use a simple geometrical model to estimate the corresponding thickness based on initial X_O, and assuming bulk mass densities for Si (ρ_{Si} = 2.33 g/cm^3) and amorphous SiO_2 (ρ_{SiO2} = 2.196 g/cm^3). This model imposes mass conservation of Si during the oxidation process, which requires that the oxide layer consumes

part of the NC core. XRD measurements provide the initial NC diameter for samples produced with X_{PH3} = 8.2% and 47%, as 9.8 nm and 6.5 nm, respectively. Accounting for X_O ~ 4% this corresponds to an oxide shell of 0.1 nm and 0.07 nm, respectively, which implies a sub-monolayer of oxide and suggests that the amorphous shell observed in TEM is not the result of short exposure to air during sample transfers. Figure 2.9 also indicates an increase of X_O after 116 hours of ambient oxidation and the removal of the oxide with a hydrofluoric vapor etch. After oxidation, we measured X_O = 12% and 56% for samples produced with X_{PH3} = 8.2% and 47%, respectively. Using our model, we calculate an oxide thickness of 0.33 nm and 1.87 nm, respectively, and an equivalent reduction in the NC core diameter. After the etching process some O remains, likely resulting from the air exposure inherent to sample transfer and loading. Using reduced core diameters of 9.6 nm and 4.9 nm, and X_O = 3.4% and 10.6%, we estimate the post-etch oxide thickness as 0.08 nm and 0.14 nm, respectively.

As stated before and shown in Figure 2.6(c), EDX measurements of freshly prepared samples indicate X_P of 2.5-16% and similar measurements made after HF vapor etching showed a decrease to about 0.5-5%, which is attributed to the P concentration in the SiNC core. This analysis followed the same performed by Pi *et al.,*[20] however, additional measurements were also recorded, and revealed that the P had actually been removed from the SiNCs before the removal of the oxide shell with the HF vapor etch. The slow oxidation of the samples in ambient conditions resulted in a reduction of X_P by a factor of ~3.5, as shown by the data points labeled "ambient oxidized, pre-etch" in Figure 2.10. If these measurements are accepted, then two potential routes exist for the reduction in P: 1) sublimation of P from the SiNC surface at ambient conditions, or 2) through P redistribution during oxidation. The former seems more likely as the latter is usually only observed in bulk Si and at much higher temperatures,[34] however P sublimation from *any* Si surface has yet to be reported in the literature. Further validation that room temperature sublimation is occurring is that samples stored under N_2 ambient for 92 hours also display a reduction in X_P, and a very noticeable odor is detected from the sample indicating some sort of chemical desorption. SAFETY NOTE: the source of this odor has not been

confirmed, and should be considered toxic and dangerous. Experiments using mass spectrometry and/or gas chromatography should reveal the molecular or aerosol nature of the odor, and are currently underway.

In contrast to the conclusions of Pi *et al.*[20] the data shown in Figure 2.10 indicates that the removal of the oxide shell with HF vapor does in fact *not* lead to a further reduction in X_P. Nonetheless, from the EDX data and the oxidation model proposed above, one can estimate between 0.33-1.87 nm of oxide is removed during etching, suggesting that any residual P at the surface may also be removed. As a result, it is still valid to attribute the remaining P to the NC core, and report it as a function of X_{PH3} in Figure 2.10, ranging from 0.5-5 at%. However, at this time the precise mechanism for P sublimation is not known, and as a result, careful consideration needs to be taken when describing the location and distribution of P within the SiNC.

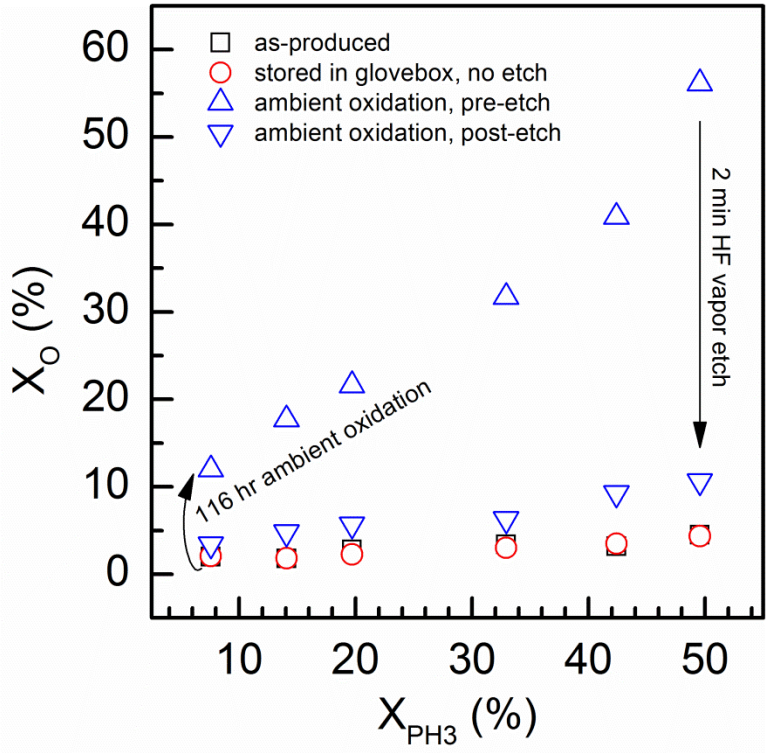

Figure 2.9. Atomic O concentration of SiNCs during oxidation. X_O measured by SEM-EDX for P-doped SiNC of varying X_{PH3} for samples processed as-produced (squares), after 90 hours of storage in a N_2 purged glovebox (circles), after 116 hours of ambient oxidation (triangles), and subsequently etched with HF vapor (inverted triangles).

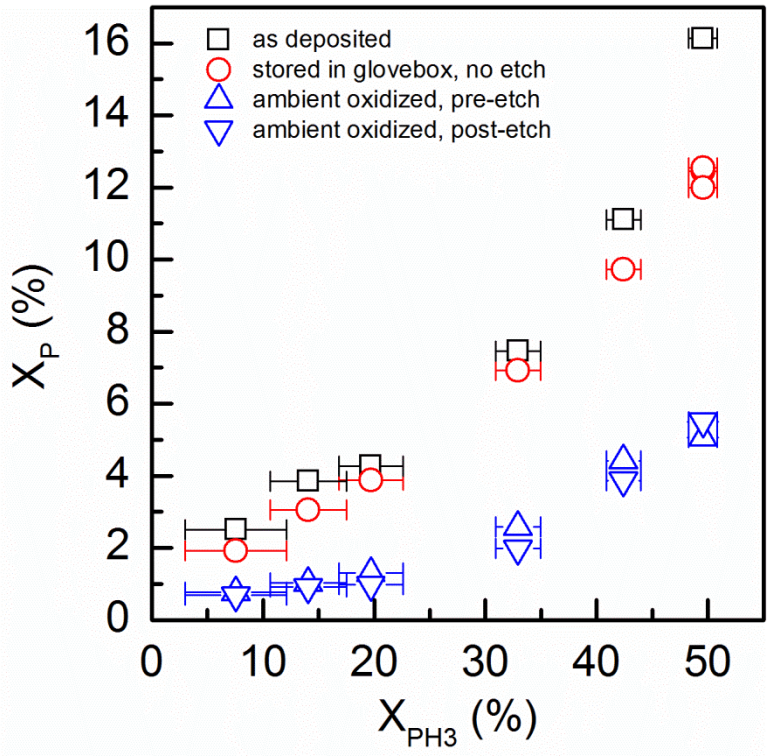

Figure 2.10. Atomic P concentration of SiNCs during oxidation. X_P measured by SEM-EDX for P-doped SiNC of varying X_{PH3} for samples processed as-produced (squares), after 92 hours of storage in N_2 purged glovebox (circles), after 116 hours of ambient oxidation (triangles), and subsequently etched with HF vapor (inverted triangles).

2.5. Preliminary Results - Alternative Doped Group IV NCs

Encouraged by the observation of LSPR in P-doped SiNC, additional experiments were conducted to determine if other materials would exhibit similar properties. B-doped SiNCs and P-doped GeNCs were synthesized, however LSPR was not observed in either case. Following is a brief account of the conditions and results acquired during these preliminary experiments.

2.5.1. B-doped SiNCs

The natural extension of observing LSPRs in P-doped SiNCs would be to attempt to measure a similar property in B-doped SiNCs. This was facilitated by already having access to B_2H_6 (diluted to 10% in H_2), which could easily be added to the Ar:SiH_4 plasma, exactly as PH_3 was.

Furthermore, it has been observed that B has a lower plasma incorporation efficiency, but incorporated dopant resides near the core of the particle, in a site more favorable to electrical activation.[20] Measurements of photoluminescent quantum yield for B-doped SiNCs also indicate that B is electrically active, as Auger recombination caused by increased charge carrier density reduces quantum yield.[20] Additionally, reports of LSPRs in copper chalcogenides have been attributed to vacancy doping giving rise p-type oscillations, indicating "hole" LSPRs are experimentally possible.[35] In spite of these advantages, maximum B solubility is lower in bulk Si than P,[36] so potential free carrier oscillations would exist at lower wavenumbers, i.e. further towards deep IR. Therefore, even if oscillations were present, they might be difficult to characterize due to interference with surface vibrations, low intensity, and lack of a detector with a lower wavenumber range (400 cm^{-1}).

Table 2.2. Standard synthesis conditions for heavily p-type doped SiNCs

	Unit	***Value***	***Notes***
Ar Flow	sccm	14-17	100%
SiH_4 Flow	sccm	0.5	100%
B_2H_6 Flow	sccm	0-5	10% in H_2
Pressure	Torr	1.6	actual
Power	W	110-130	nominal
Tube Diameter	inch	1	O.D., quartz
Deposition Time	min	0.5-1	

Figure 2.11(a) shows the FTIR spectra for SiNCs synthesized with different nominal B doping, defined as X_B = [B]/([B]+[Si]) = $2[B_2H_6]/(2[B_2H_6]+[SiH_4])$ to account for two B atoms per molecule of B_2H_6. Regardless of the amount of B_2H_6 added to the plasma, no sample exhibited LSPR for similar nominal doping concentrations used to synthesize P-doped SiNCs. However, analysis of the resulting material may provide a possible explanation.

For undoped SiNCs, surface hydride species are obvious from the stretching modes ($Si\text{-}Si_{4-x}\text{-}H_x$ at 2138 cm^{-1}, 2101 cm^{-1}, 2081 cm^{-1} for x = 3,2,1, respectively) and higher order vibrations in the 1000-800 cm^{-1} and 750-550 cm^{-1} range.[27] As B_2H_6 is added to the plasma new peaks begin to emerge, such as the peak at 2530 cm^{-1} which is likely due to $B_x\text{-}H_y$ stretching and the peak at

1340 cm^{-1} which has been attributed to either amorphous B-H or B-O bonds.[37] When only B_2H_6 (along with H and Ar) are reacted in the plasma, B_x-H_y and amorphous B-H or B-O vibrations are also observed, in addition to a small contribution from B-H-B bridging bonds found in the 2070 cm^{-1} – 2291 cm^{-1} region.[37] At low X_B, a small peak at 1878 cm^{-1} is observed, and merges into the Si-H stretches at higher nominal doping levels. This peak is attributed to surface stretches of Si-B_x-H_y. Upon addition of B_2H_6 into the plasma, the Si-H stretches are shifted from predominantly Si-Si-H_3 to Si-Si_3-H. As the amount of B_2H_6, and thus H used for dilution, is increased even more, the hydride stretches return to the Si-Si-H_3 configuration.

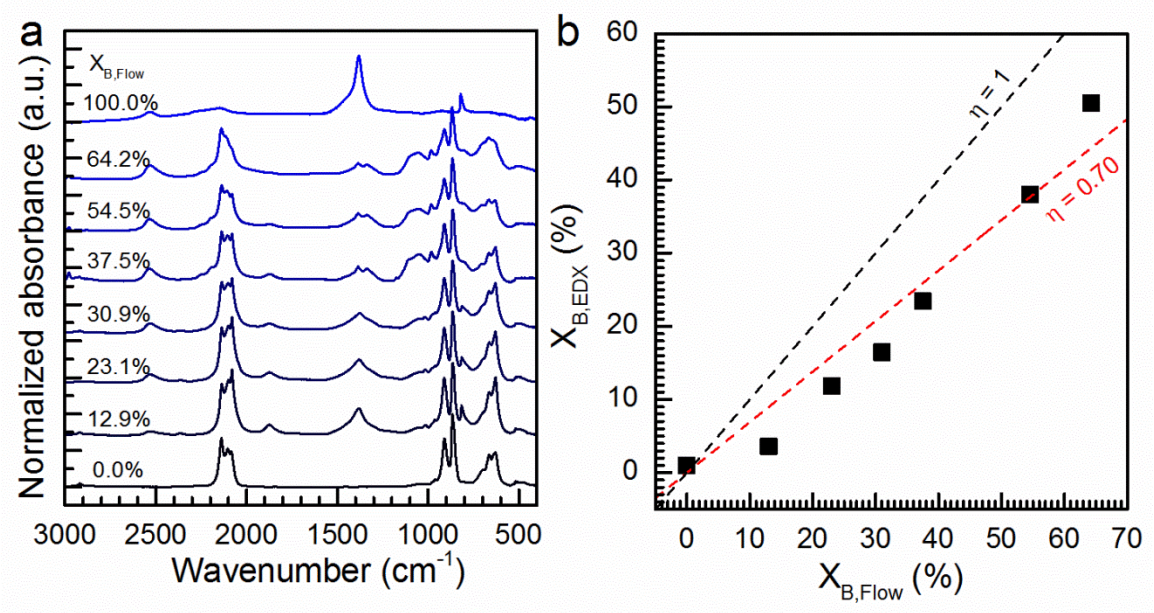

Figure 2.11. FTIR and EDX data from B-doped SiNCs. (a) FTIR spectra for B-doped SiNCs of varying X_B (normalized and offset for clarity). (b) EDX-measured X_B vs flow-based X_B, with straight line fits from zero for 100% and 70% incorporation.

Examination of the B doped SiNCs by EDX and XRD reveals a more complete picture of the particle structure. When only B_2H_6 (along with H_2 and Ar) are reacted in the plasma, the resulting material has no diffraction pattern, indicating only the presence of amorphous B compounds. Furthermore, mixtures of B_2H_6 and SiH_4 produced XRD patterns in which reflections from crystalline Si were only observed, i.e. no crystalline B or Si-B compounds were observed. Moreover, the EDX measurements show that in most cases the B is incorporated into the plasma-

produced powder at almost 70% efficiency, as seen in Figure 2.11(b), and high nominal doping results in powder which is 50% B. This could only be possible if the resulting powder is a mixture of doped SiNCs and amorphous B particles. One possible hypothesis is that at high nominal doping ratios needed to saturate SiNCs with enough dopants to observe LSPRs, B_2H_6 will decompose and natively nucleate to preferentially form amorphous B particles instead of act as a dopant. However, when the B_2H_6 concentration is low enough to avoid native nucleation, the activated dopant concentration is too low to support LSPRs. Until a more suitable B-doping precursor can be found for which native nucleation is not a factor, LSPRs from B-doped SiNCs will remain elusive.

2.5.2. P-DOPED GENCS

A second alternative to P-doped SiNCs would be to dope GeNCs with P. Similar to P in Si, P in Ge is also a shallow n-type donor (E_d = 12 meV)[38] suggesting P-doped GeNCs may exhibit similar electrical properties to P-doped SiNCs. Furthermore, since Ge has a lower melting temperature, thermodynamics would be favorable for incorporated P atoms to settle into electrically activated lattice sites, provided similar NC temperatures were attained within the plasma. Again though, the solubility of P in bulk Ge (0.4% at 600 °C) is lower than that of bulk Si,[39] which limits the amount of potential donors available to participate in an oscillation. To synthesize P-doped GeNCs, GeH_4 was mixed with PH_3 at a nominal ratio of Y_{PH3} = $[PH_3]/([PH_3]+[GeH_4])$ and reacted in the same plasma reactor under similar conditions. The quartz tube was replaced to minimize cross contamination from SiNCs.

Table 2.3. Standard synthesis conditions for n-type doped GeNCs

	Unit	*Value*	*Notes*
Ar Flow	sccm	14-17	100%
GeH_4 Flow	sccm	5	10% in Ar
PH_3 Flow	sccm	0-5	15% in H_2
Pressure	Torr	1.6	actual
Power	W	110-130	nominal
Tube Diameter	inch	1	O.D., quartz
Deposition Time	min	0.5-1	

In Figure 2.12(a), FTIR spectra are shown for the P-doped GeNCs. LSPRs were not observed under any conditions. The uneven background in the spectra are attributed to thin film interference, and changed depending on the orientation of the substrate in the spectrometer. Surface Ge-H stretching vibrations are observed between 1920-2050 cm^{-1}.[40] With increasing Y_{PH3}, the onset of a peak at 2272 cm^{-1} which is attributed to the Ge-P-H stretch is also observed. This is very similar to the vibration attributed to Si-P-H (2275 cm^{-1}), and can be understood by considering the reduced mass, m_{red}, of a three-body vibration (AB-C), given as:

$$m_{red} = \frac{1}{\left(\frac{1}{m_A + m_B} + \frac{1}{m_C}\right)} \tag{2-7}$$

So for m_{Ge} = 72.64 amu, m_{Si} = 28.05 amu, m_P = 30.97 amu, and m_H = 1.007 amu, then $m_{GeP\text{-}H}$ = 0.9973 amu and $m_{SiP\text{-}H}$ = 0.9901 amu, when only a mono-hydride species is accounted for. Since the vibrational frequency of a molecular bond, ν, is proportional to the inverse square of the reduced mass, if $m_{GeP-H} > m_{SiP-H}$, then it would follow that $\nu_{GeP-H} < \nu_{SiP-H}$, which is what is observed. Despite this being a crude approximation of the possible surface bonding configurations, the position of the peaks appears to be consistent with general theory. The very small reduced mass is due to considering the P-H bond as the source of this vibration, and not the Ge-P or Si-P. XRD was used to confirm Ge crystallinity and size, and rule out other germanium phosphide compounds which may have formed with saturated P conditions. Figure 2.12(b) shows XRD patterns for increasing Y_{PH3}, where only reflections from crystalline Ge are

observed. The reflections broaden with increased PH_3 flow, indicating smaller GeNC size, much the same as P-doped SiNCs. All of the P-doped GeNC samples are compared in Figure 2.12(c), where the effect of nominal power and nominal doping can be seen. The exact reason for the absence of LSPRs in P-doped GeNCs is still unknown. PH_3 was not observed to natively nucleate in an all-PH_3 plasma, so the formation of amorphous P particles which become sinks for P in the plasma is not likely. A more plausible hypothesis is that activated dopant incorporation in the GeNCs was so low that either the LSPR peak was too deep in the IR to observe, or there were not enough free carriers to support an oscillation. Based on the relative intensity of the GeP-H peak compared to the Ge-H peak, more of the GeNCs are covered in surface P stretches, possibly indicating enhanced "self-purification" of the GeNCs with respect to P and high diffusivity of P through Ge.[41] Instead, aluminum should be doped into Ge; it has a low ionization energy like P (E_a = 10 meV)[38], but instead has a very large maximum solubility (1.1% at 700 °C).[36]

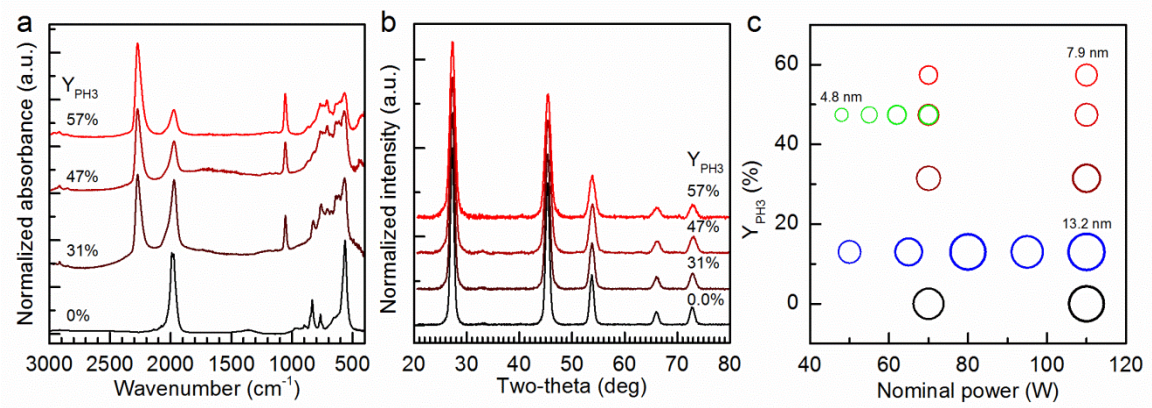

Figure 2.12. FTIR, XRD, and EDX data from P-doped GeNCs. (a) FTIR spectra and (b) XRD patterns of P-doped GeNCs of varying Y_{PH3} (normalized and offset vertically for clarity). (c) Bubble plot comparing the GeNC diameter measured from XRD to the nominal power and Y_{PH3}. The color mapped points in red correspond to the color mapping in (a) and (b). The size of the bubbles represents the diameter of the GeNC. Some bubbles are labeled for reference.

2.6. REFERENCES

(1) Kreibig, U.; Vollmer, M. *Optical Properties of Metal Clusters*; Springer: Berlin Heidelberg, 1995.

(2) Rodríguez-Lorenzo, L.; De la Rica, R.; Álvarez-Puebla, R. A.; Liz-Marzán, L. M.; Stevens, M. M. *Nature materials* **2012**, *11*, 604–607.

(3) Kundu, J.; Le, F.; Nordlander, P.; Halas, N. J. *Chemical Physics Letters* **2008**, *452*, 115–119.

(4) Jain, P. K.; Huang, X.; El-Sayed, I. H.; El-Sayed, M. A. *Accounts of Chemical Research* **2008**, *41*, 1578–86.

(5) Kelzenberg, M. D.; Boettcher, S. W.; Petykiewicz, J. A.; Turner-Evans, D. B.; Putnam, M. C.; Warren, E. L.; Spurgeon, J. M.; Briggs, R. M.; Lewis, N. S.; Atwater, H. A. *Nature materials* **2010**, *9*, 239–44.

(6) Luther, J. M.; Jain, P. K.; Ewers, T.; Alivisatos, A. P. *Nature materials* **2011**, *10*, 361–6.

(7) Kriegel, I.; Jiang, C.; Rodríguez-Fernández, J.; Schaller, R. D.; Talapin, D. V; Da Como, E.; Feldmann, J. *Journal of the American Chemical Society* **2012**, *134*, 1583–90.

(8) Manthiram, K.; Alivisatos, A. P. *Journal of the American Chemical Society* **2012**, *134*, 3995–8.

(9) Li, S. Q.; Guo, P.; Zhang, L.; Zhou, W.; Odom, T. W.; Seideman, T.; Ketterson, J. B.; Chang, R. P. H. *ACS nano* **2011**, *5*, 9161–9170.

(10) Buonsanti, R.; Llordes, A.; Aloni, S.; Helms, B. A.; Milliron, D. J. *Nano Letters* **2011**, *11*, 4706–10.

(11) Garcia, G.; Buonsanti, R.; Runnerstrom, E. L.; Mendelsberg, R. J.; Llordes, A.; Anders, A.; Richardson, T. J.; Milliron, D. J. *Nano letters* **2011**, *11*, 4415–20.

(12) Ju, L.; Geng, B.; Horng, J.; Girit, C.; Martin, M.; Hao, Z.; Bechtel, H. A.; Liang, X.; Zettl, A.; Shen, Y. R.; Wang, F. *Nature nanotechnology* **2011**, *6*, 630–4.

(13) Chen, H.-T.; Padilla, W. J.; Zide, J. M. O.; Gossard, A. C.; Taylor, A. J.; Averitt, R. D. *Nature* **2006**, *444*, 597–600.

(14) Dalpian, G.; Chelikowsky, J. *Physical Review Letters* **2006**, *96*, 1–4.

(15) Petropoulos, J. P.; Cristiani, T. R.; Dongmo, P. B.; Zide, J. M. O. *Nanotechnology* **2011**, *22*, 245704.

(16) Erwin, S. C.; Zu, L.; Haftel, M. I.; Efros, A. L.; Kennedy, T. A.; Norris, D. J. *Nature* **2005**, *436*, 91–4.

(17) Fage-Pedersen, J.; Larsen, A.; Mesli, A. *Physical Review B* **2000**, *62*, 10116–10125.

(18) Irmscher, K.; Klose, H.; Maass, K. *Journal of Physics C: Solid State Physics* **1984**, *17*, 6317–6329.

(19) Nobili, D.; Armigliato, A.; Finetti, M.; Solmi, S. *Journal of Applied Physics* **1982**, *53*, 1484.

(20) Pi, X. D.; Gresback, R.; Liptak, R. W.; Campbell, S. A.; Kortshagen, U. R. *Applied Physics Letters* **2008**, *92*, 2008–2010.

(21) Mangolini, L.; Thimsen, E.; Kortshagen, U. R. *Nano Letters* **2005**, *5*, 655–659.

(22) Stegner, A. R.; Pereira, R. N.; Lechner, R.; Klein, K.; Wiggers, H.; Stutzmann, M.; Brandt, M. S. *Physical Review B (Condensed Matter and Materials Physics)* **2009**, *80*, 165326 (10 pp.).

(23) Fujii, M.; Mimura, A.; Hayashi, S.; Yamamoto, Y.; Murakami, K. *Physical Review Letters* **2002**, *89*, 1–4.
(24) Perego, M.; Bonafos, C.; Fanciulli, M. *Nanotechnology* **2010**, *21*, 025602.
(25) Zhang, X.; Brynda, M.; Britt, R. D.; Carroll, E. C.; Larsen, D. S.; Louie, A. Y.; Kauzlarich, S. M. *Journal of the American Chemical Society* **2007**, *129*, 10668–9.
(26) Behr, M. J.; Mkhoyan, K. A.; Aydil, E. S. *ACS nano* **2010**, *4*, 5087–94.
(27) Marra, D. C.; Edelberg, E. A.; Naone, R. L.; Aydil, E. S. *Journal of Vacuum Science & Technology A: Vacuum, Surfaces, and Films* **1998**, *16*, 3199.
(28) Schrotter, J.; Cardenas, A.; Smaihi, M.; Hovnanian, N. *Journal of Sol-Gel Sci. and Tech.* **1995**, *4*, 195–204.
(29) Miura, T.; Niwano, M.; Shoji, D.; Miyamoto, N. *Journal of Applied Physics* **1996**, *79*, 4373.
(30) W Theiss *Surface Science Reports* **1997**, *29*, 91–192.
(31) Glass, J. A.; Wovchko, E. A.; Yates, J. T. *Surface Science* **1996**, *348*, 325–334.
(32) Mangolini, L.; Kortshagen, U. R. *Physical Review E (Statistical, Nonlinear, and Soft Matter Physics)* **2009**, *79*, 26405.
(33) Niesar, S.; Stegner, A. R.; Pereira, R. N.; Hoeb, M.; Wiggers, H.; Brandt, M. S.; Stutzmann, M. *Applied Physics Letters* **2010**, *96*, 193112.
(34) Grove, A. S.; Leistiko, O.; Sah, C. T. *Journal of Applied Physics* **1964**, *35*, 2695.
(35) Luther, J. M.; Jain, P. K.; Ewers, T.; Alivisatos, A. P. *Nature materials* **2011**, *10*.
(36) Trumbore, F. *The Bell System Technical Journal* **1960**, *39*, 205–233.
(37) Saß, M.; Annen, a.; Jacob, W. *Journal of Applied Physics* **1997**, *82*, 1905.
(38) Sze, S. M. *Physics of semiconductor devices*; New York, Wiley-Interscience: New York, 2005.
(39) Tsouroutas, P.; Tsoukalas, D.; Zergioti, I.; Cherkashin, N.; Claverie, A. *Journal of Applied Physics* **2009**, *105*, 094910.
(40) Bermejo, D.; Cardona, M. *Journal of Non-Crystalline Solids* **1979**, *32*, 421–430.
(41) Satta, A.; Janssens, T.; Clarysse, T.; Simoen, E.; Meuris, M.; Benedetti, A.; Hoflijk, I.; De Jaeger, B.; Demeurisse, C.; Vandervorst, W. *Journal of Vacuum Science & Technology B: Microelectronics and Nanometer Structures* **2006**, *24*, 494.

3. DOPED SILICON-GERMANIUM NCS FOR THERMOELECTRICS[‡]

3.1. INTRODUCTION

Thermoelectric materials – solid state materials which allow for direct conversion between heat and electricity – offer attractive alternatives to heating, cooling, and power generation. Thermoelectric devices have no moving parts or working fluid, e.g. R134a, but can recover electricity from waste heat and operate with zero greenhouse-gas emissions when coupled with renewable energy sources such as wind or solar PV. Currently, thermoelectric devices have found application in deep space power generation, cooling and heating units in automobile seats, thermocouple temperature probes, portable beverage coolers, and laser diode cooling.[1] Primarily, thermoelectrics have found success in niche applications such as these but have not been implemented on larger scales, despite apparent manufacturing and environmental advantages compared to other thermodynamic cycles. Why is this?

In short, the limiting factor is efficiency.[2] Most comparable conventional technologies, such as vapor power and refrigeration cycles, still outperform the best thermoelectric devices.[1] The efficiency of a thermoelectric material can be related to a dimensionless number known as the figure of merit, ZT, which is defined as:

$$ZT = \frac{\alpha^2 \sigma}{\kappa} T \qquad (3\text{-}1)$$

for a material with Seebeck coefficient, α, electrical conductivity, σ, thermal conductivity, κ, and absolute temperature, T. Currently, state-of-the-art thermoelectric materials boast ZT = 1-2,[3] but ZT > 3 has been proposed as the milestone necessary for thermoelectrics to compete with conventional thermodynamic cycles on larger scales.[2,4] Separately, each of the ZT components

[‡] Portions of this chapter were submitted to the Journal of Physical Chemistry Letters for publication under the authorship of David J. Rowe, Tyson Baldridge, Mool C. Gupta, and Uwe Kortshagen.

– α, σ, and κ – can be engineered over several orders of magnitude for a given material, however, the interdependence of these properties creates challenges for increasing ZT. An excellent review by Synder and Toberer details these trade-offs,[5] which is only summarized here for brevity.

When a material with free carriers is heated on one end, the free carriers will diffuse towards the cold end, establishing a charge density gradient and thereby an electric field. The Seebeck coefficient gives a measure of this effect, and is appropriately given units of V/K or μV/K for voltage developed per applied degree of temperature difference. In general, the Seebeck coefficient for a metal or doped semiconductor is inversely proportional to the carrier density, n, such that $\alpha \sim n^{-(2/3)}$. However, from Ohm's law, electrical conductivity is given as $\sigma = nq\mu$, for electrical charge, q, and carrier mobility, μ. Essentially, as the carrier density increases, so does the conductivity, but at the expense of the Seebeck coefficient. Another tradeoff occurs when considering the thermal conductivity, κ, which is comprised of two components, the lattice thermal conductivity, $\kappa_{lattice}$, and the electronic thermal conductivity, κ_{elec}, such that $\kappa = \kappa_{lattice} + \kappa_{elec}$. The lattice thermal conductivity comes from heat transfer through crystal lattice vibrations known as phonons. For example, glasses are known to have very low $\kappa_{lattice}$ and also have very low σ due to their electronic band structure. Furthermore, κ_{elec} is directly proportional to σ, leading to another conflicting dependence, i.e. crystalline materials are excellent thermal conductors *and* excellent electrical conductors. In the end, a very unique material is required for thermoelectrics – a material which transmits electrons (while still maintaining a large Seebeck coefficient) but prohibits the transfer of heat through phonons – a material given the name "phonon-glass electron-crystal".[6] Table 3.1 summarizes the symbols and interdependencies discussed above.

Table 3.1. Thermoelectric property descriptions and interdependencies

Property	*Symbol*	*"Good" Crystal*	*"Good" Glass*	*"Good" Thermoelectric*	*Interdependency*
Electrical conductivity	σ	high	low	high	$\sigma = nq\mu$
Thermal conductivity	κ	high	low	low	$\kappa = \kappa_{lattice} + \kappa_{elec}$ $\kappa_{elec} \sim \sigma$
Seebeck coefficient	α	high-med	med-low	high	$\alpha \sim n^{-(2/3)} \sim \sigma^{-(2/3)}$
Figure of Merit	ZT	low	low	high	$ZT = \frac{\alpha^2 \sigma}{\kappa} T$

It might appear that creating a phonon-glass electron-crystal requires careful consideration of each ZT component simultaneously; however, one component is slightly different than the rest and is receiving significant attention in the search for efficient thermoelectrics. The $\kappa_{lattice}$ has little interdependence with the other properties and can be minimized as much as possible without competing effects. This requires disruption of the crystal structure such that phonons are *scattered* efficiently while electrons are *transmitted* efficiently. The $\kappa_{lattice}$ can be reduced by introducing disorder within the crystal lattice, either through alloying with heavy elements, complex crystal structures, or through nano-structuring.[5] Research focusing on these three topics has produced several materials as potential high-performance thermoelectrics, including Bi_2Te_3, Sb_2Te_3, PbTe, GeTe, SiGe, Th_3P_4, clathrates, skutterudites, half-Heusler alloys, Ag_9TlTe_5, Tl_9BiTe_6, $Pb_2Sb_6Te_{11}$ to name only a few. A description of the advantages for each of these materials is beyond the scope of this chapter, but is expertly explained in several reviews for the interested reader.[2,3,5] Even with so many candidate materials for high-performance thermoelectrics, simple SiGe alloys provide several attractive properties over alternative thermoelectric materials. Firstly, it currently is the best thermoelectric material for high temperature (> 900 °C) applications.[7] Additionally, since Si and Ge are abundant and two of the most common materials in the microelectronics and photovoltaics industries, a vast infrastructure already exists for processing. Furthermore, unlike other materials, SiGe is easily doped n- and p-type with P and B, respectively, which is a key requirement for producing a functioning

thermoelectric generator. Lastly, the absence of heavy and toxic metals makes SiGe environmentally friendly.

Even with a simple material like SiGe, further development towards high ZT requires creating nanostructured materials. Production of nanostructured SiGe alloys can be accomplished using "bottom-up" approaches such as LPCVD[8], APCVD[9] or RF sputtering[10], however, "top-down" approaches, which first build the nanostructure and then form it into a bulk material, have had greater success. So far ball milling of Si and Ge, combined with hot pressing, has yielded nanostructured thermoelectric materials with very high performance.[11–13] This technique produces a large distribution of nanoparticle sizes comprised of many grains with a mean diameter of $d \sim 20$ nm. However, calculations for nanostructured SiGe indicate $d < 20$ nm for the largest reduction in $\kappa_{lattice}$, due to the grain size approaching that of the phonon mean free path length.[14] In other words, efficient phonon scattering leading to a better "phonon glass" requires grains smaller than the length between phonon collisions. To this effect, research focusing on "bottom-up" gas phase deposition techniques such as liquid-phase synthesis,[15] laser pyrolysis[16] and plasma synthesis[17–19] have successfully demonstrated the production of SiGe nanocrystals (SiGeNCs) down to 5-10nm.

Not only do the aforementioned gas phase synthesis techniques produce reduced grain sizes, they also provide an effective method for thin film deposition of thermoelectric materials. As mentioned above, ball milling and hot pressing form excellent bulk materials, but are generally incompatible with thin film or microprocessing techniques, required for on-chip energy harvesting.[20] Furthermore, gas phase deposition processes match closely with the requirements of more advanced thermoelectric materials, such as 2D quantum well deposition[21,22] and modulation doping.[23,24] In particular, gas phase impaction of NCs holds potential for rapid processing of such advanced thermoelectric architectures.[25] Research from Kortshagen's group indicates that nanoparticle impaction techniques are capable of producing nanoparticle films of down to 20 nm in thickness[26,27] with a density approaching that of the random packing fraction of

spheres. Furthermore, though the production of SiGeNCs from a nonthermal plasma has been demonstrated previously, assembly into thin films was not demonstrated.[18] Despite these studies, several unanswered questions exist when considering plasma processed, gas-phase impacted SiGeNC films for thermoelectrics. The quality of the SiGe alloy at the nanoparticle scale remains relatively unexplored. Even though Si and Ge are miscible with each other at thermal equilibrium, phase segregation remains a possibility by the use nonthermal plasma processing for SiGeNC production. Additionally, n- and p-type doping are required for fabricating a functional thermoelectric device, and to date doped NCs of any type remain challenging to synthesize.[28] Lastly, due to the importance of the grain size in nanostructured thermoelectrics, the size effect on alloying and doping in a nonequilibrium process could potentially limit the use of SiGeNCs.

This chapter describes a simple method for producing thin films of SiGeNCs for thermoelectrics as part of a collaborative study between the Department of Mechanical Engineering at the University of Minnesota (UMN) and the Department of Electrical and Computer Engineering at the University of Virginia (UVA). The alloy composition and doping concentration for SiGeNCs synthesized with a nonthermal plasma is characterized using XRD and EDX spectroscopy. Primarily, the composition of $Si_{0.8}Ge_{0.2}$ was explored since experiment[29] and theory[30] show that this SiGe ratio provides the optimal thermoelectric properties. Nevertheless, a range of $Si_{1-x}Ge_x$ compositions surrounding x = 0.2 were also explored. Additionally, dopant gases (B_2H_6 and PH_3) were added to the synthesis plasma to study the incorporation efficiency of B and P in SiGeNCs. Using an inertial impaction process to facilitate spray coating directly from the gas phase, good quality SiGeNC films were produced with high uniformity and reproducibility, crucial characteristics for additional post-processing and thermoelectric property measurement. Furthermore, UMN produced films demonstrating the flexibility of the impaction process for producing more advanced layered thermoelectric architectures, e.g. 2D quantum wells or modulation-doping layers. UMN engineered the film deposition and performed compositional characterization which comprises the majority of this chapter. Subsequently, the SiGeNC films

were sealed and transferred to UVA where they were laser annealed in an effort to reduce the film porosity while maintaining small grain diameter. Some preliminary results regarding laser annealing and property measurement will be reported in the last section, and will be attributed to UVA when necessary.

3.2. EXPERIMENTAL METHODS

3.2.1. SYNTHESIS OF B- AND P-DOPED SIGENCS

As described in Chapter 1, a nonthermal, low pressure plasma is used to synthesize SiGeNCs. SiH_4 and GeH_4 (diluted 10% in Ar) are used as precursor gases. PH_3 (15% diluted in H_2) or B_2H_6 (10% diluted in H_2) is added to the SiH_4:GeH_4:Ar mixture to dope the SiGeNCs n- or p-type, respectively. The gas pressure during synthesis is ~ 1.6 Torr and is controlled by Ar gas carrier flow. Table 3.2 outlines typical gas flow conditions for producing highly crystalline SiGeNCs. The composition of the gas flows can be described in an analog to the $Si_{1-x-y}Ge_xP_y$ or $Si_{1-x-z}Ge_xB_z$ ratio by $[SiH_4]_{1-a-b}[GeH_4]_a[PH_3]_b$ or $[SiH_4]_{1-a-c}[GeH_4]_a[B_2H_6]_c$ where *a*, *b*, and *c* are the flow percentages relative to the SiH_4 flow rate in the plasma. With this convention, {*a,b,c*} can be directly compared to {*x,y,z*} conveniently. Note that for B_2H_6, c^* indicates the total atomic B fraction accounting for the two B atoms per B_2H_6 molecule. For subscript notation, these flow percentages are given as numbers less than unity, but in plots are given as percentages. To reduce contamination during synthesis, the system is purged three times with N_2 and is pumped down to a base pressure below < 10 mTorr before gases are introduced. Films are fabricated by passing a substrate (SiO_2, SiC, AlN, or Si wafer) through the particle beam formed by a rectangular nozzle in the gas flow. The nozzle used to impact films is a beveled-orifice type, with adjustable height and width of 12 mm. For depositing SiGeNCs the nozzle was set to a width of 0.61 mm, giving it an aspect ratio of approximately 20. Substrates are cleaned with acetone, isopropanol, and deionized water, and dried with compressed air before loading into the reactor. Multiple substrates are loaded into the reactor simultaneously for increased throughput and for coating different substrates required for different characterization techniques.

Table 3.2. Standard synthesis conditions for n- or p-type doped SiGeNCs

	Unit	*Value*	*Notes*
Ar Flow	sccm	24-26	100%
SiH_4 Flow	sccm	0.75-0.9	100%
GeH_4 Flow	sccm	2.7-3.2	10% in Ar
PH_3 Flow	sccm	0.2-0.5	15% in H_2
B_2H_6 Flow	sccm	0.25-3.2	10% in H_2
Pressure	Torr	1.6	actual
Power	W	130	nominal
Tube Diameter	inch	1.00/0.85	O.D./I.D. - quartz
Deposition Time	min	4-10	t_{dep} ~ thickness
Nozzle Dimensions	mm	12 x 0.6	length x width

3.2.2. XRD

The crystalline diffraction pattern was measured using a Bruker diffractometer with a 2.2 kW sealed Cu Kα x-ray source and a Hi-Star 2-D Area Detector. Samples were prepared by impacting SiNC films directly from the aerosol phase onto glass microscope slides. Several samples were collected per slide and analyzed by targeting the thickest regions of deposition. Diffraction patterns were recorded at ambient room conditions. Samples were measured in "focused" mode, where two frames of 30° each were collected, the first being centered at 2θ = 36° and ω = 18°, and each for 2-5 minutes, so as to provide a pattern with good signal to noise ratio with a 0.8 mm collimator. The total scan spans 21° < 2θ < 81° and is performed in "coupled" mode. The mean NC diameter was calculated from the diffraction peak broadening using the Scherrer equation. All scans were corrected for instrumental broadening by recording standard full-width half-maximum (FWHM) curves using a lanthanum hexaboride reference material for each instrumental configuration.

3.2.3. SEM/EDX

SEM was performed using a JEOL 6500 field emission gun electron microscope. Samples were stored in a N_2 purged glovebox prior to imaging, and were transferred from the glovebox to the microscope as quickly as possible to minimize air exposure. While in the microscope, EDX spectroscopy was performed and the subsequent data was analyzed using a ThermoFisher Scientific NORAN System 6 energy dispersive x-ray spectrometer, and x-rays were collected

through a polymer-based window by a crystalline Si detector. Accelerating voltages between 5-10 kV were used to maximize dead time while minimizing the damage to the sample. The accelerating voltage was also adjusted so that the aluminum layer was not measured, such that the electron beam only probed the NC film. The pulse processor time constant was set to 50 for optimal throughput and signal resolution, and the live-time limit was set between 50-150 s for sufficient signal to noise ratio.

3.2.4. FTIR SPECTROSCOPY

FTIR measurements were done using a Bruker Alpha IR spectrometer equipped with a diffuse reflectance accessory with a deuterated triglycine sulfate (DTGS) detector. All measurements were performed in a N_2 purged glovebox at room temperature. Samples were prepared by impacting SiGeNC films directly from the aerosol phase onto 1" x 1" chips of aluminum coated Si wafer, and transferred via a portable load lock, air free, to the glovebox. A bare, clean aluminum coated chip was used as a reference. All spectra were recorded from 400 cm^{-1} to 7500 cm^{-1} at 2 cm^{-1} resolution, and averaged over 24 scans.

3.3. RESULTS & DISCUSSION – NC COMPOSITION & FILM STRUCTURE

3.3.1. FILM CHARACTERIZATION – SIGE ALLOY

An important feature of a SiGe system is the degree to which the Si and Ge have alloyed together. A true alloy is composed of a homogeneous distribution of one element (Ge) throughout the other (Si), with no phase segregation. Understanding the composition and structure of the synthesis produce facilitates interpretation of all the following process results and measurements. Specifically, inhomogeneities throughout the alloy strongly influence the laser annealing process. As one example, since Ge has a much lower melting point than Si, segregates of Ge will liquefy and coalesce during annealing before Si is close to its melting point, producing a non-uniform and phase segregated material, creating somewhat of a "positive-feedback" loop. Considering nanostructured films, the situation becomes even more complex. Nanocrystals comprised of phase pure Si or Ge may provide efficient phase-segregation

nucleation sites. Even though Pi *et al.*[18] described a process for producing alloyed SiGeNCs, the non-equilibrium plasma synthesis does not guarantee perfect Si and Ge distribution throughout the NC for a larger range of conditions than reported.

XRD provides excellent characterization of the phase composition of an alloyed sample, as well as information about NC size. Figure 3.1 shows the first reflection (111) of XRD patterns from films comprised of SiGeNCs, SiNCs, GeNCs, and layered structures of Si and Ge NCs. Plasma conditions were tuned to produce NCs of ~ 10 nm for each sample to provide comparable peak width. Single phase Si and Ge NCs show a single peak, indicative of the (111) reflection for each material. The layered film comprised of individual layers of Si and Ge NCs with mass ratio of 80:20 Si:Ge exhibits a double peak characteristic of the summation of pure SiNCs and pure GeNCs. SEM images of layered films (mass ratio 80:20 and 33:67 Si:Ge) deposited on Al-coated Si wafers, and corresponding XRD patterns are shown in Figure 3.2(a-c) to illustrate the clear phase segregation and the resulting diffraction pattern from such a material. The SiGeNC pattern shows one single reflection, again indicative of a single, true phase, however shifted centrally between phase pure SiNCs and GeNCs. Based on this, one safely concludes that the alloying was successful, and any phase segregation must occur on a length scale smaller than the mean diameter of the NCs. Furthermore, the shift of the peak provides an estimation of the alloy composition. From Figure 3.3, the SiGeNC (111) reflection appears at 2θ = 28.233°. From Bragg's law, $2d_{111}\sin\theta = n\lambda$, where n = 1 and λ = 0.154059 nm is the Cu Kα wavelength, the interplanar spacing, d_{111}, is estimated as 0.316 nm. For a cubic lattice, the lattice parameter, a_{111}, can be estimated from $d_{111} = a_{111}/\sqrt{h^2+k^2+l^2}$ where $h = k = l = 1$ such that a_{111} = 0.5470 nm. Invoking Vegard's law for alloys, the atomic concentration of Ge, x, can be estimated from $a_{SiGe} = xa_{Ge} + (1-x)a_{Si}$, where a_{SiGe} is the measured lattice parameter (a_{111}), and a_{Ge}, a_{Si} are the lattice parameters for pure Ge and Si, respectively, given as a_{Ge} = 0.5658 nm and a_{Si} = 0.5430 nm.[31] Table 3.3 details the structural parameters a and d and how they relate to the experimental

parameter, *2θ* for each material. From this, the atomic concentration is estimated as $Si_{0.823}Ge_{0.177}$, which is slightly lower than the gas flow ratio of $[SiH_4]_{0.714}[GeH_4]_{0.286}$.

Table 3.3. Standard Si and Ge XRD diffraction values and measured* $Si_{1-x}Ge_x$ values for (111) reflection.

	2θ (deg)	*a (nm)*	*d (nm)*
Si	28.447	0.5430	0.3135
Ge	27.278	0.5658	0.3267
$Si_{1-x}Ge_x$	28.233*	0.5470	0.3158

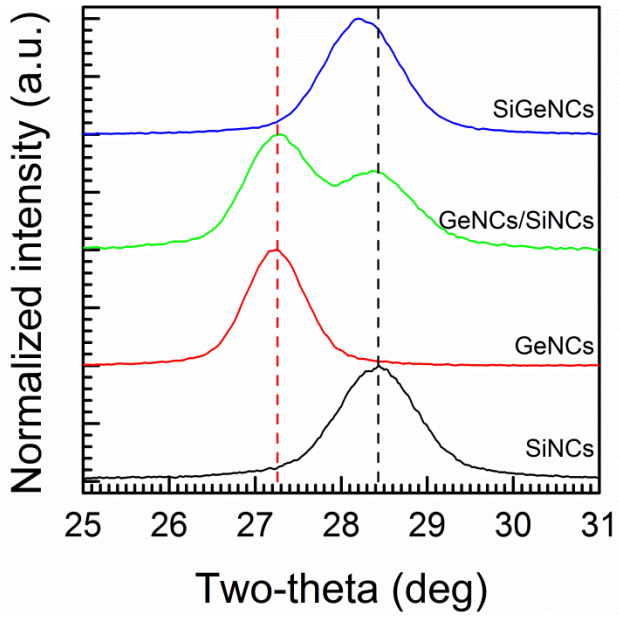

Figure 3.1. Si, Ge, and SiGe NC XRD. XRD patterns for alloyed SiGeNCs, 80:20 Si:Ge mass ratio layered films (GeNCs/SiNCs), pure GeNCs, and pure SiNCs. The dashed lines indicate the (111) reflection for Si and Ge.

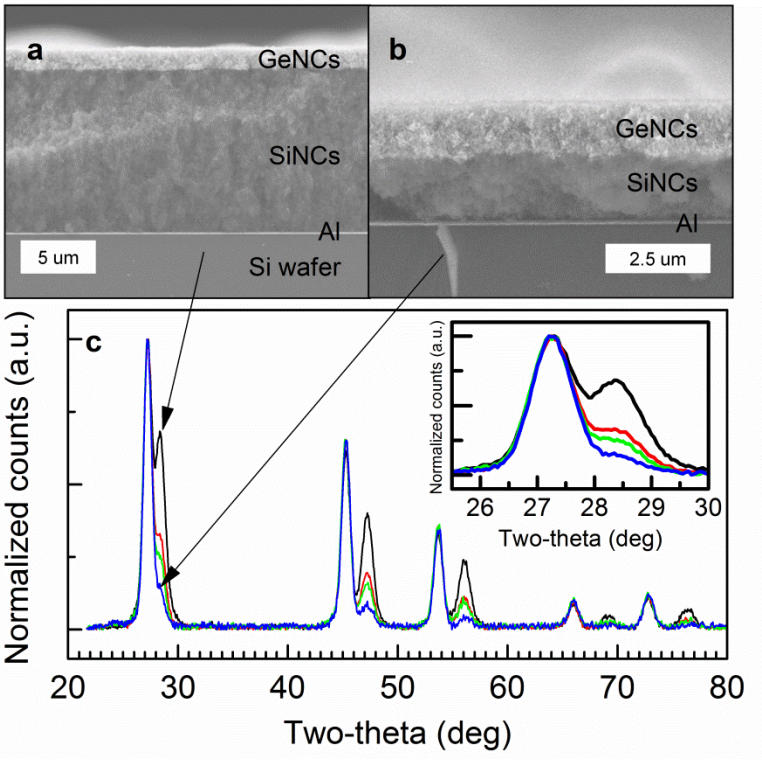

Figure 3.2. SiNC and GeNC layered films. SEM image of layered GeNC/SiNC films deposited on gold coated Si wafers, with Si:Ge mass ratio of (a) 80:20, and (b) 33:67. (c) Corresponding XRD patterns for layered films of Si:Ge deposited on glass with mass ratio of 80:20 (black), 67:33 (red), 50:50 (green), and 33:67(blue).

To confirm the ratio of $Si_{1-x}Ge_x$ as estimated from XRD data, energy dispersive x-ray spectroscopy (EDX) was also performed on the samples. Figure 3.3(a) shows the EDX spectra for the undoped SiGeNC film made with $[SiH_4]_{0.714}[GeH_4]_{0.286}$. Peaks from the *Kα* lines for the lighter elements such as C, O, and Si, and from the *Lα* lines for Ge are all clearly visible when the data is plotted as a semi-log. From this raw intensity of counted x-rays, and knowing x-ray absorption cross-sections, the atomic percentages of the elements can be deduced. It is likely the presence of O and C is due to ambient contamination and not a direct result of synthesis conditions. Since this contamination is added to the material *after* synthesis, it can be disregarded in the calculation of atomic Si and Ge ratios. After accounting for only the Si and Ge, we estimate $Si_{0.758}Ge_{0.242}$, which is in better agreement with the ratio estimate from XRD. When all the samples are analyzed this way, we can estimate the incorporation of Ge in the SiGeNCs over all flow conditions. As shown in Figure 3.3(b), a straight line fit to the data, with the intercept

fixed at zero gives us η_{alloy} = 0.76 ± 0.20, the incorporation efficiency of Ge into Si. While this also explains the disparity between the XRD measurement of alloy content and the nominal alloy content value, the exact reason for decreased Ge is not known. One explanation could be that oxidation of Ge between synthesis and measurement could be affecting the final result. Since GeO_2 is soluble in water, residual amounts of water vapor in the air could etch the Ge immediately upon removal from the reactor. However, a more reasonable explanation has to do with the flow conditions used for synthesis. Low flow rates were required for the uniform deposition of SiGeNC films, which in turn required that the GeH_4 flow controller be operated at less than 2% of the full scale. At low flow rates, thermal-based flow controllers are far less accurate and likely lead to an inaccurate reading of actual flow rates. This uncertainty is illustrated in Figure 3.3(b) as the difference between films made under "identical" $[SiH_4]_{1-a}[GeH_4]_a$. For example, EDX measurements indicate $Si_{1-x}Ge_x$ ratios change by up to 3% in films synthesized at a = 28% (small size only). Unfortunately, increasing the GeH_4 flow rates to more accurate process ranges leads to increased particle density in the reactor, which in turn resulted in uneven film deposition which was unsuitable for further processing. The size of the bubbles in Figure 3.3(b) represents the mean diameter of each sample measured with XRD, and illustrates plainly the final composition of the NC depends primarily on the gas flow composition and remains independent of the NC size, within a moderate range near $Si_{0.8}Ge_{0.2}$. No obvious trend was observed for relating composition to the final size of the NC. These results indicate that production of an alloyed SiGe NC requires careful attention to the flow composition but, if done properly, appears robust over a range of compositions and NC sizes suitable for thermoelectric processing.

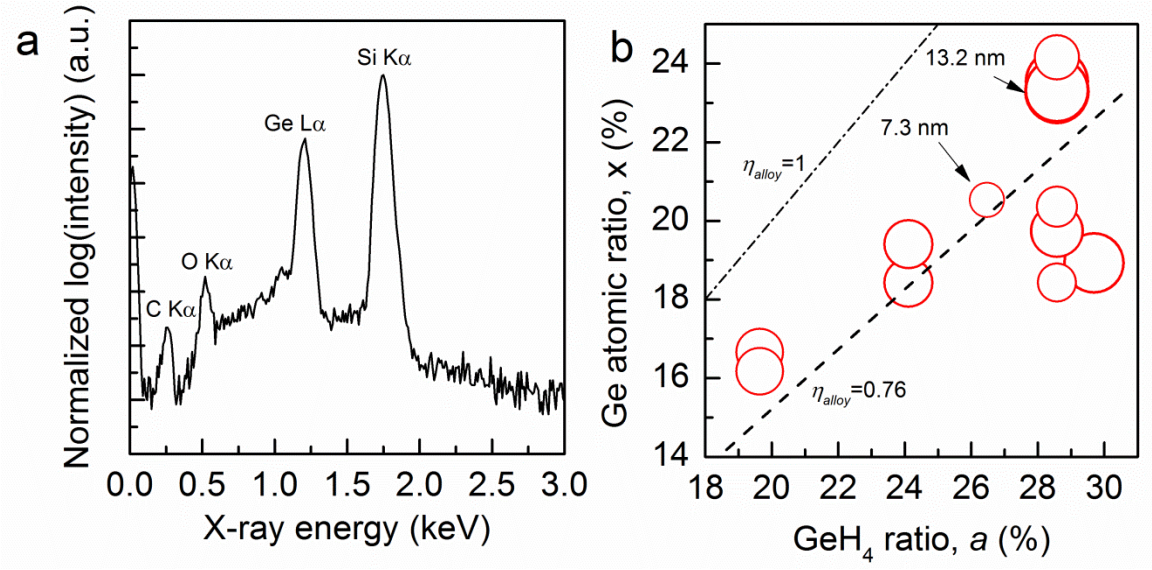

Figure 3.3. $Si_{1-x}Ge_x$ ratio of plasma produced SiGeNCs. (a) Semi-log EDX spectra for undoped SiGeNC films of $[SiH_4]_{0.71}[GeH_4]_{0.29}$, normalized to the Si Kα peak. (b) $Si_{1-x}Ge_x$ measured by EDX for flow conditions of $[SiH_4]_{1-a}[GeH_4]_a$. Included is a straight line fit to the data, estimating an incorporation efficiency, η_{alloy} = 0.76, and a line indicating η_{alloy} = 1 for reference. The size of the bubble indicates the size of the NC measured using XRD, and the largest and smallest sizes are included for reference.

3.3.2. Film Characterization – Inclusion of Dopants

The inclusion of dopants into SiGeNCs is crucial as both p- and n-type materials are necessary to construct an actual thermoelectric generator. Likewise, since electrical conductivity, thermal conductivity, and Seebeck coefficient are highly dependent on doping concentrations, precise knowledge of synthesis conditions conducive for doping is critical when fabricating thermoelectric materials. Chapter 2 elaborated on the challenges associated with NC doping, focusing on heavily P-doped SiNCs. In this section, the conditions required for light B- and P-doping of SiGeNCs will be investigated and dopant inclusion will be characterized using EDX and FTIR. Table 3.4 provides sample labels, flow conditions, and flow composition in agreement with the {*a,b,c*} convention described previously. In some cases, additional samples beyond the ones described in Table 3.4 were included in some of the plots.

Table 3.4. Doped SiGe samples for EDX and FTIR analysis with precursor flow rates.

Sample Name	*SiH_4 (sccm)*	*GeH_4 (sccm)*	*PH_3 (sccm)*	*B_2H_6 (sccm)*	*1-a-b or 1-a-c*	*a*	*b*	*c*	*c**
SG	0.8	0.32	0	0	0.714	0.286	0	0	0
SGP1	0.8	0.32	0.015	0	0.705	0.282	0.013	0	0
SGP2	0.8	0.32	0.030	0	0.695	0.278	0.026	0	0
SGP3	0.8	0.32	0.045	0	0.687	0.275	0.039	0	0
SGP4	0.8	0.32	0.060	0	0.678	0.271	0.051	0	0
SGP5	0.8	0.32	0.075	0	0.669	0.268	0.063	0	0
SGP6	0.8	0.32	0.090	0	0.661	0.264	0.074	0	0
SGB1	0.8	0.32	0	0.028	0.697	0.279	0	0.024	0.048
SGB2	0.8	0.32	0	0.056	0.680	0.272	0	0.048	0.091
SGB3	0.8	0.32	0	0.084	0.664	0.266	0	0.070	0.130
SGB4	0.8	0.32	0	0.112	0.649	0.260	0	0.091	0.167
SGB5	0.8	0.32	0	0.140	0.635	0.254	0	0.111	0.200

Figure 3.4(a) shows EDX spectra in semi-log representation for P-doped SiGeNCs. A peak at 2.01 keV corresponds to the Kα line of P and is easily distinguished from the Si Kα peak at 1.74 keV. The P peak clearly grows with increased PH_3 flow into the plasma. The Ge Lα band consists of several transitions which show up as two distinct peaks, a major peak centered near 1.19 keV, and a minor peak at 1.04 keV, and remains approximately constant with respect to the Si peak even as more dopant is added. The C and O Kα peaks are also observed in the semi-log representation, centered at 0.277 keV and 0.525 keV, respectively. Contamination from environmental exposure leads to C and O presence in the sample and remains a difficult feature to eliminate. Figure 3.4(b) shows the comparison between the atomic P ratio for the flow composition and the measured "as-produced" composition. For P-doped SiGeNCs, the P incorporation efficiency, η_P = 0.29 ± 0.015, agrees very closely with the impurity incorporation of heavily doped SiNCs synthesized in Chapter 2, when fitting the data to a straight line with zero intercept. The bubble size in the plot represents the XRD NC size, and indicates that over this small range of doping, the NC size changes very little. Some samples made at other conditions show smaller diameters, but this was accomplished by varying the synthesis pressure and is not a direct result of the doping process.

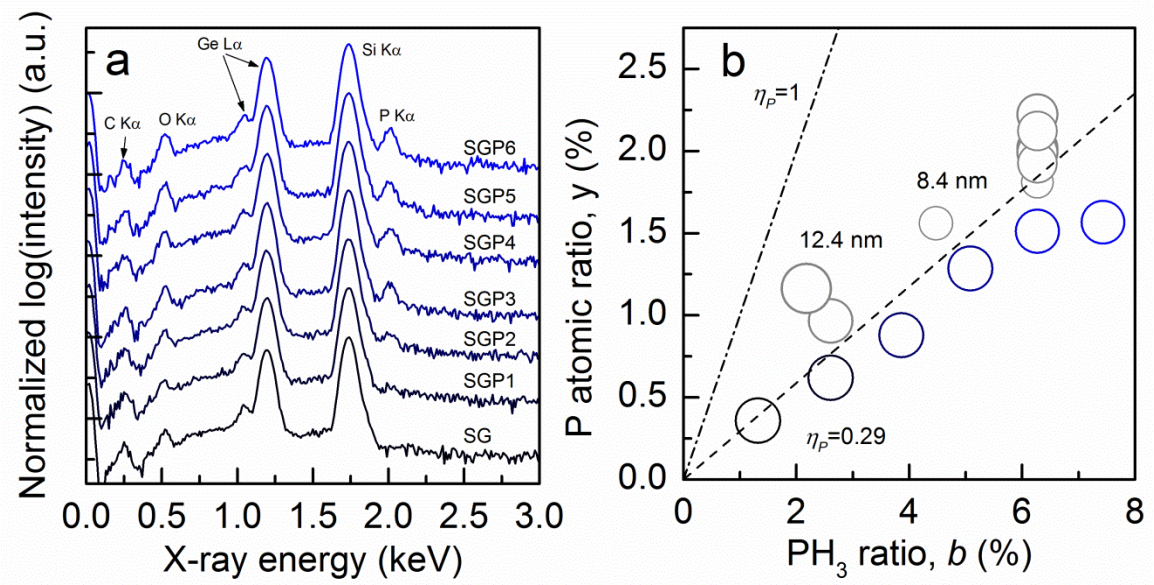

Figure 3.4. $Si_{1-x}Ge_xP_y$ ratio of plasma produced SiGeNCs. (a) EDX spectra for P-doped SiGeNC films, normalized to the Si Kα peak and shown in log scale. Spectra are offset vertically for clarity. (b) Atomic P ratio, y, measured by EDX for varying PH_3 ratio, b. Included is a straight line fit to the data, estimating an incorporation efficiency, η_P = 0.29, and a line indicating η_P = 1 for reference. The size of the bubble indicates the size of the NC measured using XRD, and the largest and smallest sizes are included for reference. The blue shaded bubbles correspond directly to the SGP samples plotted in (a). The grey bubbles indicate additional samples not show in (a).

On the other hand, the B Kα line is less easily distinguished at 0.18 keV due to several factors. Firstly, the B Kα peak resides near the very intense zero-energy peak, making it difficult to distinguish. Secondly, the C Kα peak also resides very near B, as shown in Figure 3.5(a). In fact, this is a significant source of uncertainty in the measurement of B incorporation due to the overlap of B and C integration limits imposed by the NORAN System Six EDX spectrometer. During the measurement, the system dynamically adjusts the integration limits, however in all cases the B and C regions overlap, i.e. 0.121 – 0.249 keV for B, 0.195 – 0.369 keV for C. Therefore, even small amounts of C lead to an overestimation of the B concentration. Hence, validation of the B measurement is necessary before interpreting the results properly. This was accomplished by first measuring a standard boron nitride sample to calibrate the instrument properties for measuring large concentrations of B, and then with an undoped SiGe sample to calibrate to zero B. The sample was measured at several locations to form a mean concentration for the sample. The analysis from the undoped sample showed 3.5% B, which can be attributed to the above errors, and was subsequently subtracted from all other measurements. The data in

Figure 3.5(b) shows that over a fairly large range of c^* the integrated B remains approximate linear, with a slope indicating η_B = 0.16 ± 0.010. This value agrees nicely with the data presented in Pi *et al.*[32] for B-doped SiNCs, however is about a factor of 2 lower than the value calculated in Chapter 2 for the same range of c^*. Unfortunately, this discrepancy could be associated with the uncertainty in the measurement and would require more statistically relevant data validated with a better measurement standard. Electrical measurements would also provide useful information for estimating the true atomic B concentration.

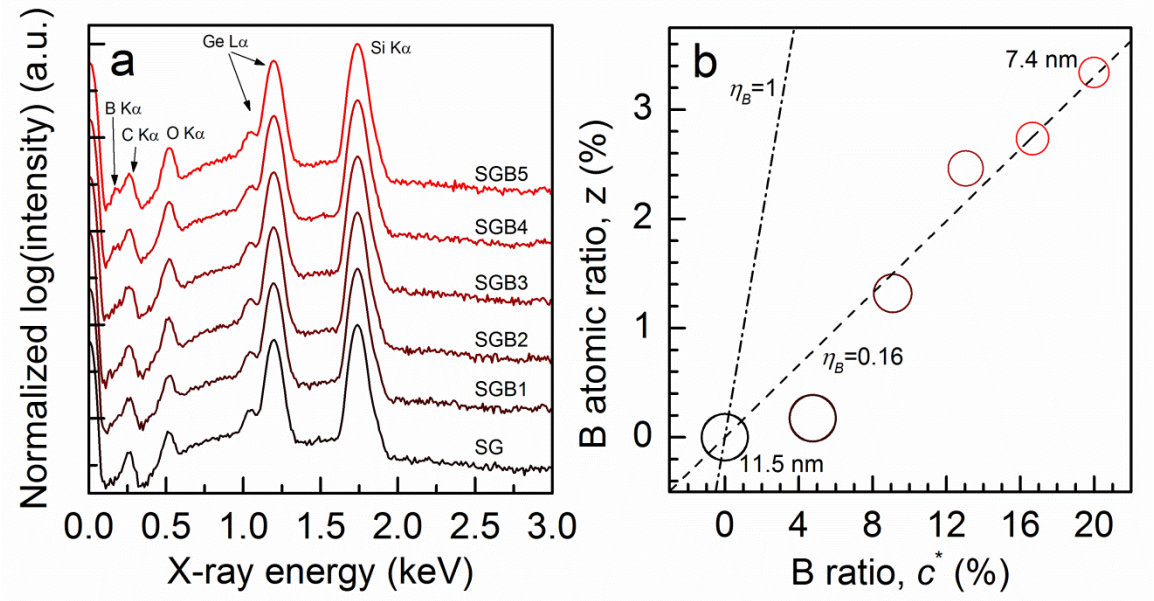

Figure 3.5. $Si_{1-x}Ge_xB_z$ ratio of plasma produced SiGeNCs. (a) EDX spectra for B-doped SiGeNC films, normalized to the Si Kα peak and shown in log scale. Spectra are offset vertically for clarity. (b) Atomic B ratio, z, measured by EDX for varying B ratio, c*. Included is a straight line fit to the data, estimating an incorporation efficiency, η_B = 0.16, and a line indicating η_B = 1 for reference. The size of the bubble indicates the size of the NC measured using XRD, and the largest and smallest sizes are included for reference. The red shading corresponds to the SGB samples plotted in (a).

FTIR measurements reveal the arrangement of Si and Ge on the NC surface. Figure 3.6 illustrates this concept by comparing the FTIR spectra of several different types of pure, alloyed, and doped NCs. Undoped SiNCs and GeNCs exhibit surface hydride vibration modes common to their respective materials. The FTIR spectrum from SiGeNCs consists roughly of the summation of the individual spectra, and Table 3.4 identifies key FTIR peak positions for several relevant chemical bonds. However, three peaks are resolved for the Si-H_x stretching modes,

while only two Ge-H_x modes appear at slightly lower wavenumbers. It is well known that highest order Si hydride stretch, Si-Si-H_3, can be removed from the surface of SiNCs by heating to low temperatures (< 400 °C) in a vacuum or through plasma heating due to large power coupling.[33–35] Already, it appears as though temperatures sufficient for Si-Si-H_3 desorption were achieved in the plasma due to the reduced peak height at 2136 cm^{-1}, therefore it may be concluded that the Ge-Ge-H_3 species was similarly desorbed. Little information exists in the literature regarding the Ge-Ge_{3-x}-H_x desorption properties, so this interpretation remains uncorroborated. From this undoped SiGeNC spectra, the fraction of surface sites can be estimated as $F = A_{Ge\text{-}H}/(A_{Ge\text{-}H}+A_{Si\text{-}H})$ where $A_{Si\text{-}H}$ and $A_{Ge\text{-}H}$ represent the integrated area under the Si and Ge hydride stretches, respectively. Curiously, the fraction of Ge surface states estimated in this fashion (F ~ 0.32) is much larger than the estimated atomic fraction from EDX measurements (x ~ 0.22). This result indicates that Ge segregates to the surface of the NC; however, since some of the Ge-H vibrations are not counted, the actual value of F might be even larger. Nevertheless, the degree of segregation must be fairly small such that XRD does not detect two separate phases.

Furthermore, FTIR measurements reveal that $Si_{0.8}Ge_{0.2}$ NCs also exhibit similar spatial distributions of dopants as the P- and B-doped SiNCs discussed in Chapter 2, likely in part due to the predominant fraction of Si within in the NCs. For P-doped SiGeNCs, a small, broad peak at 2279 cm^{-1} (Si-P_x-H_y stretch)[36] appears, almost identical in position and breadth as the same peak observed in P-doped SiNCs discussed in Chapter 2. This indicates that most of the P is likely bonded to the Si atoms at the SiGeNC surface instead of the Ge atoms. If P was evenly distributed among the Si and Ge surface atoms, a significant broadening and potential peak shift would be observed. Furthermore, as shown in Figure 3.7(a) the appearance of the peak at 2279 cm^{-1} corresponds to a relative reduction of the surface Ge-H stretching mode intensity, indicating that the P replaces Ge surface atoms, consistent with P segregation to the surface of the SiGeNC. However, the relative increase of the P surface stretch appears insufficient to account for the relative decrease in the Ge surface stretches. To explain this, the effect of the H_2 which dilutes the PH_3 must be considered. As more PH_3 (15% in H_2) is added to the plasma, the

intensity of the Si hydride stretches also increases, indicating a large source of atomic H is available in the plasma. This type of plasma is well-known for etching Si, but may also efficiently etch Ge preferentially from the SiGeNC surface. A literature review for H_2 plasma etch rates for Ge turned up no results, implying this may be an unexplored phenomena.

For B-doped SiGeNCs, a feature appears at 1365 cm^{-1} attributable to either amorphous B-H or B-O bonds[37] however a new peak appears at 1840 cm^{-1} which is not identified in the literature. This peak also appears in B-doped SiNCs, but not in amorphous B particles. The peak increases with increased B_2H_6 flow as shown in Figure 3.7(b), and appears at lower wavenumbers than the other heavier species stretching modes, indicating that this peak may represent $Si\text{-}B_x\text{-}H_y$ stretching vibrations. Additionally, B-doped SiGeNCs retain approximately the same distribution of Si-H and Ge-H stretches, indicating that the B is either incorporated mainly in the core of the SiGeNC or that amorphous B particles form and act as a sink for atomic H. In fact, the peak at 1365 cm^{-1} attributed to amorphous B-H peaks also appears in FTIR spectra of particles produced with exclusively B_2H_6 flow, as discussed in Chapter 2.5.1. Furthermore, the peak at 2560 cm^{-1} has also been associated with B-H stretching vibrations,[37] supporting the idea of H absorption by amorphous B. These results indicate dopant incorporation and segregation of B or P from the plasma into a SiGeNC is similar in nature to SiNCs.

Table 3.5. Selected FTIR peak assignments for P- and B-doped SiGeNCs.

Species	*cm^{-1}*	*Species*	*cm^{-1}*	*Species*	*cm^{-1}*	*Species*	*cm^{-1}*
$Si\text{-}Si_3\text{-}H$	2086	***$Ge\text{-}Ge_3\text{-}H$***	1977	***a:B-H, B-O***	1365	***$Si\text{-}P_x\text{-}H_y$***	2279
$Si\text{-}Si_2\text{-}H_2$	2112	***$Ge\text{-}Ge_2\text{-}H_2$***	1992	***$Si\text{-}B_x\text{-}H_y$***	1840		
$Si\text{-}Si\text{-}H_3$	2136	***$Ge\text{-}Ge\text{-}H_3$***	---	***B_2H_6***	2524		

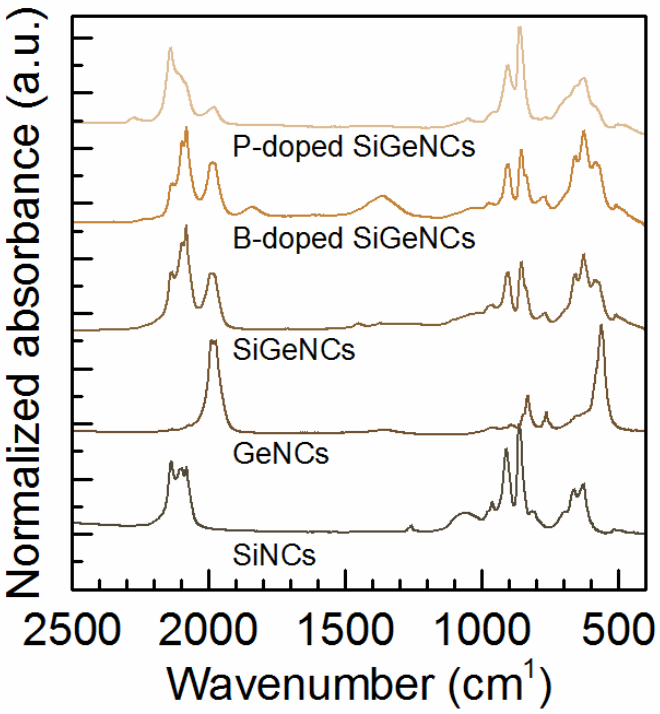

Figure 3.6. FTIR spectra of undoped SiNCs, undoped GeNCs, undoped SiGeNCs, B-doped SiGeNCs, and P-doped SiGeNCs. Peaks are identified in Table 3.5 for a variety of Si, Ge, P, and B species. Spectra are normalized and offset vertically for clarity.

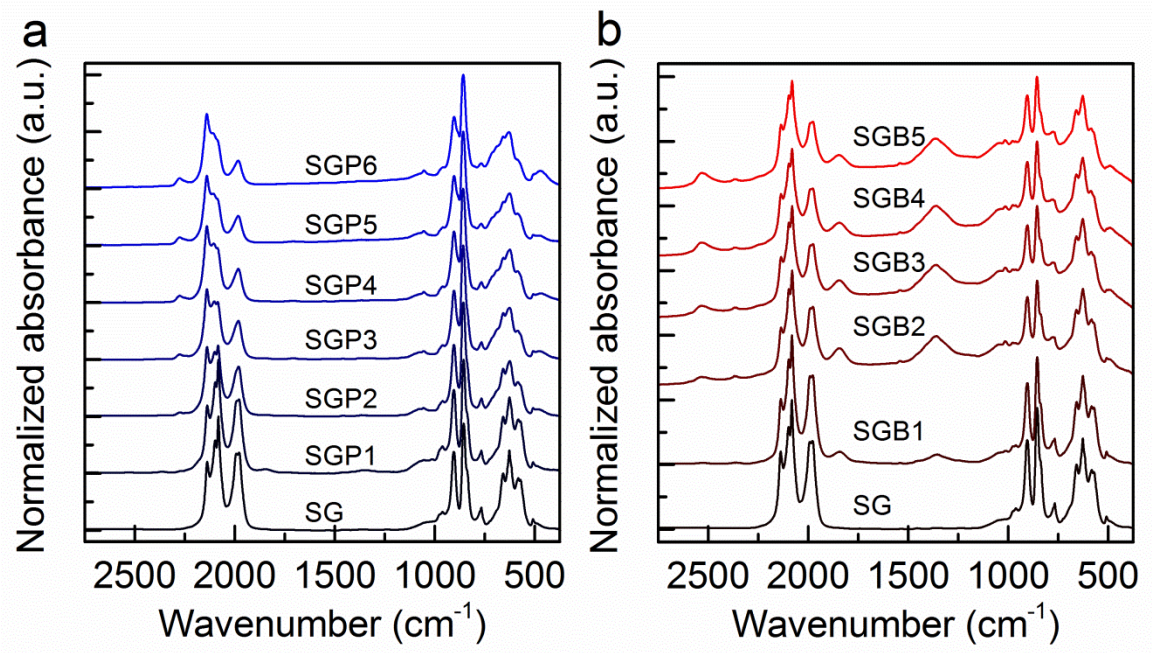

Figure 3.7. FTIR spectra of P- and B-doped SiGeNCs. (a) P-doped SiGeNCs and (b) B-doped SiGeNCs for ranges of dopant gas flows. Spectra are normalized and offset vertically for clarity. The shading and coloring correspond to data shown in Figs 3.4-5.

3.3.3. UNIFORM THIN FILM REPRODUCIBILITY

Considerations regarding optimal SiGe alloy ratios and doping concentrations dictate the composition and structure of the plasma-produced doped SiGeNCs. However, optimization of the laser-annealing and measurement post-processes requires the reproducible production of uniform thin films. Two keys aspects needed to be controlled: 1) variations within a single film should be minimized (intra-film), and 2) variations between different films should be minimized (inter-film). Point 1 is important because small intra-film variations cause difficulties in the laser annealing process, such that the laser power necessary to anneal the entire thickness of the film needs to be dynamically adjusted. Since the laser power is adjusted manually and there was no way to identify *in-situ* if the entire film was annealed, variations such as this would be difficult to account for. Furthermore, thickness variations make the calculation of thermoelectric properties difficult since most models assume a flat profile with a constant thickness. Essentially, point 2 is important for the same reasons. Laser annealing conditions optimized for one film should be applicable to other films made under the same plasma conditions. Moreover, to compare property measurements, the inter-film variation should be minimal.

Reducing each type of film variation required two different approaches. Figure 3.8(a) shows a photograph of two films synthesized under identical conditions displaying a prime example of inter-film variation. The right-hand film was fabricated immediately after the left-hand film, and the missing region of the film is a shadow from additional substrates loaded on the glass. In this case, the variation resulted from unexpected changes in the synthesis conditions during a single deposition. It is clear to see that the left-hand film has a much thicker edge than the right-hand film. Overall, this would be unacceptable for laser processing. The pressure of the synthesis chamber gradually increased during the four minute deposition required to deposit this film. This is most likely due to the nozzle clogging during a deposition from large amounts of NCs attaching to the nozzle walls. Unfortunately, there is no way to confirm this without *in situ* visual confirmation, as the high-pressure, high-flow N_2 purge process required to open the reactor and

remove the nozzle for inspection likely blows away any NCs stuck to the nozzle wall. However, two techniques were observed to reduce clogging and reduce inter-film variation. First, the SiH_4 and GeH_4 flow rates can be reduced, leading to reduced NC density and thereby extending the usefulness of a clean nozzle. This technique only works by extending the characteristic time for clogging past the required deposition time. In between depositions, an Ar or N_2 puff can be used to clear most of the clog. A better way to reduce clogging is to simply increase the nozzle width. A nozzle width below 0.3 mm leads to rapid clogging and pressure changes, however, a nozzle width greater than 0.5 mm leads to much more gradual pressure increases during a deposition run. The explanation for this result remains unexplored, but it will likely be related to the gas properties and the nozzle wall surface in the smallest region of the nozzle. A better nozzle would have fewer sharp edges, a polished surface, and possibly be treated with a non-stick coating to prevent NC attachment. A byproduct of increasing the nozzle width was a reduction of the intra-film variation displayed in Figure 3.8(b) as vertical streaking in the films. These films were fabricated by passing the particle beam over a region of the glass, locking it in place, modifying the Ar carrier flow in real-time, and then continuing the deposition. The dark horizontal lines represent the location where the sample was locked in place while conditions were modified. It was observed that by changing the Ar flow, the position of the streaks could be changed, however no condition was found that eliminated the streaking. Instead, the position and intensity of the streaking decreased by increasing the nozzle width.

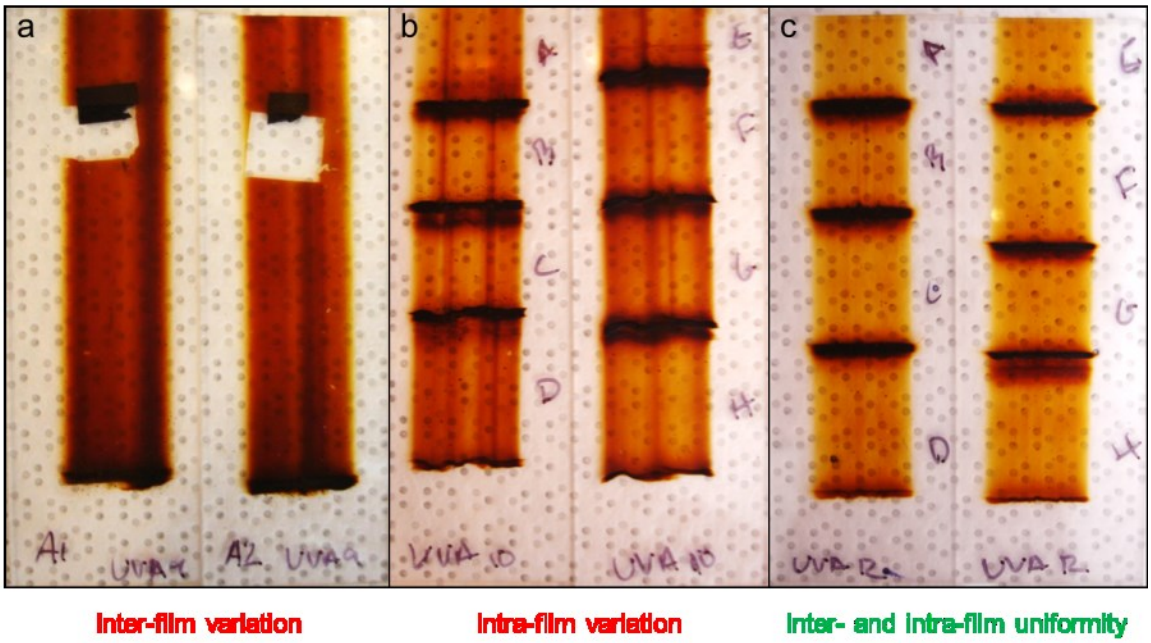

Figure 3.8. Doped SiGeNC film deposition variation. Examples of (a) inter- and (b) intra-film variation, and (c) an example of combined inter- and intra-film uniformity. Vertical streaking is observed in (a) and (b), but not in (c). The dark horizontal lines show where the manual feedthrough stopped while plasma conditions were changed.

Unfortunately, opening the nozzle to reduce film variation will have a direct impact on the NC synthesis by altering the pressure in the synthesis chamber simultaneously. Since the nozzle resides between the plasma reactor and the deposition chamber, and essentially acts as a flow throttle, it dramatically impacts the flow conditions in each chamber. The most general effect of increasing the nozzle width is to lower the synthesis pressure, which in turns lowers the residence time of NCs in the plasma, leading to smaller NCs. More subtly, changes in the synthesis pressure could lead to significant differences in the NC heating, surface chemistry, and doping efficiency. Therefore, to reduce clogging in the nozzle without drastically changing the nozzle geometry, a different approach was used to produce the very uniform films displayed in Figure 3.8(c). This film was fabricated when the plasma electrodes were placed near the top of the reactor tube, such that the distance between the afterglow of the plasma and the nozzle was in excess of 8 inches. Remarkably, when the electrodes were moved to a lower position, such that the distance between the plasma afterglow and the nozzle was virtually eliminated, the film structure changed significantly, as shown in Figure 3.9(a,b). Furthermore, both types of film

variation were practically eliminated, *and* pressure fluctuations during synthesis were reduced significantly. But how could such a simple change in reactor geometry affect such a large change in macroscopic and microscopic structure? It is hypothesized that by reducing the amount of time the particles travel between the plasma and nozzle reduces the degree of agglomeration which can occur. Therefore, instead of large, agglomerated clusters flowing through the nozzle and impacting, the process more closely follows that of individual particles impacting. Calculations of the Stokes number in the downstream region of the deposition reactor indicate under conditions typically measured, single particles are likely too small to impact, and should follow the gas flow lines. This is related to the Stokes drag on a particle, which for a sphere is proportional to the particle diameter. Drag forces on agglomerates roughly scale with some defined measure of agglomerate diameter.[38] In this case, the drag forces are causing the particle to relax to the gas flow streamlines, but its inertia is keeping it moving in a straight line, and scales with the diameter cubed. As a result, as the size of the agglomerate increases so does its characteristic stopping distance with the square of the diameter (given constant velocity). Likewise, if larger sized particles are assumed in the impaction, then the Stokes number would accurately predict the likelihood of impaction. However, this analysis is based on the assumption of particles/agglomerates leaving the nozzle with equal velocity. Such an assumption would require the residence time of the agglomerate within the nozzle to be sufficiently long such that all the momentum from the gas flow was coupled to the agglomerate. Consequently, this momentum coupling would be related to the drag force in the same way the stopping distance is. Suddenly it becomes obvious that the impaction process depends heavily on the particle size and shape, and in the absence of any information, only qualitative descriptions can be made. Such an analysis is beyond the scope of this thesis and was unnecessary to meet the required design conditions. Nonetheless, a better understanding of the relationship between particle agglomeration and impaction physics would allow for a more complete and robust thin film deposition process.

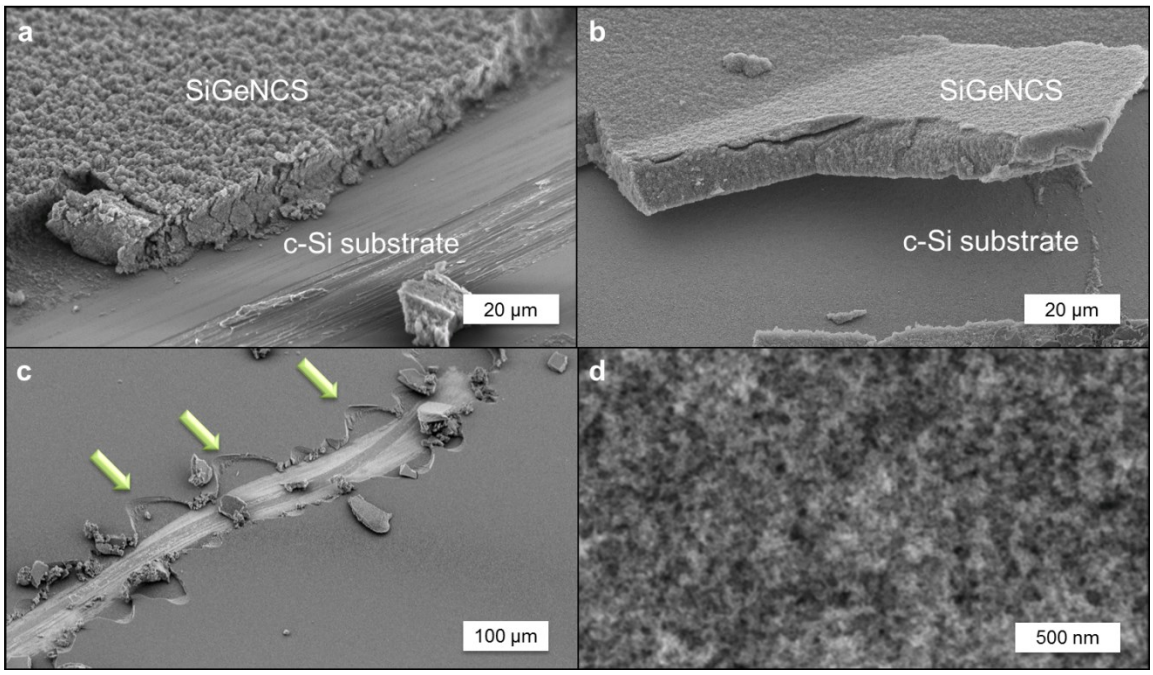

Figure 3.9. SiGeNC film structure. High angle SEM images of SiGeNC films (a) electrodes were placed far from impaction nozzle, (b) near impaction nozzle. (c) Low magnification of (b) where a scratch is visible, arrows indicate fracture features found in dense, glassy films. (d) High magnification of (b) shows porous, nanostructure of SiGeNC films.

More advanced thermoelectric architectures, such as 2D quantum wells and modulation doped matrices, require nanostructures of varying composition and structure to be placed at precise locations within the bulk of the material. The layering technique used in Section 3.3.1 to produced films with two phases can be taken further with the impaction process as a way to engineer nanostructured films which may be suitable for advanced thermoelectrics. As a demonstration of the simplicity involved with this technique, two films were produced with multiple layers of Si and Ge NCs (not alloyed here). Figure 3.10 displays each of these films, with cross-sections in the inset. These films were fabricated without ever removing the samples from the plasma chamber, and require no special processing for each layer to adhere to its predecessor. The porosity of the films induces some unevenness in the layers, but this could be reduced with further optimization. Furthermore, these films were produced without any special metering or integrated flow controls. The addition of a small LabVIEW program to control the gas flows and feedthrough linear velocity would significantly improve film quality. Nevertheless, this illustrates the power of such a deposition system, such that doped layers could also be cycled in

occasionally to preferentially dope single layers for a modulation doping scheme. The limiting factor would be cross contamination from using a single plasma reactor to process each type of NC, which could be eliminated by having multiple synthesis reactors feed into a single deposition chamber through multiple nozzles. Due to time and budget constraints, a next-generation reactor such as this was not built, but holds excellent potential for further research.

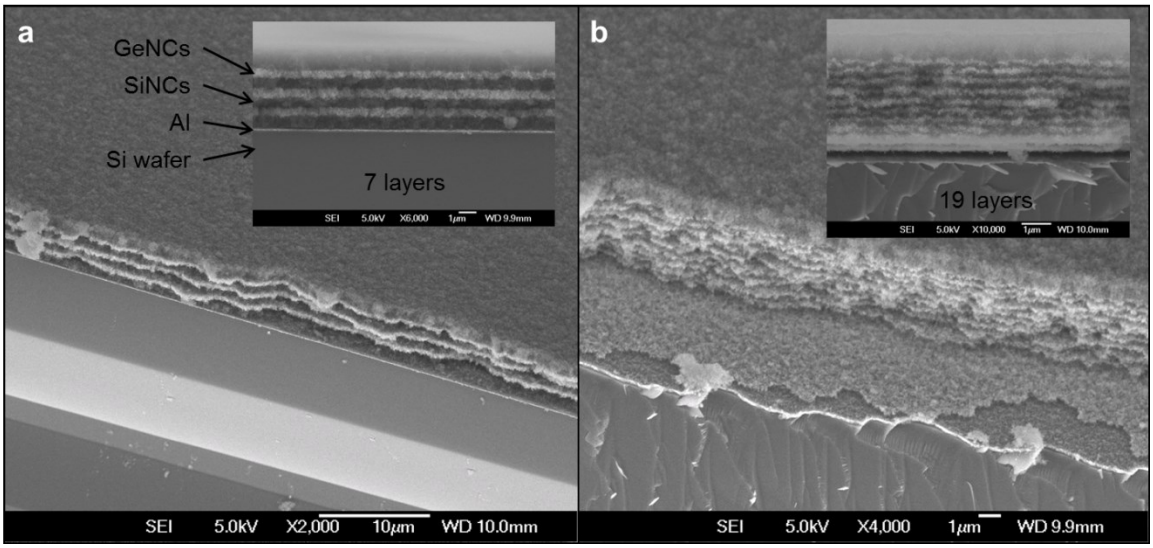

Figure 3.10. Layered SiNC/GeNC films. High angle SEM images of SiNC/GeNC films with (a) 7 and (b) 19 alternating layers of SiNCs (darker film) and GeNCs (lighter film). Inset: cross-section showing even spacing of each layer. Each film was deposited in an Al-coated Si wafer, and the top SiNC layer was deposited extra thick as a barrier layer for oxidation. The film in (b) can be seen to delaminate from the Al with the first SiNC layer cracking away from subsequent layers.

3.4. PRELIMINARY RESULTS – LASER SINTERING

After deposition, SiGeNC films were transferred to the University of Virginia (UVA) for additional processing by Ph.D. candidate Tyson Baldridge. "As-deposited" films remain relatively porous compared to other high-performance nanostructured thermoelectric materials, i.e. greater than 95% of the bulk density. For instance, the SiGeNC film shown in Figure 3.9(b) appears dense at one scale (Fig 3.9(c)), but remains porous at the nanoscale (Fig 3.9(d)). This type of porosity advantageously reduces κ, however extremely porous materials also have very low σ. Unfortunately, most methods for reducing porosity involve high temperature annealing or high

pressure, which tend to also increase the grain size, thereby negating the gains made in reducing κ.[14] Therefore, laser annealing was used to densify the film to reduce the porosity for increased σ, while maintaining small grain boundaries without sacrificing κ. Under the appropriate conditions laser annealing can be a very non-equilibrium process, such that the laser light is locally absorbed in only the SiGeNC film and local heating reduces out-diffusion of dopants from the film. Additionally, laser annealing is more convenient for *in-situ* film annealing and could be used to build multiple, high density layers from simultaneously impacted and annealed SiGeNCs. Our goal was to investigate the viability of laser annealed SiGeNCs as a high-performance thermoelectric material as a proof-of-concept. Included are preliminary results reported from UVA regarding laser annealing. Figure 3.11(a) shows a schematic of the laser annealing system, which consists of a 940 nm CW diode laser (Jenoptik JOLD-250-CPXF-2P2) scanned over a sample by the use of an x-y stage integrated with a LabVIEW program. The laser beam yields 250 W at a spot size of 800 μm. A 600 ampere induction heater surrounding the substrate provides additional heating during the laser annealing process. Figure 3.11(b) shows a film in which the laser power is insufficient to cause any noticeable change in the surface structure of the film, compared to the film in Figure 3.10(a). When the power is increased, micrometer-sized spheres begin to develop on the surface of the film, as show in Figure 3.11(c). By optimizing the laser power and the dwell time through trial and error, a significant change in the film structure was observed, while maintaining a smooth surface, as shown in Figure 3.11(d).

EDX mapping determined the composition of the spheres which formed under high laser power conditions deposited on glass. As shown in Figure 3.12, Ge shows up only in the spheres and not in the surrounding film. Since very little oxide shows up in the spheres, it can be inferred that most of the electron beam is absorbed in the sphere before it reaches the substrate; therefore, most of the Si which appears in the spheres is actually alloyed with the segregated Ge. Point measurements indicate that the laser annealing drastically changes the chemical composition of the sphere to a Ge rich material, ~ $Si_{0.2}Ge_{0.8}$.

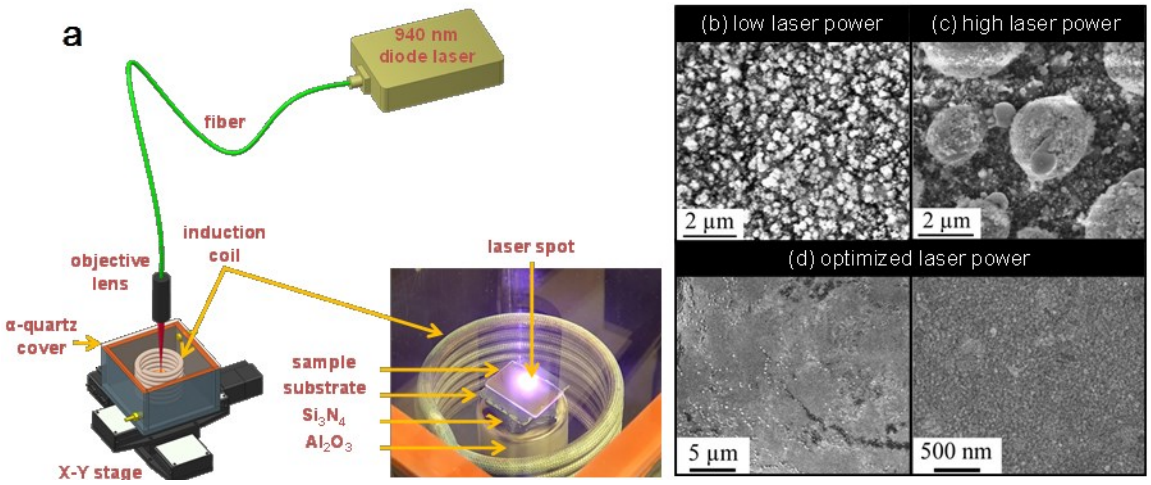

Figure 3.11. Preliminary results of laser annealing collaboration. (a) Schematic of laser annealing process used by Tyson Baldridge at the University of Virginia, includes a 940nm laser diode, an inductive heater, and a translating stage for scanning the focused laser beam. (b-d) SEM images taken by Tyson Baldridge of SiGeNC films after laser annealing under conditions of (b) low power, (c) high power, and (d) optimal power at low and high magnification.

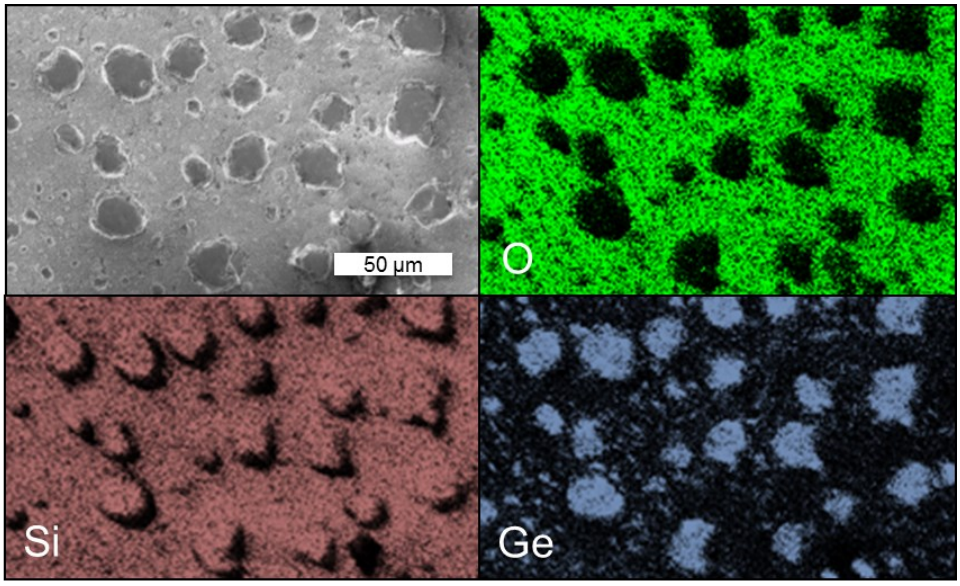

Figure 3.12. EDX mapping of laser annealed SiGeNC film. (upper left) SEM image of SiGeNC film deposited on SiO2 substrate exhibiting significant segregation after laser annealing. EDX maps of O (upper right), Si (lower left), and Ge (lower right). The dark areas in the Si map are an artifact of the measurement from electron shadowing. Scale bar equal for each image. EDX mapping was performed by DJR.

At this point, several measurements are underway to further characterize the annealed films, and evaluate the thermoelectric properties of the finished materials. Further laser annealing optimization is being performed at UVA. Preliminary results indicate that the choice of substrate

dramatically affects the final product. For instance, Si wafers work well for creating a film which is well adhered to the substrate, however electrical measurements become challenging since the SiGeNCs and dopants easily diffuse through bulk Si, thereby making the electrical thickness of the material difficult to ascertain. On the other hand, substrates such as AlN and SiC show promise if the thermal expansion coefficients can be matched, or annealing-induced strain can be reduced. Nevertheless, the plasma synthesis and gas-phase impaction have been shown to deliver good quality films for further densification and processing, providing an excellent platform for which to create nanostructured thermoelectric materials. Furthermore, doping of SiGeNCs has been demonstrated for both n- and p-type materials, strengthening the potential for this material and process. More advanced thermoelectric architectures are possible through layering of materials, but the full potential of this process will require further experimentation.

3.5. REFERENCES

(1) Bell, L. E. *Science* **2008**, *321*, 1457–61.

(2) Vineis, C. J.; Shakouri, A.; Majumdar, A.; Kanatzidis, M. G. *Advanced Materials* **2010**, *22*, 3970–80.

(3) Zebarjadi, M.; Esfarjani, K.; Dresselhaus, M. S.; Ren, Z. F.; Chen, G. *Energy & Environmental Science* **2012**, *5*, 5147.

(4) DiSalvo, F. J. *Science* **1999**, *285*, 703–706.

(5) Snyder, G. J.; Toberer, E. S. *Nature materials* **2008**, *7*, 105–14.

(6) Slack, G. A. In *CRC Handbook of Thermoelectrics*; Rowe, D. M., Ed.; CRC Press: Boca Raton, Fl, 1995; pp. 407–440.

(7) Minnich, A. J.; Dresselhaus, M. S.; Ren, Z. F.; Chen, G. *Energy & Environmental Science* **2009**, *2*, 466.

(8) Darma, Y.; Takaoka, R.; Murakami, H.; Miyazaki, S. *Nanotechnology* **2003**, *14*, 413–415.

(9) Wijngaards, D. D. L.; Wolffenbuttel, R. F. *IEEE Transactions on Electron Devices* **2005**, *52*, 1014–1025.

(10) Choi, W. K.; Teh, L. K.; Bera, L. K.; Chim, W. K.; Wee, A. T. S.; Jie, Y. X. *Journal of Applied Physics* **2002**, *91*, 444.

(11) Joshi, G.; Lee, H.; Lan, Y.; Wang, X.; Zhu, G.; Wang, D.; Gould, R. W.; Cuff, D. C.; Tang, M. Y.; Dresselhaus, M. S.; Chen, G.; Ren, Z. *Nano letters* **2008**, *8*, 4670–4.

(12) Wang, X. W.; Lee, H.; Lan, Y. C.; Zhu, G. H.; Joshi, G.; Wang, D. Z.; Yang, J.; Muto, A. J.; Tang, M. Y.; Klatsky, J.; Song, S.; Dresselhaus, M. S.; Chen, G.; Ren, Z. F. *Applied Physics Letters* **2008**, *93*, 193121.

(13) Zamanipour, Z.; Shi, X.; Dehkordi, A. M.; Krasinski, J. S.; Vashaee, D. *physica status solidi (a)* **2012**, *209*, 2049–2058.

(14) Bux, S. K.; Blair, R. G.; Gogna, P. K.; Lee, H.; Chen, G.; Dresselhaus, M. S.; Kaner, R. B.; Fleurial, J.-P. *Advanced Functional Materials* **2009**, *19*, 2445–2452.
(15) Ruddy, D. A.; Erslev, P. T.; Habas, S. E.; Seabold, J. A.; Neale, N. R. *The Journal of Physical Chemistry Letters* **2013**, *4*, 416–421.
(16) Erogbogbo, F.; Liu, T.; Ramadurai, N.; Tuccarione, P.; Lai, L.; Swihart, M. T.; Prasad, P. N. *ACS nano* **2011**, *5*, 7950–9.
(17) Joshi, K. U.; Kabiraj, D.; Narsale, A. M.; Avasthi, D. K.; Warang, T. N.; Kothari, D. C. *Surface and Coatings Technology* **2009**, *203*, 2482–2485.
(18) Pi, X. D.; Kortshagen, U. R. *Nanotechnology* **2009**, *20*.
(19) Stoib, B.; Langmann, T.; Matich, S.; Antesberger, T.; Stein, N.; Angst, S.; Petermann, N.; Schmechel, R.; Schierning, G.; Wolf, D. E.; Wiggers, H.; Stutzmann, M.; Brandt, M. S. *Applied Physics Letters* **2012**, *100*, 231907.
(20) Chrastina, D.; Cecchi, S.; Hague, J. P.; Frigerio, J.; Samarelli, A.; Ferre–Llin, L.; Paul, D. J.; Müller, E.; Etzelstorfer, T.; Stangl, J.; Isella, G. *Thin Solid Films* **2013**.
(21) Chino, H. U.; Kamoto, Y. O.; Awahara, T. K.; Orimoto, J. M. *Applied Physics* **2000**, *39*, 1675–1677.
(22) Hicks, L.; Dresselhaus, M. S. *Physical Review B* **1993**, *47*, 727–731.
(23) Zebarjadi, M.; Joshi, G.; Zhu, G.; Yu, B.; Minnich, A. *Nano Letters* **2011**, *11*, 2225–2230.
(24) Yu, B.; Zebarjadi, M.; Wang, H.; Lukas, K.; Wang, H.; Wang, D.; Opeil, C.; Dresselhaus, M.; Chen, G.; Ren, Z. *Nano letters* **2012**, *12*, 2077–82.
(25) Girshick, S. L. *Journal of Nanoparticle Research* **2008**, *10*, 935–945.
(26) Anthony, R. J.; Cheng, K.-Y.; Holman, Z. C.; Holmes, R. J.; Kortshagen, U. R. *Nano letters* **2012**, *12*, 2822–5.
(27) Holman, Z. C.; Kortshagen, U. R. *Nanotechnology* **2010**, *21*, 335302.
(28) Erwin, S. C.; Zu, L.; Haftel, M. I.; Efros, A. L.; Kennedy, T. A.; Norris, D. J. *Nature* **2005**, *436*, 91–4.
(29) Dismukes, J. P.; Ekstrom, L.; Steigmeier, E. F.; Kudman, I.; Beers, D. S. *Journal of Applied Physics* **1964**, *35*, 2899.
(30) Dresselhaus, M. S.; Chen, G.; Tang, M. Y.; Yang, R. G.; Lee, H.; Wang, D. Z.; Ren, Z. F.; Fleurial, J.-P.; Gogna, P. *Advanced Materials* **2007**, *19*, 1043–1053.
(31) Kittel, C. *Introduction to solid state physics*; New York : Wiley: New York, 1976.
(32) Pi, X. D.; Gresback, R.; Liptak, R. W.; Campbell, S. A.; Kortshagen, U. R. *Applied Physics Letters* **2008**, *92*, 2008–2010.
(33) Holm, J.; Roberts, J. T. *Journal of Vacuum Science & Technology A:* **2010**, *28*, 161.
(34) Winters, B. J.; Holm, J.; Roberts, J. T. *Journal of Nanoparticle Research* **2011**, *13*, 5473–5484.
(35) Anthony, R. J.; Rowe, D. J.; Stein, M.; Yang, J.; Kortshagen, U. *Advanced Functional Materials* **2011**, *21*, 4042–4046.
(36) Schrotter, J.; Cardenas, A.; Smaihi, M.; Hovnanian, N. *Journal of Sol-Gel Sci. and Tech.* **1995**, *4*, 195–204.
(37) Saß, M.; Annen, a.; Jacob, W. *Journal of Applied Physics* **1997**, *82*, 1905.
(38) Rogak, S. N.; Flagan, R. C. *Journal of Colloid and Interface Science* **1990**, *134*, 206–218.

4. DOPED SINCS FILMS FOR PHOTOVOLTAICS

4.1. INTRODUCTION

4.1.1. NCS & PHOTOVOLTAICS

In order to surpass the theoretical efficiency limits imposed on single crystal photovoltaic (PV) cells while simultaneously providing low cost alternatives to wafer based cells, it is widely believed that PV devices exploiting nanoscale structures will pave the way.[1–4] At the nanoscale, quantum confinement occurs because the size of the NC begins to approach the length scale related to the underlying quantum mechanics in the bulk material. As a result, the material's optical, mechanical, and electrical properties dramatically change as the material's dimensions are reduced to the nanoscale. A consequence of this effect is that the band gap energy in a pure semiconductor can be tuned strictly by changing NC size.[5–8] This means that by simply changing the size of a material, one can change the frequency of light it absorbs. One way to take advantage of this phenomenon is by creating solar cells with layers of material possessing varying band gap energies thereby efficiently absorbing different regions of the solar spectrum at the same time. In addition, some NCs exhibit a phenomenon, known as multiple exciton generation (MEG).[9] In essence, for one photon absorbed of twice the band gap energy, two excitons are generated instead of one exciton plus thermal relaxation (heat). Such a mechanism could double the generated charge carriers per incoming photon and remains at the forefront of PV research.[10–12] Calculations have been carried out that suggest MEG could increase the maximum PV conversion limit to increase to 38% - 50%, depending on the material.[13,14] More recently, Beard and collaborators claim to observe this phenomenon occurring in Si.[15] In general, observations of such interesting physical phenomena require beginning with high quality and high purity materials. Likewise, rapid and inexpensive deployment of these technologies requires materials suitable for thin film deposition as an alternative to using Si wafers. During Si wafer manufacturing, the handling and processing techniques require 300 μm – 500 μm thick wafers to avoid cracking and damage. However, calculations predict 29% efficiency could be realized with

an 80 μm single crystal Si layer,[16] and 10% efficiency with a 10 μm poly-crystalline Si layer.[17] Due to the indirect band gap of Si, such a prediction represents a good estimate for the upper limit on material thickness. Moreover, thin film technologies enable flexible substrate processing which would even further proliferate the use of PV through increased manufacturing throughput.[18]

The development of materials which satisfy these criteria requires fabrication methods which combine high purity synthesis with rapid thin film deposition. However, despite widespread research interest and numerous synthetic techniques for fabrication, free-standing SiNCs have played a limited role in the nanostructured PV literature. An study published by Kortshagen's group incorporated SiNCs into a conductive polymer to fabricate a hybrid organic solar cell, with efficiency as high as 1.15%.[19] In a different study, researchers used SiNCs from pulverized porous Si dispersed in spin on glass (SOG) to fabricate a down-conversion layer for traditional solar cells.[20] The authors claimed that a 1.2% increase in efficiency was observed with the down-converting layer, as opposed to a SOG layer with no SiNCs embedded. In another study, Green's group sputtered alternating layers of n-doped Si rich oxide (SRO) and SiO_2 onto a p-doped Si wafer.[21,22] They then used a high temperature anneal to precipitate out the NCs, which were confined to the resulting SiO_2 matrix. They showed that for a cell made of 15 alternating layers of 3 nm of SRO, 2 nm of SiO_2, that cells were 10.6% efficient. In a similar study, the same method for fabricating SiNCs was used,[21] however, a p-i-n structure was used instead in an effort to absorb more light in the intrinsic (i) layer. In this case the SiNCs were precipitated from the p-doped and n-doped layers during the high temperature anneal. These cells showed lower performance which was attributed to dopant diffusion during the SiNC precipitation process. In a similar study, SiNCs were spontaneously formed during the deposition of Si nitride films from PECVD.[23] The films were grown on p-type Si wafers to create p-n junction solar cells. SiNC size ranged from 3.3 - 4.8 nm depending on deposition conditions. The study concluded that devices did show a slight PV response, but they attributed overall poor performance to the slow carrier transport in the Si nitride film due to large distances between SiNCs.

Throughout these studies the challenges inherent to processing SiNC films, e.g. low deposition rates, small grain size, low electrical conductivity, high processing temperatures, and difficulties associated with doping NCs often limited the ultimate solar conversion efficiency. Simply replacing a layer of a c-Si solar cell with a SiNC layer will likely not achieve any greater efficiency gains. This is clearly and simply demonstrated by considering the differences in performance between a c-Si solar cell (eff = 25%)[24] and poly-crystalline Si solar cell (eff = 20.4%)[25] – two systems which have been well studied for several years. To use SiNCs properly in a new solar cell structure, factors like quantum confinement effects, low-cost processing, doping, and unrealized device architectures must be addressed. However, a simple device as noted above *can be used* as a testbed for device performance and response during the development of doped SiNC films. Despite modest predicted efficiencies, valuable device physics and material properties can be extracted from such a device architecture.

This chapter details research which develops this testbed by investigating a simple single layer SiNC PV device using P-doped SiNCs. In conventional p-n junction type Si solar cells, a thin (~300 nm) heavily n-type doped emitter sits on top of a thick (~300 μm) lightly p-type doped base layer. As shown in previous chapters, SiNCs can be doped n-type with P to very large concentrations with a plasma synthesis technique. Therefore replacing the emitter layer of c-Si PV device with a P-doped SiNC layer should also produce a solar cell, albeit with much lower performance due to the poly-crystalline nature of the material as mentioned above. Specifically, this chapter examines methods for increasing the density of gas-phase impacted SiNC films to achieve better electrical transport as emitter layers. One method involves post-deposition annealing as an effort to sinter the SiNCs together to form larger grain sizes and reduce surface recombination within the porous SiNC layer. In a different approach, atomic layer deposition (ALD) was used to fill the porous void fraction of SiNC films with a transparent oxide and/or subsequently depositing a conductive, transparent top contact. Hypothetically, the ALD process should passivate surface defects and form a more compact, stable layer without the need for high temperature annealing or SiNC sintering. Cross-sectional SEM images identify the resulting

structure from multiple top contact deposition and infill methods. I-V measurements performed on the different cells reveal the effectiveness of the densification method. Some suggestions for further research and comments regarding device fabrication and measurement are also provided for the next generation of devices. Finally, the last section presents a fitting model for advanced device parameter extraction and identification of non-idealities within the device. The non-idealities in the devices impose new models for fitting the PV devices in order to better understand the device physics.

4.1.2. PV PERFORMANCE FUNDAMENTALS

Before proceeding, a brief description of PV performance characterization will help to clarify further discussion and results for those not familiar with PV characterization. In general, a p-n junction can accurately describe many PV devices, and the theory has been thoroughly developed for many years with excellent coverage given by Sze.[26] Very briefly, a p-n junction is formed when two oppositely doped semiconductors are brought in mechanical contact with each other. The doping in each material offsets the Fermi energy from the center of the band gap, and when the materials come to equilibrium with each other, the Fermi levels align. This causes the conduction and valence band edges to bend, and the region where bending occurs is known as the depletion region. The band bending creates a built-in voltage, V_{bi}, which is fundamental to the operation of a solar cell. Excitons created from photon excitation are spatially separated from each other by V_{bi}, at which point they can become free carriers and can be used for electrical power. With a few approximations, the p-n junction becomes an ideal diode, and the current-voltage relation is given by:[27]

$$J_{dark}(V) = J_o\left(e^{qV/nk_bT} - 1\right) \tag{4-1}$$

where J_{dark} is the current density for an non-illuminated junction, J_o is the saturation current density, V is the applied bias voltage, k_b is Boltzmann's constant, T is temperature, and n is the ideality factor. For an ideal diode which results from the depletion width approximation, n = 1.

Differences from this model lead to $n > 1$. Illuminating the junction creates a photocurrent, J_L, and the resulting current-voltage relationship for an illuminated junction becomes,

$$J(V) = J_L - J_{dark}(V) = J_L - J_o\left(e^{qV/k_bT} - 1\right) \tag{4-2}$$

As can be seen from equation 4-2, J_L is assumed constant with respect to V for a given material and illumination spectrum. The goal of most PV materials research is to maximize J_L for the known solar spectrum. When V = 0, the second term vanishes,

$$J(V) = J_L = J_{sc} \tag{4-3}$$

where J_{sc} is now defined as the short circuit current density. When J(V) = 0, we can solve for V and define it as the open circuit voltage, V_{oc}, such that,

$$V_{oc} = \frac{k_bT}{q}\ln\left(\frac{J_{sc}}{J_o} + 1\right) \tag{4-4}$$

It is evident that V_{oc} increases logarithmically with the photocurrent density and the inverse of the diode saturation current density. The diode saturation current density is representative of how well the p-n junction forces current in one direction, or in other words, its "idealness". The device properties, J_{sc} and V_{oc}, are two of the main parameters used in characterizing device performance. The other two are power efficiency, η_{eff}, and fill factor, FF. Power efficiency is simply the ratio of the maximum power density from the cell, P_{max}, to the power input, P_{in},

$$\eta_{eff} = \frac{P_{\max}}{P_{in}} = \frac{J_{\max}V_{\max}}{P_{in}} \tag{4-5}$$

The fill factor is simply a ratio that describes how well the maximum power condition fits the ideal diode assumption, has a maximum value of 1, and is defined as the following ratio,

$$FF = \frac{J_{\max} V_{\max}}{J_{sc} V_{oc}} \tag{4-6}$$

The relation of all these parameters is shown graphically in Figure 4.1. As can be seen from this figure and the above relationships, maximizing J_{sc}, V_{oc}, and FF all contribute towards maximizing η_{eff}. Therefore, these four quantities are the main indicators that will be extracted from the I-V curves for each sample.

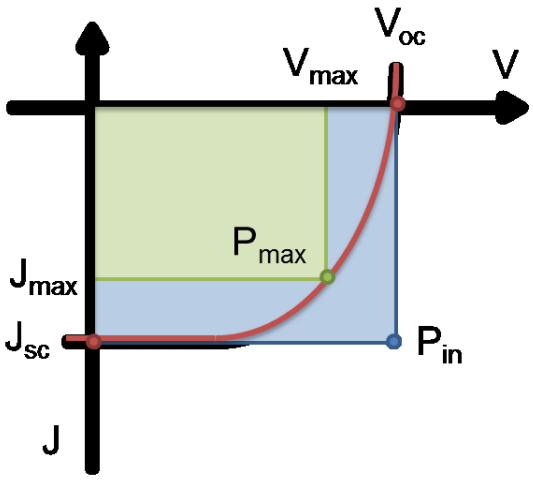

Figure 4.1. Hypothetical current-voltage curve for an illuminated p-n junction solar cell with key performance parameters identified.

4.2. EXPERIMENTAL METHODS

4.2.1. DEVICE FABRICATION OF BASE LAYER, SiNC LAYER, & BACK CONTACT

SiNC/crystalline Si heterojunction solar cells were fabricated by impacting P-doped SiNCs onto B-doped, single-crystal Si substrates (ρ = 10-20 Ω-cm). The substrates were fabricated from a single-side polished wafer, with a thermally grown 300 nm SiO_2 layer. The active area was defined by etching a 3 mm x 3 mm window through the SiO_2 using 10:1 buffered oxide etch (BOE) solution diluted in water. The SiO_2 layer on the back side is removed in the same process. Details of the lithography process used to pattern the active area can be found in the appendix (section 7.1). After the lithography process the Si wafer was diced into 1 cm x 1 cm squares with

a single device centered on each square. The back contact was formed using a CHA SEC 600 electron-beam evaporator to deposit 200 nm of Al at a rate of 0.1 nm/s at room temperature. Immediately before Al deposition, the samples were etched again to remove any native SiO_2 that formed during preparation. After Al deposition, the Al back contact was annealed at 525 °C for 5 minutes under forming gas (5% H_2 in N_2) to form an ohmic contact.

The SiNC films were produced in a flow-through reactor using a 13.56 MHz capacitively-coupled nonthermal Ar-SiH_4 plasma, as described in previous chapters. Table 4.1 outlines standard synthesis parameters for this work. Immediately before SiNC deposition, substrates were etched in 10:1 BOE solution to remove any native oxide which may have formed during processing. Samples were loaded into the SiNC deposition chamber within a few minutes of being etched. In some instances, the SiNC layer was annealed to high temperatures (> 500 °C) under Ar or forming gas (5% H_2 in N_2) after deposition using a rapid thermal annealing (RTA) system. For these samples, the Al back contact was deposited and annealed after the high temperature SiNC anneal. For samples in which the SiNC layer *was not* annealed, the Al back contact was deposited and annealed before SiNC deposition.

Table 4.1. Standard synthesis conditions for P-doped SiNCs for PV devices.

	Unit	***Value***	***Notes***
Ar Flow	sccm	14-17	100%
SiH_4 Flow	sccm	0.5	100%
PH_3 Flow	sccm	0-5	15% in H_2
Pressure	Torr	1.0-1.6	actual
Power	W	110-130	nominal
Tube Diameter	inch	1/0.85	O.D./I.D, quartz
Deposition Time	min	0.5-1	

4.2.2. TOP CONTACT & VOID INFILLING

The top contact (TC) was fabricated from a transparent conductive oxide via two different methods. In one method, an AJA ATC 2000 rf/dc sputtering system was used to deposit 70 nm of indium tin oxide (ITO) at a chamber pressure of 6 mTorr and at sputter power of 250 W, while heating to 150 °C, at a rate ~2.3 nm/s. The ITO target was sputtered in an environment of 20:1

Ar:O_2 to help create a more stoichiometric ITO layer. The second method of top contact deposition involved using a Cambridge Nanotech, Inc. Savannah series atomic layer deposition (ALD) system. With the ALD system, ~ 70 nm of Al-doped ZnO (AZO) was deposited at 180 °C, at a rate of ~ 0.8 nm/s. This is accomplished by alternating pulses of diethylzinc and water vapor to build ZnO layers. For every 15 cycles of the ZnO precursor, a single trimethylaluminum and water vapor cycle was run to dope the ZnO material. Higher doping levels could be achieved by decreasing the number of ZnO cycles between the Al cycle. The combination of the ZnO and Al process was then cycled 28 times to build up 70 nm of AZO.

To fill the voids in the SiNC layer, the ALD system was run using prolonged pulses such that any given pulse is allowed several seconds to saturate and permeate the SiNC matrix before being pumped out of the deposition chamber. This process was run prior to the AZO deposition, but during the same run. Some samples received a 5 nm planar equivalent process of ZnO using the aforementioned process, and some samples received a 5 nm planar equivalent HfO_2 infill process consisting of alternating pulses of tetrakis(dimethylamido)hafnium(IV) and water vapor. Generally, the infill process only requires ~ 20 total cycles. Figure 4.2 illustrates schematics of the four architectures studied in this chapter.

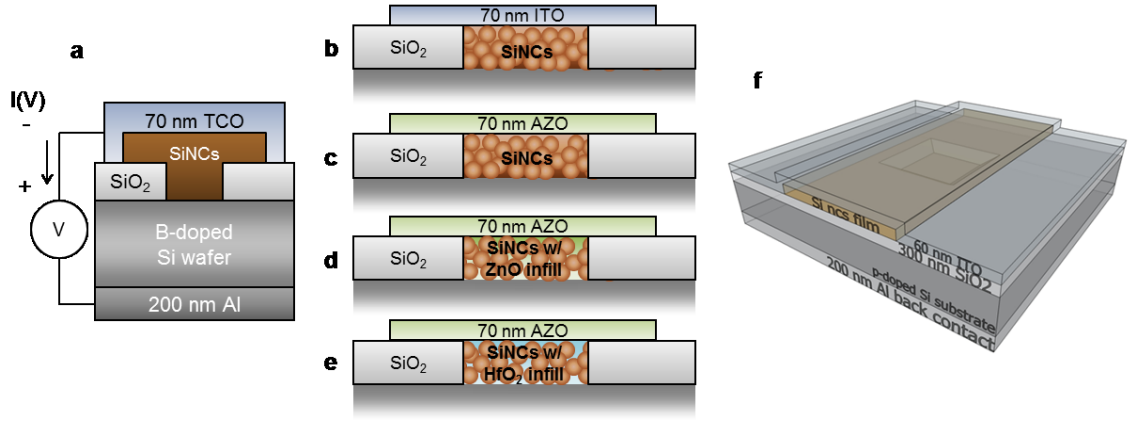

Figure 4.2. SiNC solar cell architectures. (a) generic architecture showing full stack with transparent conductive oxide (TCO) for top contact. (b) sputtered ITO top contact, (c) ALD-deposited AZO top contact, (d) ZnO infill with AZO top contact, (e) HfO_2 infill with AZO top contact. (f) 3D representation of cell showing the active area square underneath the TCO.

4.2.3. SEM

Scanning electron microscopy was performed using a JEOL 6500 field emission gun electron microscope. Samples were stored in a N_2 purged glovebox prior to imaging, and were transferred from the glovebox to the microscope as quickly as possible to minimize air exposure. Samples were cracked using a diamond pen and mounted to a 90° stub for cross-sectional (XS-SEM) analysis. The accelerating voltage was set to ~ 5 kV, and the beam current factor set to ~8-9 to avoid charging the sample. No metallic coatings were used to enhance the imaging.

4.2.4. XRD

The crystalline diffraction pattern was measured using a Bruker-AXS microdiffractometer with a 2.2-kW sealed Cu x-ray source and a Hi-Star 2-D Area Detector. Powder samples were impacted directly from the gas phase onto a piece of glass for mounting in the instrument, and diffraction patterns were recorded at ambient room conditions. One frame centered at $2\theta = 36°$ and $\omega = 18°$ was collected for 5-10 minutes, so as to provide a pattern with good signal to noise ratio. The mean NC diameter was estimated from the reflection broadening using the Scherrer equation.

4.2.5. CURRENT-VOLTAGE (I-V) MEASUREMENTS

The current-voltage (I-V) characteristics of solar cells were measured in air under AM1.5 light at an intensity of 100 mW/cm^2 using a Newport Oriel xenon-arc lamp (P/N 60025) and Keithley 2611A SourceMeter. The light intensity power output was calibrated using a thermopile sensing probe and a radiant power meter (Newport P/Ns: 70268 and 70260). A cell is connected via a copper contact mounted to a vacuum stage for the back contact, and a single needle-point probe for the transparent top contact. Substantial force is applied to the needle to make good contact to the top layer. The SiO_2 layer provides an isolation barrier to prevent the needle from shorting out to the Si wafer. A single scan from -0.5 V to 1.0 V consisting of 401 points is collected with a 50 ms delay between points.

4.3. RESULTS & DISCUSSION – FILM STRUCTURE & DEVICE PERFORMANCE

Preliminary experiments on P-doped SiNC films suggest very low electrical conductivity, σ, even with the presence of dopant. Attempts to increase σ by altering the impaction process to produce a denser layer only show modest improvement in σ. For reference, devices fabricated from "as-produced" SiNC films show very low J_{sc}, which results in low η_{eff} (< 0.05%). As an alternative to modifying impaction conditions, post-deposition annealing may cause SiNCs to sinter, coalesce, or even melt to form very dense layers with appreciably large σ. Furthermore, σ likely trends with the mean NC grain diameter, as larger grains transport carriers more efficiently and possess fewer grain boundaries which scatter or trap carriers. Using the nonthermal plasma synthesis technique to produce SiNCs, the mean NC size can be tuned by adjusting the residence time of the SiNCs in the plasma region. Figures 4.3, 4.4, and 4.5 show the effect of annealing on SiNCs of mean diameter of 16, 5.6, and 8.0 nm, respectively.

Figure 4.3(a) shows a TEM image of spherical free-standing SiNCs produced using low SiH_4 flow rates and very large residence times. A Gaussian fit to the histogram plotted in Figure 4.3(b) predicts SiNCs of 16.0 nm mean diameter (standard dev = 3.8 nm). Al Gunawan provided the TEM image and this author performed the counting statistics using ImageJ software. When impacted on a Si wafer substrate, the film appears fairly smooth as shown in Figure 4.3(c), however, the SiNC films exhibit no noticeable change in film structure upon annealing at temperatures ranging from 500 – 1100 °C for 30 s under Ar, as shown in Figures 4.3(d-g).

Figure 4.4(a) shows XRD patterns from SiNC films prepared under shorter residence times to produce smaller NCs. Using the Scherrer equation, the width of the diffraction peaks estimates the mean NC diameter, assuming a single spherical grain for each NC. Now, annealing smaller SiNCs results in dramatic changes in the mean NC size and film structure. After annealing at 1100 °C for 30 s under Ar, the NC grains grow by an order of magnitude, and after annealing at 1200 °C for 15 s under Ar grow to a size larger than the acceptable range for use of the Scherrer equation (> 100 nm). Figures 4.4(b-d) show XS-SEM images illustrating the remarkable change

in NC structure. The un-annealed film appears porous, with individual NCs almost impossible to resolve. The photograph in the inset shows a corresponding PV device, and the active area of the PV appears faintly through the brown tint of the SiNCs. After annealing, the grain size increases, and at the highest temperature appears to have melted and wetted to the Si substrate. Now the films appear opaque to the naked eye, consistent with an increase in the average scattering diameter of the NC grains. While impressive in appearance, this result agrees with previously reported work regarding the size-dependent reduction in the melting point of NCs.[28–31]

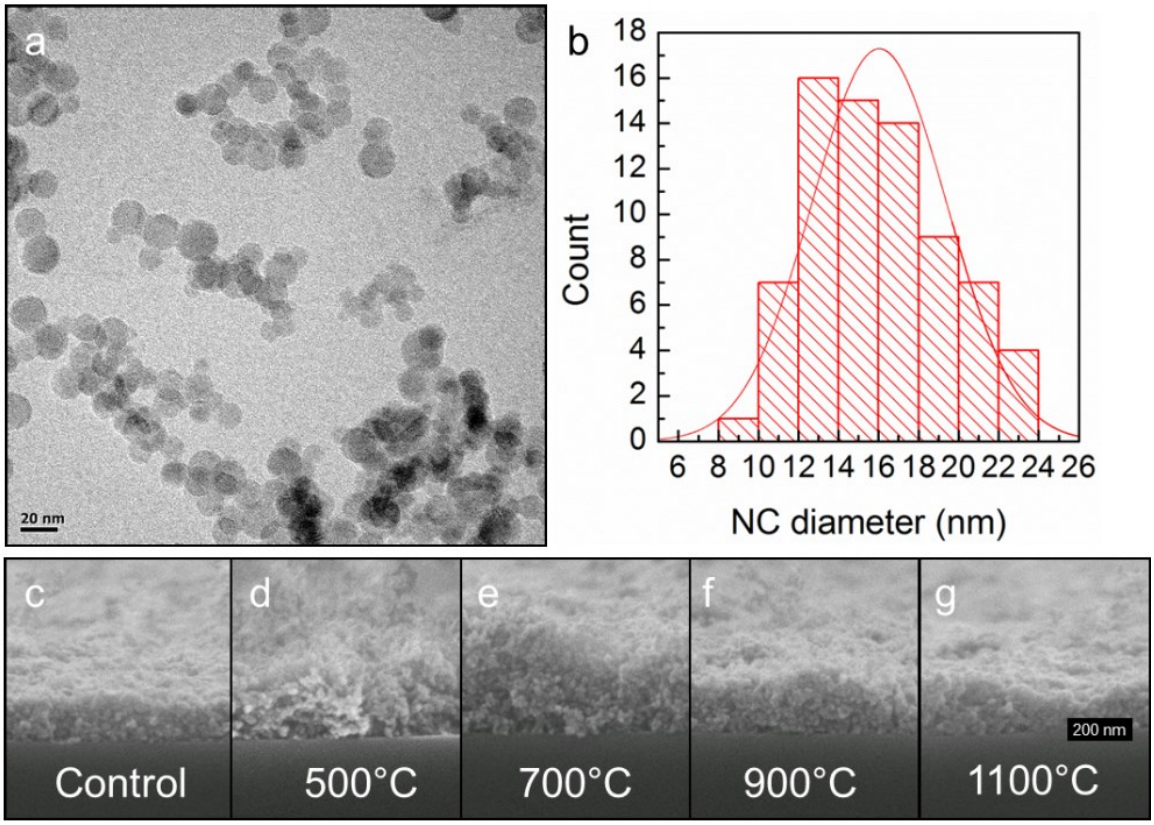

Figure 4.3. Densification of thin films made from 16 nm SiNCs. (a) TEM showing spherical SiNCs (TEM image from Al Gunawan) (b) a corresponding histogram indicating roughly a normal distribution with a mean diameter of 16.0 nm and standard deviation 3.8 nm. XS-SEM images for films of SiNCs (c) before annealing, and after annealing to (d) 500 °C, (e) 700 °C, (f) 900 °C, and (g) 1100 °C. Scale bar for (c-g) all same.

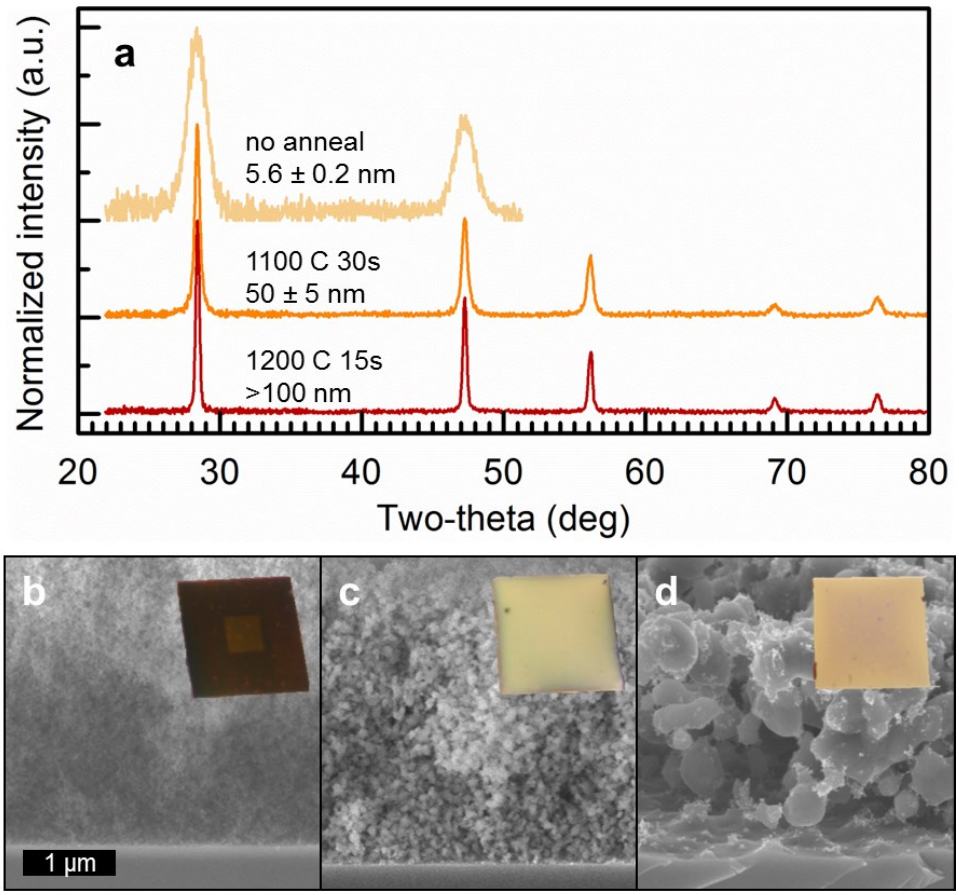

Figure 4.4. Densification of thin films made from 5.6 nm SiNcs. (a) XRD showing patterns for un-annealed SiNCs with a mean diameter of 5.6 nm, and after annealing to 1100 °C and 1200 °C in an RTA under Ar for 15 s and 30 s, respectively. XS-SEM images for (b) un-annealed SiNCs and SiNCs annealed to (c) 1100 °C and (d) 1200 °C. Insets show photographs of the corresponding devices.

The SiNC structure also depends on the annealing environment and the NC surface prior to annealing, as shown in Figure 4.5. Beginning with SiNCs with a mean diameter of 8.0 nm, annealing under Ar produced the largest change in NC size, to ~ 20.8 nm. Figure 4.5(a) shows XS-SEM images displaying the change in film structure for different annealing gases. The dramatic grain growth under Ar annealing can be explained by considering the SiNC surface during annealing. Under forming gas, a significant source of atomic H exists such that the SiNC always remain in a steady-state of H adsorption/desorption. This provides a net H coverage on the SiNC surface, and very few dangling bonds. Under Ar annealing, H desorbs rapidly from the SiNC surface forming dangling bonds. These bonds fulfill themselves with dangling bonds on nearby NCs, forming a “necking” region. This necking region pulls NCs together and allows for

sintering to produce large NC grains.[32,33] Some samples were etched with 10:1 BOE prior to etching. In the case of Ar and forming gas, the etch process made little difference, but etching produced a significant increase in the NC grain size under N_2 annealing. Reactions at the SiNC surface with H and N at these temperatures could also explain the reduction in NC growth as compared to Ar. Additional analysis to identify the resulting structure would help further explain the melting/sintering mechanisms.

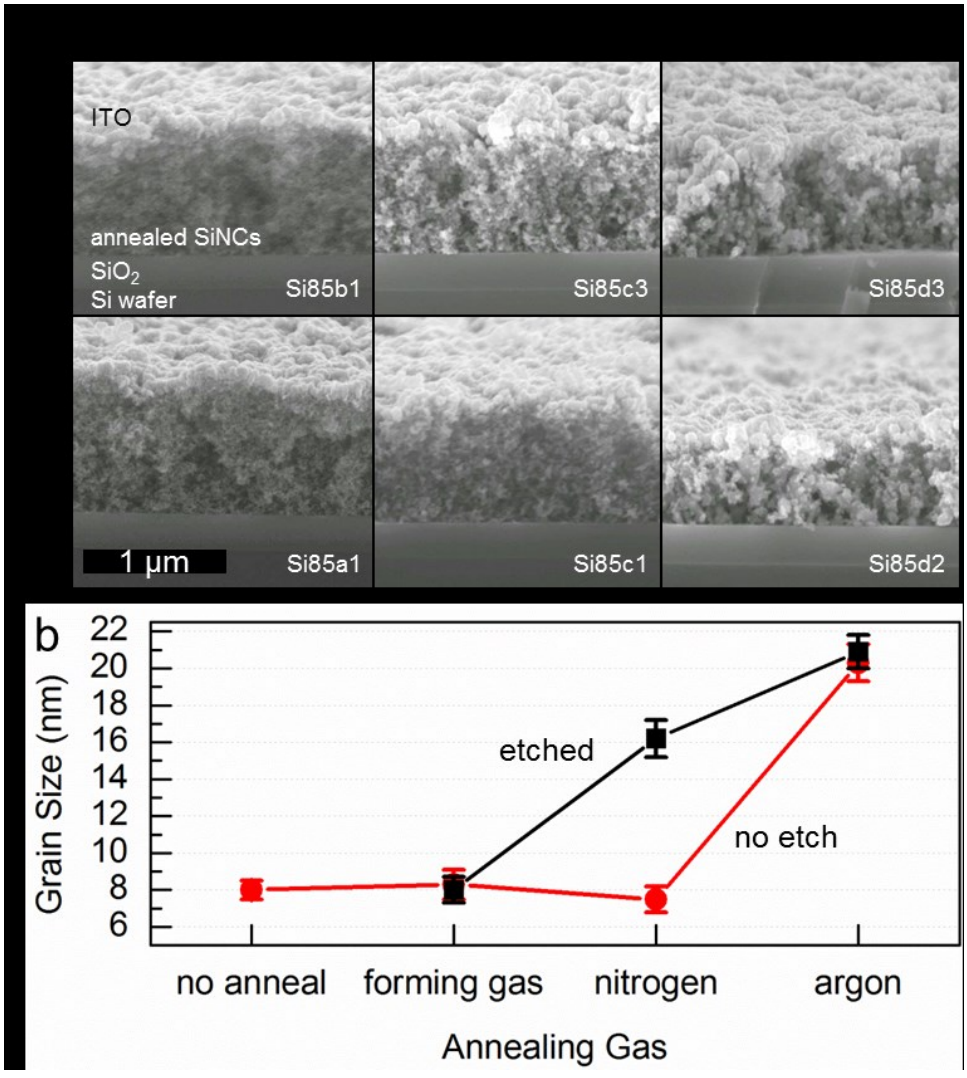

Figure 4.5. Densification of thin films made from 8.0 nm SiNCs under different annealing environments. (a) SEM series showing SiNC films with ITO top contacts for a variety of annealing gas treatments at 1100 °C. The top row of films were etched in 10:1 BOE before annealing, the bottom row of films were not. Scale bar equal for all SEM images. (b) Grain sizes as measured by XRD for each of the films in (a) including the size for an un-annealed sample.

Figure 4.6(a) shows the effect that annealing has on the PV device performance. The cells shown here were sputtered with ITO as a transparent TC. While device performance basically increases with NC grain diameter, the overall performance remained quite low, with η_{eff} < 0.1% in most cases. A cell which had been annealed to lower temperature (525 °C for 60 min) was also included. Low temperature annealing did not increase the NC size, but the device J_{sc} exceeds that of the forming gas process. Some "necking" probably occurs leading to a slight increase in σ, but not enough to affect the SiNC size. Low σ still seems to limit the device performance, likely a result of high film porosity after annealing. As the NC grain size increases, so does the pore size, as shown in the XS-SEM images. As a result, the SiNC films maintained their overall porosity throughout the annealing process. After some optimization and increasing the active area to the standard 3 mm x 3 mm square, the devices performed as shown in Figure 4.6(b), representing the films shown in Figure 4.5. The low FF and linear response at high forward bias indicate that even after optimization, the cells remain largely resistive, likely due to the NC layer and its interfaces with the Si wafer and/or the ITO layer. By passivating the SiNC with additional H using a forming gas anneal after the sintering anneal, the performance increases incrementally. Table 4.2 outlines the performance parameters for the two cells shown in Figure 4.6(b). Performance at this level remains too low for commercialization, and incremental increases only appear possible through optimization

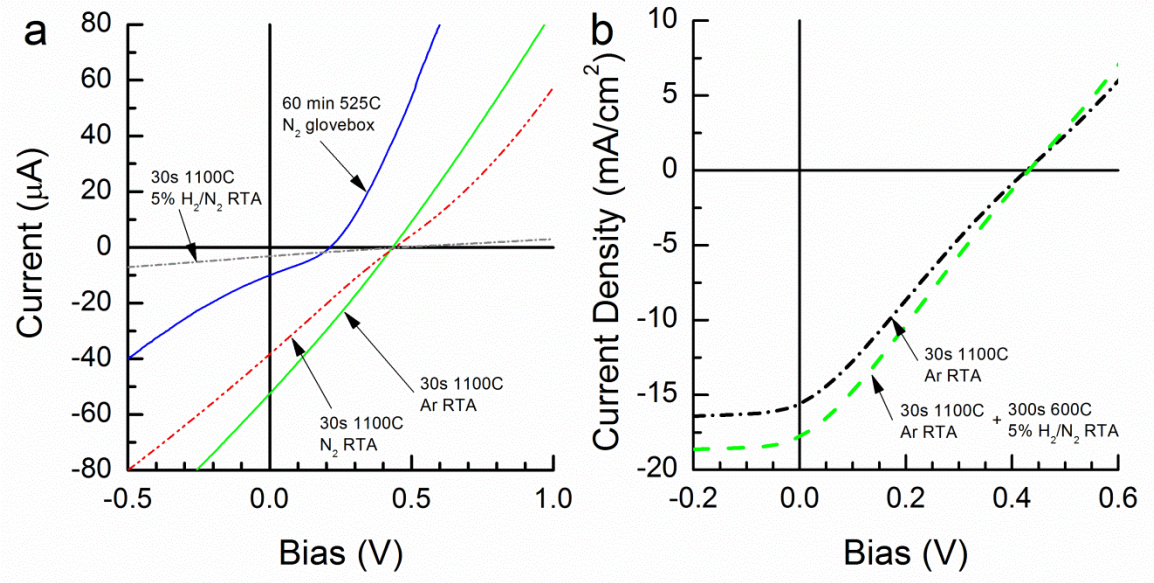

Figure 4.6. SiNC PV cell performance with densification via annealing. (a) I-V characteristics for SiNC PV cells fabricated via annealing with an RTA and ITO top contacts. (b) SiNC PV cell J-V characteristics after optimization using an RTA for 30 s at 1100 °C under Ar, and with additional H exposure using a forming gas post-anneal (5% H_2/N_2).

Table 4.2. Performance parameters for SiNC PV cells in Figure 4.10.

treatment	*name*	V_{oc} *(mV)*	J_{sc} *(mA/cm²)*	*FF (-)*	η_{eff} *(-)*
30 s 1100 °C, Ar RTA	Si94e-1	426	15.6	26.1%	1.74%
30 s 1100 °C, Ar RTA + 300 s 600 °C, 5% H_2/N_2 RTA	Si94f-1	430	17.8	27.1%	2.07%

When trying to increase σ of SiNC films through densification, ALD processes provide an excellent alternative to high temperature annealing. Most ALD processes require modest temperatures (160 - 250 °C) and vacuum pressures (100 Torr - 100 mTorr), and inherently coat surfaces very conformally. Due to the high conformance, infilling of the pores within the SiNC film becomes possible by allowing the ALD precursors to diffuse and penetrate the film. Furthermore, the process can be modified *in situ* to provide a dopant pulse to produce a transparent top contact in addition to the infilling material. Figure 4.7 shows the J-V curves for several SiNC PV cells prepared with different ALD processes, and Table 4.3 reports the corresponding performance parameters. Also included is a cell corresponding to the SiNC film from Figure 4.4(d) coated with AZO only. The annealed film displays much higher performance, but required

significant thermal annealing. Although the performance dropped in cells which were not annealed, the J_{sc} remains comparable to that of the cells reported in Figure 4.7, without the need for thermal annealing. Furthermore, by infilling the SiNC films, the *FF* and V_{oc} improved, indicating a better passivation of the SiNC surface. Overall, the cell response still indicates low σ, however, the infilling process still requires significant optimization.

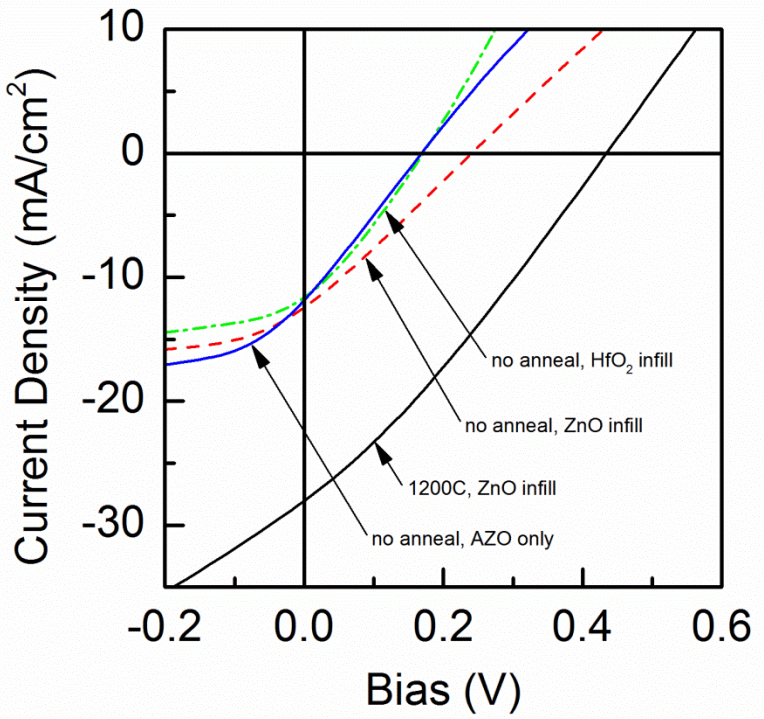

Figure 4.7. SiNC PV cell performance with densification via ALD infilling. J-V curves for SiNC PV cells under different infilling techniques (HfO_2 infill with AZO TC, ZnO infill with AZO TC, and AZO only) and one curve representing the performance of a cell corresponding the film in Figure 4.4(d) (ZnO infill with AZO TC).

Table 4.3. Performance parameters for SiNC PV cells in Figure 4.10.

treatment	*name*	V_{oc} *(mV)*	J_{sc} *(mA/cm²)*	*FF (-)*	η_{eff} *(-)*
no anneal, HfO_2 infill	Si180g-1	168	11.8	29.3%	0.58%
no anneal, ZnO infill	Si177a5-3	240	12.4	26.5%	0.79%
1200 °C, ZnO infill	176c4-3	430	28.0	29.0%	3.50%
no anneal, AZO only	Si177a8-2	160	11.9	27.1%	0.51%

The XS-SEM images in Figure 4.8 illustrates the effect that ALD has on the infilling of the porous SiNC matrix leading to better surface passivation. Figure 4.8(a) shows a cell where the SiNC has not been annealed with a sputtered ITO top contact. The resulting SiNC films appears very porous, and a clear distinction between the SiNC and ITO layers can be made. However, for films which were only coated with ALD AZO and/or ALD infilled with a transparent oxide, the resulting structure resembles something much more dense and compact, likely forming a much better material for carrier transport. Some pores remain after the infilling, indicating longer times for precursor diffusion may be necessary. Careful inspection indicates that the films which were infilled show slightly fewer pores, although not much difference can be made between ZnO and HfO_2 infilling. Figure 4.9 shows the result of attempting ALD infilling with very thick SiNC films. The bright, fluffy material near the substrate indicates the ALD precursors did not diffuse to that depth of the film.

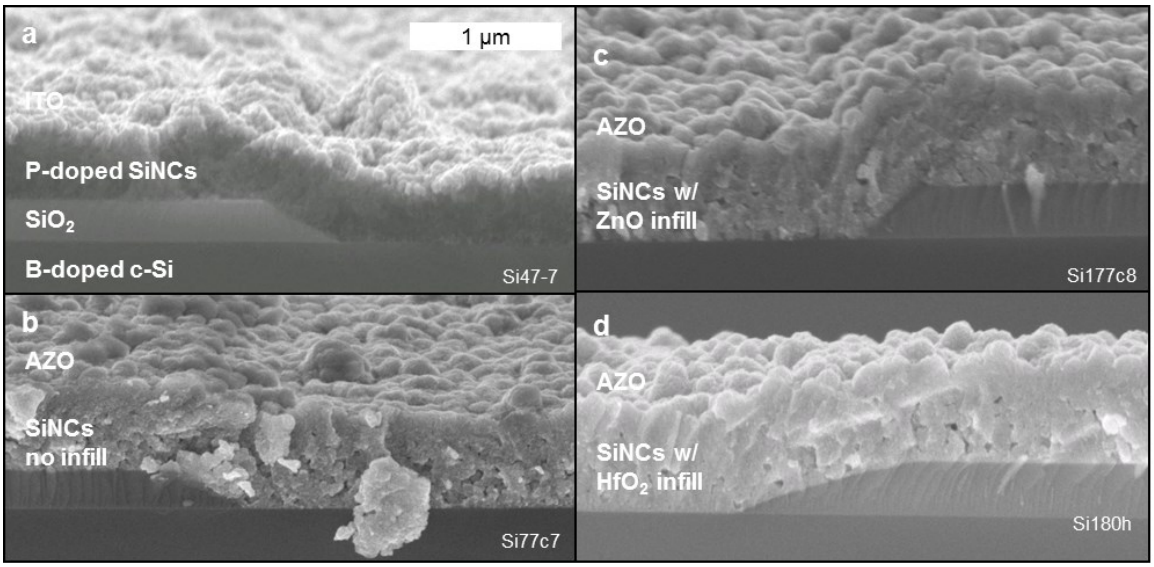

Figure 4.8. Emitter layers for p-n junction PV cells from SiNCs. XS-SEM images of each of the four types of cells depicted in Figure 4.2 at the edge of the active area (a) sputtered ITO top contact, (b) ALD AZO top contact, (c) ALD infill with ZnO followed by ALD AZO, (d) ALD infill with HfO_2 followed by ALD AZO. Scale bar same for all images.

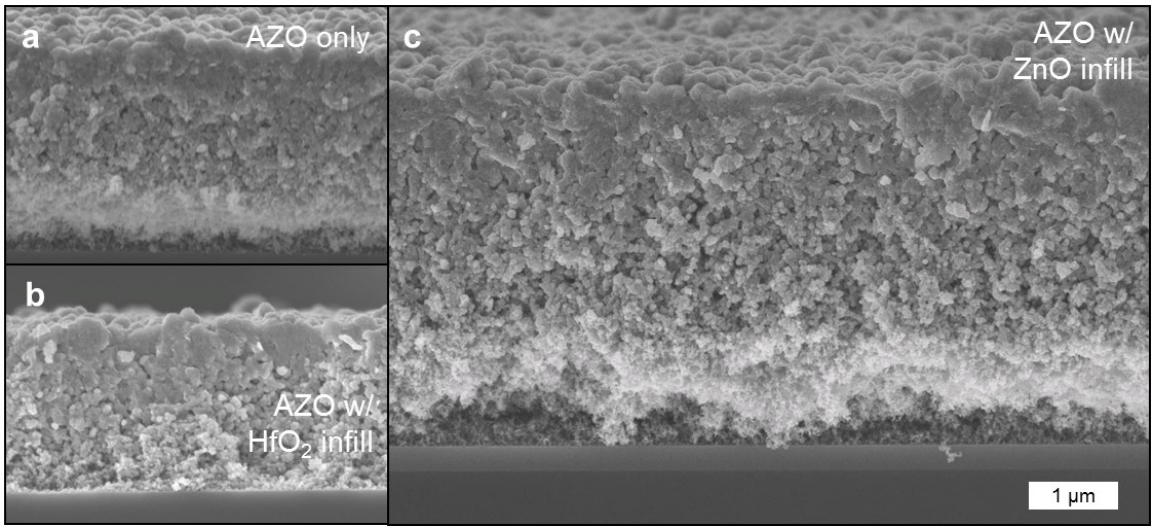

Figure 4.9. Penetration of ALD precursors into thick SiNC films. XS-SEM images for (a) AZO-only deposition, (b) AZO/HfO_2 infill, and (c) AZO/ZnO infill. The porous material near the Si or SiO_2 interface towards the bottom of each image indicates weak penetration for very thick films. Scale bar same for all images.

Figure 4.10 compiles the performance of all the different infilling techniques. Furthermore, the effect of low doping (X_{PH3} = 10%), high doping (X_{PH3} = 50%), and film thickness are included. Moreover, some cells were annealed to high temperature before the ALD process to assess any improvements over the ITO TC structure. Briefly, thin films of heavily doped SiNCs produced the best PV cells. When annealed to 1200 °C, the cells surpassed η_{eff} = 3%, and performed best when infilled with ZnO before the AZO deposition. However, the un-annealed samples hold more potential due their lower thermal budget. In this case, very thin films (requiring only three passes through the SiNC impaction beam) performed the best when infilled with HfO_2 (despite an outlier at 5 passes). Due to the rapid deposition, determining film thicknesses and deposition rates became difficult, however the films in Figure 4.8(b-d) represent 3 passes through the SiNC beam. The HfO_2 infilled cells showed the best *FF* while maintaining high η_{eff} indicating very good SiNC surface passivation, possibly due to a thin SiO_2 layer forming before HfO attachment.

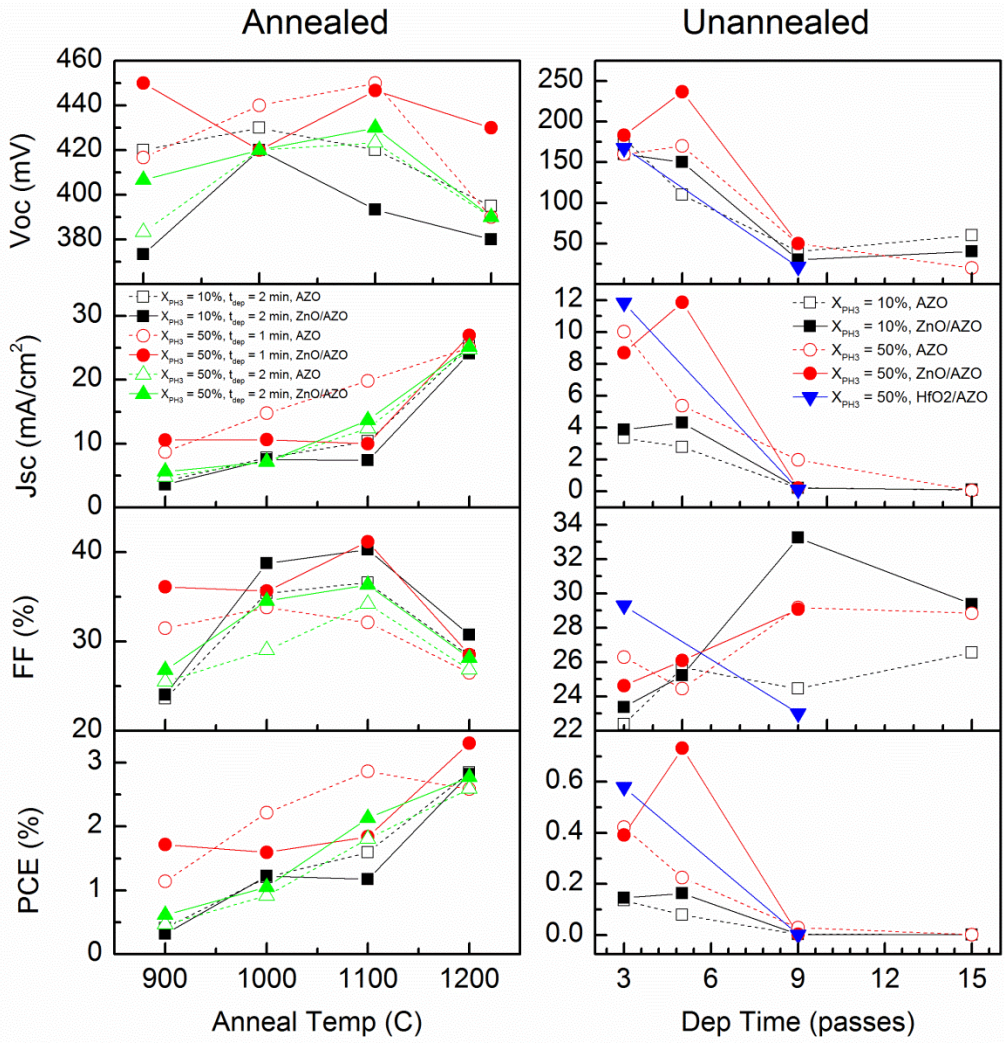

Figure 4.10. Comprehensive SiNC PV cell performance parameters with annealing and ALD infilling and top coating. V_{oc}, J_{sc}, FF, and PCE (η_{eff}) for several SiNC PV cells. X_{PH3} indicates the fractional PH_3 flow rate in the synthesis plasma. Deposition time (Dep Time) measured in minutes for the annealed films, but only integer passes through the particle beam was needed for unannealed films. For reference, 3 passes and 15 passes produce the films shown in Figure 4.8(b-d) and Figure 4.9(c), respectively.

Figure 4.11 shows the different top contact layers in contact with bare SiO_2. All deposition techniques form very smooth uniform films with bare SiO_2, except for some surface roughness when AZO is deposited directly without any infilling material. However, these same processes produce vastly different structures when in contact with the SiNC film. Figure 4.12(a) shows high magnification XS-SEM near the interface between ITO and a SiNC film. The ITO appears to nucleate at the SiNC surface, and grow upwards in well-defined grains, in stark contrast to the film in Figure 4.11(a). In the case of AZO, when it comes in contact with a SiNC surface, it forms

a nano-“rose” structure shown in Figure 4.12(b), unlike the smoother film shown in Figure 4.11(b). This structure has been observed in colloidally-grown ZnO particles,[34] and CVD-grown ZnO.[35] Films infilled with ZnO or HfO_2 before AZO deposition appear to maintain a smooth film with the same approximate surface roughness as the SiNC film. However, optical and electrical transport through these structures and their respective interfaces remains relatively unstudied, and may be significantly impacting device performance.

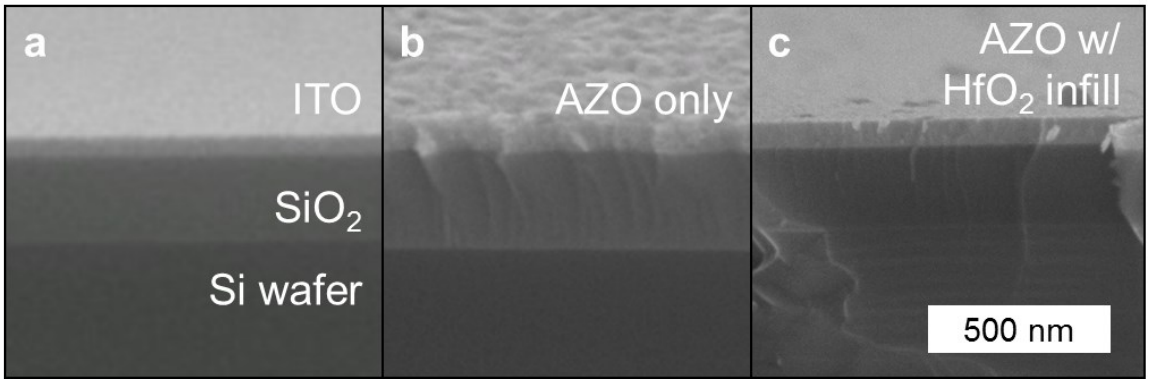

Figure 4.11. Top contact deposition in the absence of SiNCs. XS-SEM images of thin films of top contact material and infill material deposited without SiNCs present. (a) ITO, (b) AZO, (c) AZO over HfO_2 infill. Scale bar same for all images.

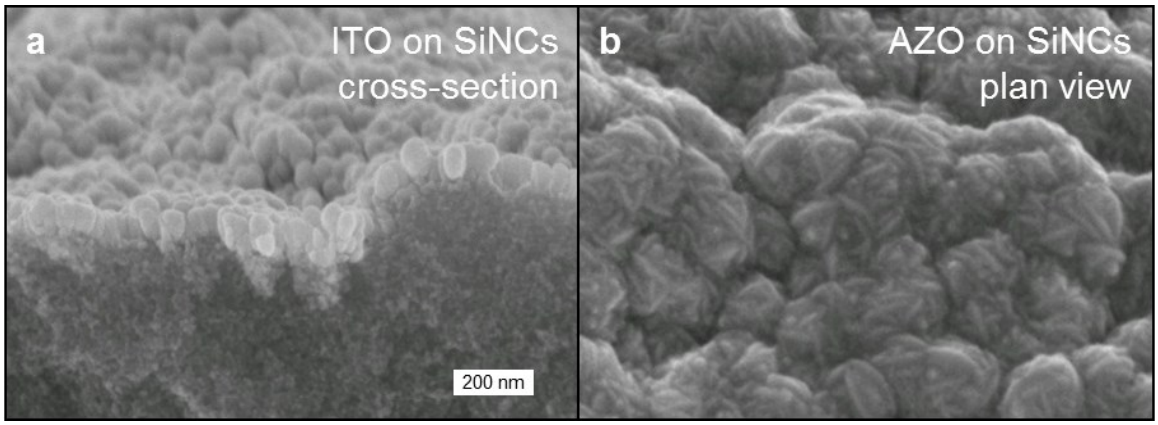

Figure 4.12. Top contact film structure on top of SiNC film. XS-SEM images for films without any infilling. (a) Sputtered ITO in direct contact with SiNCs appears to form small grains which nucleate at the SiNC film surface and grow upwards during the deposition. (b) ALD AZO in direct contact with SiNCs appears to form “nano-roses” when viewed in plan view. Scale bar same for both images.

Lastly, the type of infill changes the device performance during prolonged ambient exposure. Figure 4.13 shows J-V curves for a device with HfO_2 infill and one with ZnO infill, and Table 4.4 compiles the performance parameters for each curve. After 40 days, the ZnO infill cell shows

severe degradation, with every performance parameter decreasing, leading to a ~50% decrease in η_{eff}. On the other hand, after only 17 days of ambient exposure, the HfO_2 infilled cell shows increases in each performance category, leading to a ~50% increase in η_{eff}. To this point, it has been assumed that the ALD process produced stoichiometric HfO_2, however most oxides remain O deficient after deposition. However, Hf oxides have been observed to change chemically[36] and electrically[37] over the course of long periods of ambient exposure. Therefore, a constantly evolving Hf oxide may provide an explanation for the increase in PV cell performance.

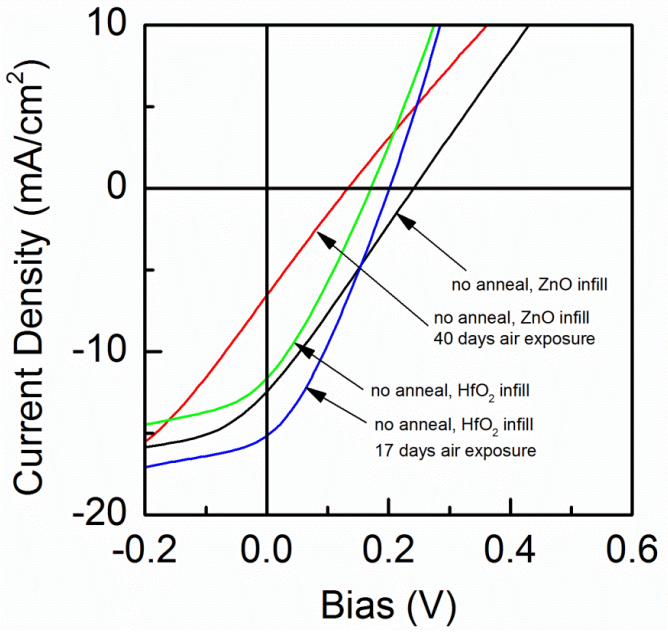

Figure 4.13. SiNC PV cell performance with infilling after several days air exposure. J-V curves for SiNC PV cells measured immediately after fabrication, and after several days of ambient air exposure.

Table 4.4. Performance parameters for SiNC PV cells in Figure 4.12.

treatment	*air exposure (days)*	V_{oc} *(mV)*	J_{sc} *(mA/cm^2)*	*FF (-)*	η_{eff} *(-)*
no anneal, HfO_2 infill	0	183	11.8	26.5%	0.57%
	17	201	15.2	31.5%	0.96%
no anneal, ZnO infill	0	240	12.4	26.5%	0.79%
	40	171	10.5	24.7%	0.44%

Using an ALD infill may provide a new alternative to using SiNCs for PV cells. Within the framework of P-doped SiNCs as emitter layers for a Si wafer based cell, significant areas of

research remain unexplored. The chemical, electrical, and optical properties of the oxides have barely been optimized, with respect to stoichiometry, thickness, and deposition temperature. Furthermore, the robustness offered by ALD allows for the deposition of different oxides (Al_2O_3, SiO_2, etc) possible, as well as other materials such as Si_3N_4 which is a well-known passivating material of Si. Moreover, the amount of infilling and penetration has yet to be fully explored. For testing of this kind, the simple device proposed here continues to make a good testbed, but future iterations could begin to use flexible or inexpensive substrates where separate SiNC layers with custom infill materials form multiple layers of an "all-SiNC" PV cell, or even tandem stacked cells. Due to the rapid deposition and doping capability of SiNC films, such PV cells could be possible in the near future.

4.4. RESULTS & DISCUSSION – ADVANCED PARAMETER EXTRACTION

To further understand the sources of non-ideality in the devices, one can fit the data to a modified ideal diode model. Parasitic resistances alter the shape of the ideal diode curve and lower device performance by providing alternative loss mechanisms. The series resistance, R_s, of a cell usually represents the overall material resistivity and any contact resistance between layers. Optimal PV cells exhibit minimum R_s. Additionally, shunt resistances, R_{sh}, provide alternative pathways for current to flow around the PV junction, and should be maximized to force current to flow through the junction. Carrier recombination in the depletion region can be modeled with a second diode, and non-ohmic resistances can be incorporated with a space-charge limiting component (SCLC) in parallel with R_s. SCLC behavior is observed in simple electrical conductivity measurements of SiNC films at the applied voltage of interest, thereby motivating the addition to the model. To simplify the fitting process further, fitting was only performed for the dark current under forward bias ($V_d > 0$). Using the genetic algorithm implemented through the software Engineering Equation Solver, the fit also included $\ln(I_d)$ vs V_d to accommodate for currents spanning several orders of magnitude. Use of the genetic algorithm and reasonable initial guesses allowed for efficient sampling of the nonlinear solution space to

find a global minimum and several fitting procedures were run to ensure convergence. Equation 4-7 gives the full set of three equations used to account for the model shown in Figure 4.14.

$$
\begin{aligned}
I_d &= I_{d1} + I_{d2} + I_{Rsh} = \sum_{i=1,2} I_{oi}\left[\exp\left(qV_j / m_i k_b T\right) - 1\right] + V_j / R_{sh} \\
I_d &= V_b / R_s + k_{SCLC} V_b^{\,m_{SCLC}} \\
V_d &= V_b + V_j
\end{aligned}
\tag{4-7}
$$

where k_bT = 0.025 eV; I_{d1}, I_{d2}, and I_{Rsh} are the currents through the injection diode, recombination diode, and the shunt resistor, respectively; I_{o1} and I_{o2} are the injection and recombination saturation currents, respectively; $m_{1,2}$ are the ideality factors for the diodes; V_j and V_b are the voltage drops across the junction and bulk, respectively; and k_{SCLC} and m_{SCLC} are the pre-factor and exponent for the SCLC component, respectively. Similar models have been proposed for studying nanocrystalline Si/amorphous Si[38] and P3HT/n-type c-Si solar cells.[39]

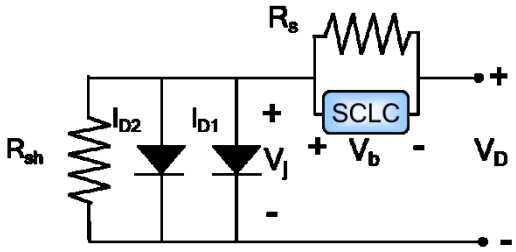

Figure 4.14. Twin diode model equivalent circuit with parasitic resistances and a space charge limited resistor.

Figure 4.15(a) is a log-log plot of I_d vs. V_d, with the light and dark currents plotted linearly in the upper inset. From this plot we extract the solar cell performance parameters: V_{oc} = 419 mV, I_{sc} = 0.82 mA, FF = 33.6%, and η_{eff} = 1.3%. Inspection of the log-log I-V curve indicates that the cell behaves as a non-ideal diode. Under reverse bias and low forward bias (V_d < 0.2 V), the device is limited by R_{sh} indicated by the linear overlapping forward and reverse bias curves. From the dark I-V curve, one can estimate $R_{sh} = dV_d/dI_d$ = 5.7 kΩ for -0.1 V < V_d < 0 V. Similarly, under high forward bias R_s should dominate so one estimates R_s = 250 Ω for 0.9 V < V_d < 1.0 V. The data was fit using three versions of the proposed model; a two-diode model with a SCLC

(2DSC), two-diode without a SCLC (2Dw, k_{SCLC} = 0), and one-diode with a SCLC (1DSC, I_{o2} = 0). A one-diode model without a SCLC (k_{SCLC}, I_{o2} = 0) was also used but the resulting fit was extremely poor and was thereby immediately ruled out as an acceptable model. The fitting parameters extracted from each model are found in Table 4.5. Generally, the two diode model uses m_1 = 1 and m_2 = 2, however, larger values have been reported for different heterojunction SiNC solar cells[21,38,39]. These values are consistent with the values extracted from the following fitting technique. These reports attribute the larger ideality factors to charge trapping in the bulk, which could be significant in a SiNC film, with a relatively large defect density as compared to bulk Si. Theoretical considerations predict m_{SCLC} = 2 for space charge limiting current in the absence of traps, however, values for m_{SCLC} have been reported between 2 - 4 depending on the presence of trap states in the semiconductor[39,40]. From this procedure, one can extract values for m_{SCLC} ~ 4.3 for both the 1DSC and 2DSC model. One obtains close fits with much larger values for m_1, m_2, and m_{SCLC}, however the underlying physics of the model is undetermined and m_1, m_2, and m_{SCLC} only apply as empirical fitting parameters, such as in the case of the ideality factor for the recombination diode (m_2 = 5.4) in the 2Dw model. Only under the 2DSC model do the fitting parameters lie in a physically meaningful range. Figure 4.15(b) shows a plot of the experimental data and the corresponding fits, as well as deviation plot for each model. Empirically, all models fit the data quite well however the 2DSC model has equal or lower deviation in all regions of forward bias compared to the other models. It is interesting to note that the 2DS model fits with very low deviation near the V_{oc} region, even though the fit was done under dark current conditions. Extracted values of R_s and R_{sh} from the fitting agree closely with values estimated from the dark I-V curve slope, regardless of the model used to fit the data. Unfortunately, the 2DSC model contains the most terms of all the models, which should naturally make the fit closer to the experimental data. Therefore, the actual accuracy of the model should be taken under further consideration. Extraction of some of the parameters with other methods would further validate this model, but has not been attempted thus far.

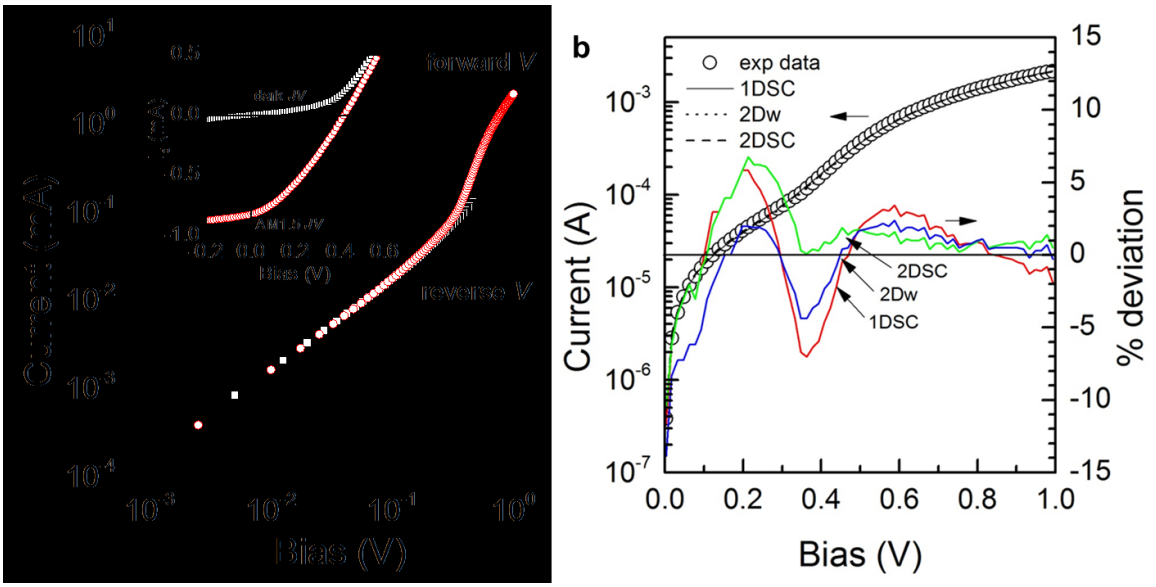

Figure 4.15. I-V characteristics and fitting results for typical ITO top contact PV cell. (a) Log-log dark current of SiNC/c-Si heterojunction solar cell. (Inset) Light and dark current plotted linearly of same device. (b) Experimental data (open circles) and fitted data (lines) of equivalent circuits one- or two- diode (1D or 2D) and with or without space charge limited component (SC or w). Deviation of current to fit plotted on the right axis.

Table 4.5. Extracted solar cell parameters from Figure 4.15(b)

Parameter	*1DSC*	*2Dw*	*2DSC*
I_{o1} *(A)*	2.6×10^{-7}	2.8×10^{-8}	1.6×10^{-9}
m_1 *(-)*	2.34	1.79	1.38
I_{o2} *(A)*	--	2.8×10^{-6}	7.0×10^{-7}
m_2 *(-)*	--	5.44	3.18
k_{SCLC} *(A V^m)*	6.8×10^{-5}	--	3.2×10^{-5}
m_{SCLC} *(-)*	4.30	--	4.41
R_s *(Ω)*	204	220	232
R_{sh} *(Ω)*	5821	6274	5970
*std dev (A)**	0.0337	0.0301	0.0295

Nevertheless, the extracted parameters at least partially indicate that significant charge trapping is present in this device. This is likely due to two factors: (a) surface states and dangling bond defects acting as trap states, or (b) interface states between the ITO and SiNC film where a Si oxide may have formed. Partial oxidation of the SiNCs can occur during synthesis due to etching of the plasma reactor tube, and such low temperature oxidation can increase the dangling bond defect density of the SiNCs, contributing to charge trapping.[41] Further oxidation and contamination are inherent to the ITO sputtering environment due the O present in the sputtering plasma to achieve more stoichiometric and conductive ITO. This leads to the presence of highly

reactive O radicals which can rapidly form SiO_2 near the surface of the SiNCs. Charge trapping may occur at the oxide/crystalline interface, or within the oxide itself. As mentioned earlier, perhaps ALD processes will provide better interfacial regions to SiNC films for reduced charge carrier trapping and increased σ.

4.5. REFERENCES

(1) Nozik, A. J. *Physica E* **2002**, *14*, 115–120.
(2) Conibeer, G.; Green, M.; Cho, E.-C.; König, D.; Cho, Y.-H.; Fangsuwannarak, T.; Scardera, G.; Pink, E.; Huang, Y.; Puzzer, T.; Huang, S.; Song, D.; Flynn, C.; Park, S.; Hao, X.; Mansfield, D. *Thin Solid Films* **2008**, *516*, 6748–6756.
(3) Nozik, A. J. *Nano letters* **2010**, *10*, 2735–41.
(4) Sark, W. van; Meijerink, A. In *Third Generation Photovoltaics*; 2011; pp. 1–28.
(5) Wilcoxon, J. P.; Samara, G. A.; Provencio, P. N. *Physical Review B* **1999**, *60*, 2704.
(6) Van Buuren, T.; Dinh, L. N.; Chase, L. L.; Siekhaus, W. J.; Terminello, L. J. *Physical Review Letters* **1998**, *80*, 3803–3806.
(7) Von Behren, J.; Van Buuren, T.; Zacharias, M.; Chimowitz, E. H. H.; Fauchet, P. M. M. *Solid State Communications* **1998**, *105*, 317–322.
(8) Meier, C.; Gondorf, A.; Luttjohann, S.; Lorke, A.; Wiggers, H. *Journal of Applied Physics* **2007**, *101*, 103112–8.
(9) Beard, M. C.; Midgett, A. G.; Hanna, M. C.; Luther, J. M.; Hughes, B. K.; Nozik, A. J. *Nano letters* **2010**, *10*, 3019–27.
(10) Luque, A.; Marti, A.; Nozik, A. J. *MRS Bulletin* **2007**, *32*, 236–241.
(11) Nozik, A. J. *Nature Nanotechnology* **2009**, *4*, 548–549.
(12) Semonin, O. E.; Luther, J. M.; Choi, S.; Chen, H.-Y.; Gao, J.; Nozik, A. J.; Beard, M. C. *Science (New York, N.Y.)* **2011**, *334*, 1530–3.
(13) Allan, G.; Delerue, C. *Physical Review B* **2008**, *77*, 1–10.
(14) Shpaisman, H.; Niitsoo, O.; Lubomirsky, I.; Cahen, D. *Solar Energy Materials and Solar Cells* **2008**, *92*, 1541–1546.
(15) Beard, M.; Knutsen, K.; Yu, P.; Luther, J.; Song, Q.; WK *Nano Lett* **2007**, *4*, 4–10.
(16) Luque, A.; Hegedus, S. *Handbook of photovoltaic science and engineering*; John Wiley & Sons Inc: Hoboken, NJ, 2003.
(17) Ghosh, A. K. A.; Fishman, C.; Feng, T. *Journal of Applied Physics* **1980**, *51*, 446–454.
(18) Yang, J.; Banerjee, A.; Guha, S. *Solar Energy Materials and Solar Cells* **2003**, *78*, 597–612.
(19) Liu, C.-Y.; Holman, Z. C.; Kortshagen, U. R. *Nano Letters* **2009**, *9*, 449–452.
(20) Švrček, V.; Slaoui, A.; Muller, J. C. *Thin Solid Films* **2004**, *451-452*, 384–388.
(21) Perez-Wurfl, I. H.; Hao, X.; Gentle, A.; Kim, D.; Conibeer, G.; Green, M. A. *Applied Physics Letters* **2009**, *95*, 153506.
(22) Park, S.; Cho, E.; Song, D.; Conibeer, G.; Green, M. A. *Solar Energy Materials and Solar Cells* **2009**, *93*, 684–690.

(23) Kim, S.-K.; Cho, C.-H.; Kim, B.-H.; Park, S.-J.; Won Lee, J. *Applied Physics Letters* **2009**, *95*, 143120.
(24) Zhao, J.; Wang, A.; Green, M. A.; Ferrazza, F. *Applied Physics Letters* **1998**, *73*, 1991–1993.
(25) Schultz, O.; Glunz, S. W.; Willeke, G. P. *Progress in Photovoltaics: Research and Applications* **2004**, *12*, 553–558.
(26) Sze, S. M. *Physics of semiconductor devices*; New York, Wiley-Interscience: New York, 2005.
(27) Nelson, J. *The physics of solar cells*; London : Imperial College Press: London, 2003; p. 363.
(28) Goldstein, A. N.; Echer, C. M.; Alivisatos, A. P. *Science* **1992**, *256*, 1425–7.
(29) Goldstein, A. N. *Applied Physics A: Materials Science & Processing* **1996**, *62*, 33–37.
(30) Nanda, K. K. *European Journal of Physics* **1998**, *19*, 471–472.
(31) Schierning, G.; Theissmann, R.; Wiggers, H.; D; Sudfeld, D.; Ebbers, A.; Franke, D.; Witusiewicz, V. T.; Apel, M. *Journal of Applied* **2008**, *103*, 1–6.
(32) Holm, J.; Roberts, J. T. *Journal of Physical Chemistry C* **2009**, *113*, 15955–15963.
(33) Winters, B. J.; Holm, J.; Roberts, J. T. *Journal of Nanoparticle Research* **2011**, *13*, 5473–5484.
(34) Bai, W.; Yu, K.; Zhang, Q.; Zhu, X.; Peng, D.; Zhu, Z.; Dai, N.; Sun, Y. *Physica E: Low-dimensional Systems and Nanostructures* **2008**, *40*, 822–827.
(35) Zhang, N.; Yi, R.; Shi, R.; Gao, G.; Chen, G.; Liu, X. *Materials Letters* **2009**, *63*, 496–499.
(36) Morant, C.; Galán, L.; Sanz, J. M. *Surface and Interface Analysis* **1990**, *16*, 304–308.
(37) Satake, T.; Yamamoto, M.; Natio, S.; Mabuchi, M.; Kaneda, A.; Kurahashi, M.; Hashino, T. *Journal of the Chemical Society, Faraday Transactions* **1993**, *89*, 3611.
(38) Pallarès, J.; Cabré, R.; Marsal, L. F.; Schropp, R. E. I. *Journal of Applied Physics* **2006**, *100*, 084513.
(39) Nolasco, J. C.; Cabré, R.; Ferré-Borrull, J.; Marsal, L. F.; Estrada, M.; Pallarès, J. *Journal of Applied Physics* **2010**, *107*, 044505.
(40) Rose, A. *Physical Review* **1955**, *97*, 1538–1544.
(41) Pereira, R. N.; Rowe, D. J.; Anthony, R. J.; Kortshagen, U. *Physical Review B* **2011**, *83*, 155327.

5. OXIDATION & DEFECTS – TWO TYPES OF SINC INHERENT IMPURITIES[§]

5.1. INTRODUCTION

Strictly speaking, a perfectly pure SiNC would consist of only Si atoms and nothing else. Realistically, this is certainly not the case. Depending on the synthesis technique, SiNCs are usually covered in a variety of elements and/or molecules, and in some cases are specifically engineered as such. These surface atoms, or states, can be considered as inherent impurities, a necessary chemical termination to the SiNC surface. Even if every non-Si atom is removed from the SiNC surface, the unsatisfied chemical bonds which remain either restructure to create a low energy surface, or form a different class of inherent impurities commonly known as dangling bond defects. Defects such as these can be located on the NC surface or within the crystalline core, causing disruption of the crystalline structure. However, the surface defects are typically reactive, and prefer to fulfill their chemical bonds.

Of all the possible inherent chemical reactions which can occur at the SiNC surface, oxidation represents a ubiquitous mechanism of inherent impurity incorporation which maintains great fundamental and technological importance. For instance, the oxidation of Si surfaces forms the basis for metal-oxide-semiconductor (MOS) capacitors and field-effect transistors, key components in the microelectronics industry.[1] Additionally, it is generally understood that surface oxides are responsible for water solubility and biocompatibility, which have become essential properties for SiNCs since these are increasingly regarded as promising biomaterials.[2–4] In previous investigations of SiNCs fabricated by other techniques, it has been found that oxidation and oxide defect states play important roles in SiNC photoemission.[5,6] Theoretical calculations

[§] Parts of this chapter are reproduced with permission from R.N. Pereira, D.J. Rowe, R.J. Anthony, and U. Kortshagen, Physical Review B (10.1103/PhysRevB.83.155327, 2011) and (10.1103/PhysRevB.86.085449, 2012). Copyright 2011, 2012 American Physical Society.

indicate that this could originate from the introduction of intragap energy levels by interfacial Si=O bonds[7] and Si–O–Si surface bridges.[8]

Oxidation of H-terminated SiNCs can readily take place in air at room temperature,[9–13] whereas under pure molecular O atmosphere higher temperatures are required.[14] Oxidation at high temperatures is limited by O diffusion through the oxide layer, a model proposed by Deal and Grove in 1965.[15] However, at room temperature the diffusion coefficient is much too low to explain oxidation. Instead, Cabrera and Mott proposed an oxidation model, in which an electron from the Si tunnels through the oxide and is captured by largely electronegative oxidant molecules, like O_2 or H_2O. This process is shown schematically in Figure 5.1 as starting with step [1] through step [5]. [1] An H- or OH- terminated surface is introduced to oxidants such as water or molecular O. [2] Dipolar water molecules induce a charge dipole in a Si-Si bond. [3] Then, a charge from the induced dipole tunnels through the oxide layer and attaches to an oxidant such as O_2 or H_2O. [4] An image charge is created in the Si due to the newly charged surface species, and the resulting dipole creates an electric field that forces the oxidant to drift through the growing oxide layer towards the Si/SiO_2 interface. [5] Eventually the O_2 molecule inserts itself within the Si-Si bond. As the oxide layer grows, the tunneling probability of an electron through the layer decreases exponentially and eventually limits the reaction.

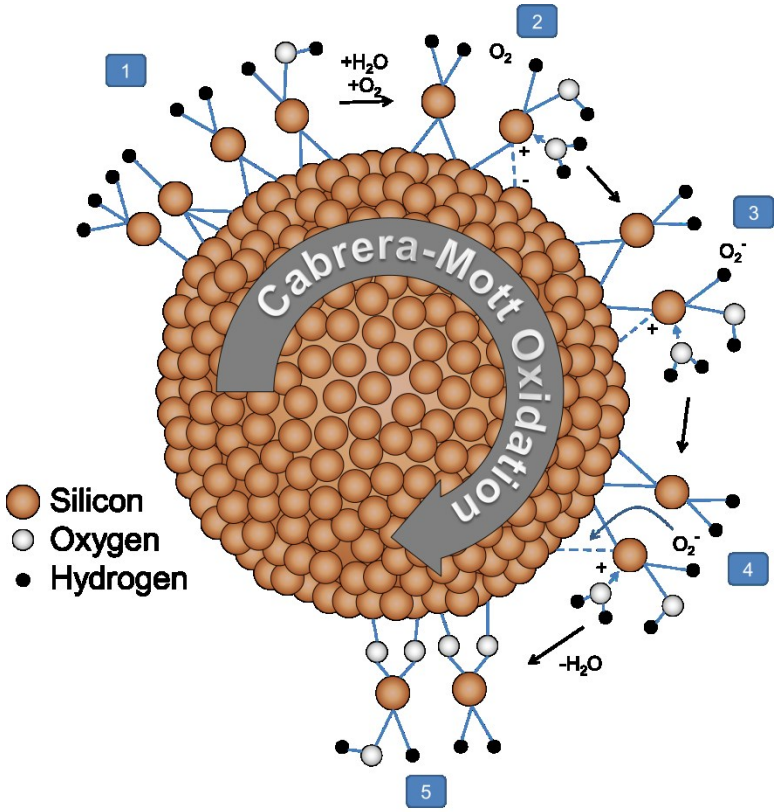

Figure 5.1. Diagram of the Cabrera-Mott mechanism for Si oxidation as applied to SiNCs.

Although the SiNC core can be virtually defect free, coordination point defects are expected to form at the interface between the NC core and an oxide shell. Two types of interfacial paramagnetic defects have recently been detected with electron spin resonance (ESR) in gas-phase-grown NCs containing an oxide shell.[16] One was assigned to a structure similar to that of the so-called P_b centers in bulk-Si/SiO_2 interfaces, i.e., an Si sp3 dangling bond (SiDB) on an interfacial Si atom, backbonded to three Si atoms of the Si crystal ($Si_3{\equiv}Si\bullet$).[17,18] The other defect was ascribed to a SiDB located in a disordered environment.[16] Similar defects have been previously observed in porous Si samples oxidized in ambient air.[19] Combined magnetic resonance and electrical studies demonstrated that these defects have an adverse impact as recombination and charge-trapping centers on the electrical conductivity of SiNC ensembles[20,21] and on the efficiency of electronic doping with foreign atoms.[16] Importantly, degradation of light emission from confined excitons in SiNCs has been observed, which was attributed to an

oxidation-induced generation of DBs.[9,22] Earlier theoretical studies indicated that these defects are efficient photoluminescence quenchers.[23] On the other hand, luminescence enhancement has been observed after oxidation of SiNCs produced by other methods, which has been attributed to an oxidation-induced passivation of DBs.[24–28] Distinct initial surface passivation and oxidation conditions may explain the apparent discrepancy between different studies. In an investigation where the oxidation approach of reducing the NCs size has been explored, the light emission of the smaller NCs obtained has been associated with defects,[22] in line with findings for SiNCs embedded in amorphous SiO_2[6,29] and porous Si.[30] Thus, a consensus has been reached that interfacial defects and, in particular, SiDBs strongly influence the (opto) electronic properties of SiNC ensembles. If we are aware of the detailed dynamics and mechanisms of the creation and elimination of these defects during oxidation of SiNCs, we will be in a position to minimize their negative impact. Moreover, given the fact that these defects reside essentially at the interface between the SiNC core and the growing oxide shell, they are extremely sensitive interface probes and therefore provide invaluable insight into interface phenomena involved in oxidation of Si surfaces.

Despite their recognized worth, very few reports exist regarding the association of defects with oxidation. In principle, one could rely on information obtained for H-terminated bulk-Si surfaces to infer the behavior of interfacial defects on plasma-synthesized, H-terminated SiNCs.[31–37] However, studies monitoring the evolution of DB interfacial defects upon oxidation of H-terminated bulk-Si surfaces have not been reported since the time scale of surface reactions in the early oxidation stages is shorter than the time required to acquire enough ESR scans to detect interfacial DB centers due to the relatively low density of these defects. As far as theoretical modeling is concerned, existing studies indicate that the P_b centers in bulk-Si/SiO2 interfaces are a product of the emission of interfacial Si atoms to release strain generated due to the formation of Si−O−Si bonds.[36,38] To date, experimental evidence directly linking the creation of P_b defects with the formation of Si−O−Si bridges has been elusive.

Previous studies have revealed that Si dangling bonds (SiDBs) have an adverse impact on the SiNC properties.[9,16,20,22] SiDBs act as recombination and trapping centers for electrons and holes moving across SiNC superlattices,[20,21] strongly decreasing the efficiency of electronic doping with foreign impurities,[16] and have been associated with degradation of light emission from confined excitons.[9,22] Improvement of the performance of SiNCs in (photo) electronic applications and accomplishment of new applications require the fabrication of SiNCs with very low defect content by means of inexpensive and scalable methods. SiNCs grown from microwave plasma-assisted decomposition of SiH_4 display typically an order of magnitude increase in the interfacial DB density [$(5–7)\times10^{11}$ cm^{-2}] after surface oxidation in air is completed, corresponding to 0.25–0.35 defects per NC for SiNCs of 4 nm size.[16,21] Subsequently, the defect density was reduced by up to one order of magnitude after the SiNCs were subjected to wet etching in hydrofluoric acid followed by vacuum heating at 200 °C.[21,39] Recently, highly efficient photoluminescence was observed after alkene functionalization of SiNCs grown with injection of additional H_2 gas into the afterglow region of a nonthermal RF plasma.[40] This enhanced photoluminescence was correlated with the presence of surface Si-H_3 species and a lower amount of defects, as suggested from a reduced ESR intensity from SiDBs observed for these SiNCs in comparison to SiNCs grown with He or Ar added in the afterglow region instead of H_2. However, the exact nature of the role the defects plays in oxidation and PL is not yet completely understood. In this chapter, samples produced with a low initial defect density (LIDD) and a moderate initial defect density (MIDD) will be studied in order to elucidate dependencies of SiDBs on the SiNC oxidation process. A correlation between initial surface termination, oxidation rate, and SiDB density will be discussed in terms of time-dependent ESR and FTIR measurements.

5.2. EXPERIMENTAL METHODS

5.2.1. SYNTHESIS OF UNDOPED SINCS

SiNCs were synthesized with the reactor described in Chapter 1, under two different conditions to yield SiNCs with high photoluminescent quantum yield,[40] and NCs with completely quenched photoluminescence,[41] after previous experiments correlated high PLQY to low defect density. To fabricate samples with high photoluminescent quantum yield, additional H_2 gas was injected into the afterglow of the plasma, which had been shown to saturate the surface with H, thereby reducing dangling bond defects, and preparing the surface favorably for hydrosilylation.[40] From now on, these samples are denoted as LIDD. Although the absence of H_2 injection in the plasma afterglow has been shown to *decrease* photoluminescence significantly after hydrosilylation,[40] it is not possible to *eliminate* photoluminescence entirely simply by omitting H_2 injection. Therefore, several other plasma conditions are varied to produce SiNCs with completely quenched PL so an obvious comparison could be made, and are now referred to as MIDD. The term “moderate” is in reference to a smaller defect density than observed for SiNCs fabricated with a microwave plasma.[16,21] The conditions and reactor geometries used to produce each sample can be found in Table 5.1 and Figure 5.2, respectively. SiNCs were collected either via a mesh filter downstream of the plasma, or via inertial impaction. Control experiments showed that the collection scheme does not significantly affect the NC surface. Samples were kept air free under a dry N_2 environment before initial measurements were performed. After a control measurement under no or minimal air exposure, samples were exposed to ambient room conditions and allowed to oxidize for 5000 hours.

Table 5.1. Standard synthesis conditions for undoped SiNCs before oxidation

LIDD SiNCs	*Condition*	*MIDD SiNCs*
5% SiH_4 in He (13 sccm)	***Precursor gas***	100% SiH_4 (6 sccm)
Ar (35 sccm)	***Carrier gas***	Ar (200 sccm)
1.4 Torr	***Pressure***	3.6 Torr
H_2 (100 sccm)	***Injection gas***	None
5.5 mm	***Internal tube diameter***	22 mm
4.0 nm	***SiNC diameter***	5.5 nm
yes	***Observable PL***	no

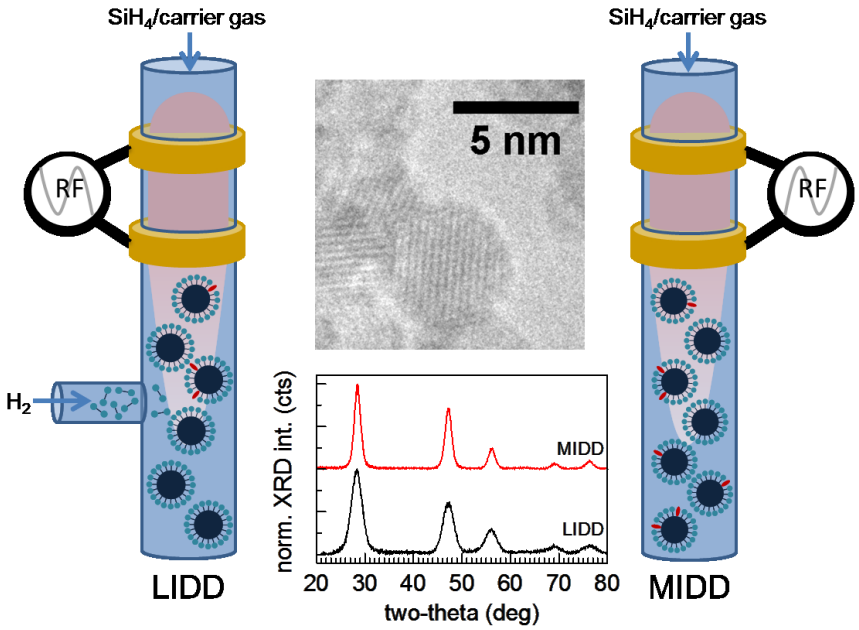

Figure 5.2. Reactor schematics for generating SiNC with low initial defect density (LIDD) and mid initial defect density (MIDD). Upper inset: TEM image of MIDD SiNC. Lower inset : x-ray diffraction data used for estimating the SiNC diameter from the Scherrer equation.

5.2.2. FTIR SPECTROSCOPY

FTIR measurements were carried out with a N_2-purged Nicolet Series II Magna-IR System 750 spectrometer, equipped with a glowbar light source, a KBr beam splitter, and a mercury-cadmium-telluride detector. All absorbance spectra were recorded in diffuse reflection mode at room temperature with a resolution of 2 cm^{-1} and averaged over 100 scans. A bare gold-coated Si wafer was used as a reference. The samples were continuously exposed to air between

consecutive measurements. For FTIR measurements, SiNCs were deposited from the plasma via inertial impaction onto gold-coated Si substrates. To avoid oxidation before the first measurement, as-grown SiNCs were transferred under vacuum condition from the synthesis to the FTIR spectrometer.

5.2.3. XRD

The crystalline diffraction pattern was measured using a Bruker-AXS microdiffractometer with a 2.2-kW sealed Cu x-ray source and a Hi-Star 2-D Area Detector. Powder samples were lightly pressed onto a piece of glass substrate for mounting in the instrument, and diffraction patterns were recorded at ambient room conditions. One frame centered at $2\theta = 36°$ and $\omega = 18°$ was collected for 5-10 minutes, so as to provide a pattern with good signal to noise ratio. The mean NC diameter was estimated from the reflection broadening using the Scherrer equation.

5.2.4. ESR

ESR measurements were performed at room temperature in continuous-wave Bruker spectrometers mounted with X-band microwave bridges. The spin-density measurements were calibrated using a diphenylpicrylhydrazyl (DPPH) reference, magnetic field values were measured using a nuclear magnetic resonance Teslameter (resolution better than 5×10^{-3} mT), and the microwave frequency was measured with a frequency counter with resolution above 10^{-5} GHz. Samples were made by filling a small, ESR inactive, suprasil glass capillary tube with a known mass of NCs under dry N_2. Both ends of the tube were packed with Teflon tape and sealed with epoxy to prevent the unwanted oxidation of the samples. To initiate oxidation, one end of the tube was cleaved and the Teflon packing was removed. ESR measurements were performed in cooperation with Rui Pereira from the Department of Physics and Institute for Nanostructures, Nanomodelling, and Nanofabrication at the University of Aveiro, Portugal.

5.3. RESULTS AND DISCUSSION

Figure 5.3(a) compares the ESR spectra of LIDD and MIDD SiNCs recorded within 3 min after air exposure. The spectra show a structured band in the region of g ~ 2, which can be well reproduced by a sum of an axially symmetric powder pattern of Lorentzian lines (dashed curves), whose linewidths increase linearly from the direction parallel to the symmetry axis to the perpendicular direction, and a relatively less intense line with Gaussian shape (dotted curves). The two spectral components originate from axially symmetric and isotropic defects with electron spin S = 1/2. The contribution of axial defects is dominant since they always represent more than 85% of the total number of defects. The values of $g_{\perp}$ = 2.0086 and $g_{||}$ = 2.0019 observed after complete oxidation of the NCs (t_{ox} > 130 days) are very close to those reported for the Si3≡Si• defects in bulk-Si/SiO_2 interfaces (P_b centers).[17] Thus, we assign the axial component of our spectra to a Si_3≡Si• defect in the interface between the NCs core and the growing oxide shell, denoted hereafter P^{NC}_b to distinguish from the P_b centers in bulk-Si/SiO_2 interfaces. The g value observed after complete oxidation for the isotropic spectral component is g_D = 2.0053. This value is very close to those typically found for the SiDBs in a disordered environment, which have been observed in bulk-Si/SiO_2 interfaces,[42] and in amorphous Si.[43] Therefore, we assign this spectral component to the same type of defect in our SiNCs. Fig. 5.3(b) shows the ESR spectrum of LIDD and MIDD SiNCs recorded after complete oxidation. After complete oxidation, the spectrum of LIDD SiNCs is quite similar qualitatively to that observed for MIDD SiNCs, though the initial spectra were significantly different. After complete oxidation the P^{NC}_b and D defects represent about 85% and 15%, respectively, of the total amount of defects for both the LIDD and MIDD SiNCs. Before oxidation the P^{NC}_b and D defects represent about 94% and 6%, respectively, of the total amount of defects in the MIDD SiNCs. The situation is inverted for the LIDD SiNCs, where the initial ESR band is dominated by the contribution of D defects. The total defect density of 7×10^9 cm^{-2} recorded before oxidation is also close to the density of D defects [D] = 4×10^9 cm^{-2} measured after complete oxidation, which indicates that the increase of the total defect density to

the value of 2×10^{10} cm^{-2} is mainly due to the increase of P^{NC}_b defect density induced by oxidation.

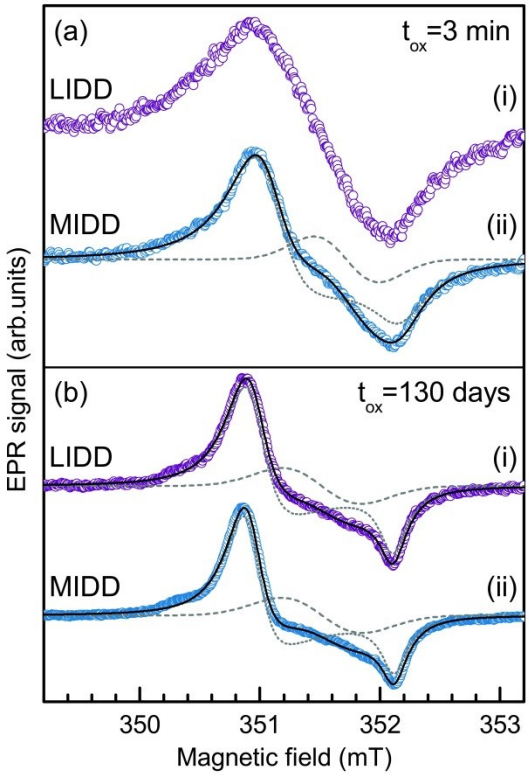

Figure 5.3. SiNC dangling bonds before and after oxidation. Normalized first-derivative ESR spectra for (i) LIDD and (ii) MIDD SiNCs upon (a) initial exposure to air and (b) 130 days of ambient oxidation. Solid line indicates total defect density fit, dashed line indicates isotropic D-defect component, and dotted indicates axial P_b-defect component.

Figure 5.4 shows sections of the FTIR spectra of SiNCs recorded for different t_{ox}. In the first collected spectrum (within 2 min of air exposure), the spectral region of Si−H modes is dominated by a structured band at 2000–2150 cm^{-1} due to Si_{4-x}−Si−H_x (x = 1, 2, 3) surface hydride stretching modes,[44,45] and a doublet observed near 900 cm^{-1} associated with deformation modes of Si-Si-H_3 and with scissor and wag modes of Si-Si-H_2.[44,46] In the lower energy range a band centered at 1045 cm^{-1} is observed, originating from Si−O−Si bridges.[45] The appearance of a small Si−O−Si band, as well as the observation of P_b-type defects as shown in Figure 5.3(a), in the as-grown SiNCs is most likely due to a small O contamination of NCs during synthesis. A significant decrease of the hydride band is observed in the spectrum recorded for large t_{ox}, while

the intensity of the band in the 1000–1250 cm^{-1} spectral region due to Si−O−Si bonds displays a strong increase. These changes are accompanied by the emergence of a line at 2202 cm^{-1} due to Si−H stretching in intermediate oxidation states O_2−Si−H_2 and O_2Si−Si−H and a line at 2255 cm^{-1} from O_3−Si−H surface bonds.[13,45,47,48] The LIDD SiNCs exhibit a pronounced higher-order hydride (Si-Si-H_3) concentration due to the additional H_2 injected into the afterglow of the synthesis plasma. The MIDD SiNCs were not treated with H_2 injection and the hydride stretching region is similar to that observed by Winters and co-workers,[11] when their SiNCs synthesized in a nonthermal plasma were heated to 400 °C in flight. This indicates that the particle temperature for the MIDD SiNCs remained sufficiently high immediately after synthesis in the plasma afterglow for some H desorption to occur. In the spectra recorded for the LIDD SiNCs after a long-time exposure to air (dashed lines), the intensity of the band related to Si-O-Si stretching increases strongly with a shape different from that for MIDD SiNCs. For LIDD SiNCs, the Si-O-Si bridging band shifts from 1030 - 1045 cm^{-1} and grows slightly during oxidation. As the SiNCs oxidize, the Si-O-Si band starts to exhibit a higher-frequency shoulder around 1145 cm^{-1}, while the main peak continues to shift to approximately 1070 cm^{-1}.

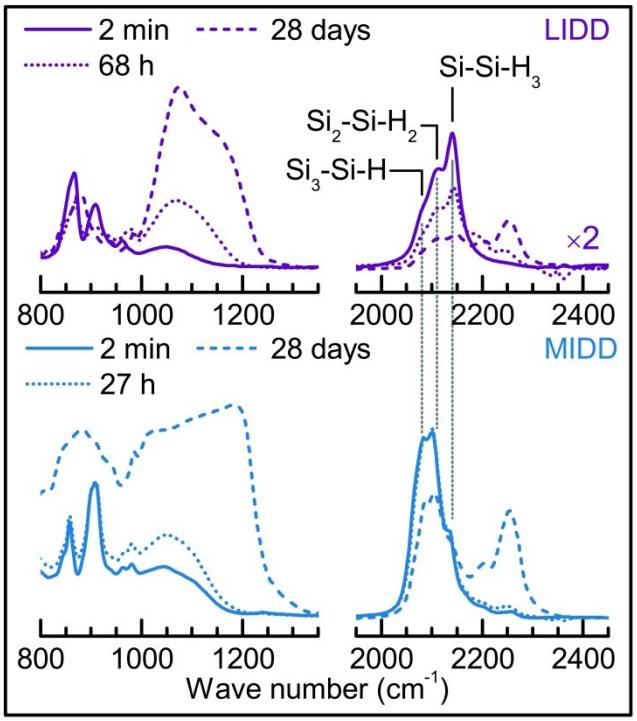

Figure 5.4. FTIR of oxidizing SiNCs. FTIR absorbance spectra for LIDD and MIDD SiNCs for times corresponding to initial exposure to air, the end of the induction period, and complete oxidation.

The ESR spectra obtained for the complete range of oxidation times investigated, spanning from a few minutes to several months, were fitted with the two-component spectrum, from which the SiDB densities and ESR spectral parameters were extracted via double numerical integration. The obtained dependence of the SiDB density as a function of t_{ox} is depicted in Figure 5.5(a). An initial defect density of 7×10^{9} cm^{-2} is observed for LIDD SiNCs, which remains approximately constant over the first 100 h (4.2 days) of air exposure. This density corresponds to only about 0.002–0.005 defects per SiNC, or one SiDB per 200–400 SiNCs. An increase of the defect density is observed only for t_{ox} > 100 h, followed by saturation at about 2×10^{10} cm^{-2} at $t_{ox} \approx 800$ h (33 days). For the case of MIDD SiNCs, a defect density decrease to a minimum value of 3×10^{10} cm^{-2} was observed in the first ~30 h (1.25 days) of air exposure, after which an increase is observed, followed by a saturation at about 5×10^{10} cm^{-2} also at $t_{ox} \approx 800$ h (33 days).

The evolution of the intensity of bands from Si-O-Si and Si_{4-x}-Si-H_x, estimated by numerical integration of the FTIR spectra in the 995–1350 and 1885–2170 cm^{-1} intervals, respectively, with

t_{ox} is shown in Figure 5.5(b,c). After an initial period of time, referred to as the induction period,[31–33,49] characterized by nearly no oxidation of the SiNC surface, the oxidation accelerates in a logarithmic fashion until it reaches saturation at $t_{ox} \sim 800$ h. We have fitted the dependence of the Si-O-Si band intensity on t_{ox} with the Elovich equation, [50] defined as:

$$n_m(t_{ox}) = \lambda_m t_m \ln\left(1 + t_{ox}/t_m\right) \quad (5\text{-}1)$$

where t_{ox} is oxidation time, n_m is the amount of reaction products, and λ_m and t_m are reaction rate and characteristic time, respectively. The fitting curves obtained for the LIDD and MIDD samples are shown as solid lines in Figures 5.5(b) and 5.5(c), respectively. From the fittings, we estimate a characteristic time t_m of 88 h (3.7 days) for LIDD SiNCs and 33 h (1.4 days) for MIDD SiNCs. These are indicated as dashed vertical lines in Figure 5.5. As can be seen, the t_m values obtained agree very well with the onset of SiDB formation observed for the respective SiNCs, providing further support to the conclusion that the creation of interfacial SiDB defects is directly linked to the formation of surface Si-O-Si bonds. First-principles studies of bulk-Si surfaces have predicted that strong local stress arises around Si−O−Si bridges formed during oxidation.[51] To release the stress, Si atoms participating in newly formed Si−O−Si bonds are emitted, leaving behind a bridge-bond oxygen (BBO) and unsatisfied orbitals at nearest-neighboring Si atoms. These dangling orbitals may form bonds between them[51] or remain unsaturated as P_b centers.[36,38] A slow-fast-slow evolution of Si−O−Si formation with $\log(t_{ox})$ has also been reported for ambient-air oxidation of bulk-Si surfaces terminated with H, with the initial period of slow oxidation, referred to as the induction period, ranging from 3 to 170 h (7 days), depending on the Si surface index, air humidity, and the initial amount of residual Si−OH groups at the surface.[31–33,37,49] It has been shown for bulk-Si surfaces that the duration of the induction period is shorter for higher air humidity and higher density of residual Si−OH groups.[33,37]

The difference in t_m should not result from the differences in size of the NCs in the two samples. In previous studies, shorter induction periods have been observed for nanoparticles

(curved Si surface) in comparison to flat surfaces of bulk Si,[52] due to the increasingly higher number of oxidation sites present in increasingly curved surfaces. Thus, the somewhat smaller size of the NCs in the LIDD samples would result in a shortened induction period in comparison to MIDD SiNCs, which is in clear contrast with our experimental results. Therefore, the longer induction period observed for the LIDD SiNCs should have another origin. For ambient-air oxidation of bulk Si surfaces, values ranging from 3 to 170 h have been found, depending on the Si surface index, air humidity, and the initial amount of residual Si-OH groups at the surface. According to the Cabrera-Mott mechanism of ambient-air oxidation of bulk Si and SiNC surfaces,[10,35,53] the oxidation is initiated by adsorption of water molecules at surface Si-OH groups followed by cleavage of Si-Si backbonds of Si-OH. This is followed by electron transfer from the broken bond to an adsorbed O_2 molecule, which drifts toward the cleaved bond, leading to the oxidation of this bond and of a neighboring Si-Si bond.[35] The steps prior to the formation of Si-O-Si take place during the induction period and a larger amount of surface Si-OH groups results in a shorter t_m.[33,37] Thus, the large difference in t_m observed for LIDD and MIDD SiNCs should originate from a smaller surface coverage of the LIDD SiNCs with Si-OH groups. This is also supported by our FTIR data, where we observe the presence of surface Si-OH bonds only for the MIDD SiNCs. The differences observed in the initial behavior of the defect density immediately after air exposure between LIDD and MIDD SiNCs may also elucidate this issue. As mentioned above, in the case of MIDD SiNCs an initial decrease of the defect density is observed, which could be due to the reaction $Si_3{\equiv}Si\bullet+H_2O\rightarrow Si_3{\equiv}Si\text{-}OH+H$, resulting in a coverage of the NC surface with Si-OH groups. This defect density reduction upon air exposure is not observed for LIDD, which could indicate a smaller surface contamination in this case.

The combined ESR and FTIR data enable us to draw the following important conclusions. In the case of LIDD SiNCs, the majority of surface SiDBs present at the newly formed SiNC surface are passivated by H_2 gas injected into the plasma afterglow, resulting in a very low initial defect density (0.002–0.005 defects per NC). Remarkably, this value is about 30 times lower than that observed for H-terminated SiNCs grown from microwave plasma-assisted decomposition of

SiH_4.[21,39] The dangling bonds which are present in the as-produced SiNCs are in fact most likely located on sites inaccessible to H, i.e., are not located close to the SiNC surface. This is also consistent with the fact that the ESR signal reveals mostly D-defects, as shown in Figure 5.3(a), which are typically SiDBs located on internal sites. Such in-flight passivation of surface SiDBs does not take place in MIDD SiNCs, resulting in the considerably larger density of defects observed (4×10^{10} cm^{-2}) and a markedly different shape of the ESR spectra, due to the presence of surface defects of type P^{NC}_b in addition to the residual internal D-defects [Fig. 5.3(a)]. For MIDD SiNCs, the decrease of the intensity of the ESR spectrum during the induction period shows that the amount of P^{NC}_b (superficial) defects decreases. This decrease has been associated with (i) an effective passivation of the defects, via, e.g., the reaction $Si_3{\equiv}Si\bullet+H_2O\rightarrow Si_3{\equiv}Si\text{-}OH+H$, or (ii) a charge transfer process that changes the valence state of the P^{NC}_b defects to a charged (diamagnetic) state. The relatively low SiDB density for LIDD SiNCs may be understood based on the mechanism (i). For LIDD SiNCs, the amount of superficial P^{NC}_b defects is negligible and the residual SiDBs present (D-defects) are not accessible to H_2O. Therefore, the reaction $Si_3{\equiv}Si\bullet+H_2O\rightarrow Si_3{\equiv}Si\text{-}OH+H$ does not take place, resulting in a quite stable density of SiDBs throughout the entire induction period.

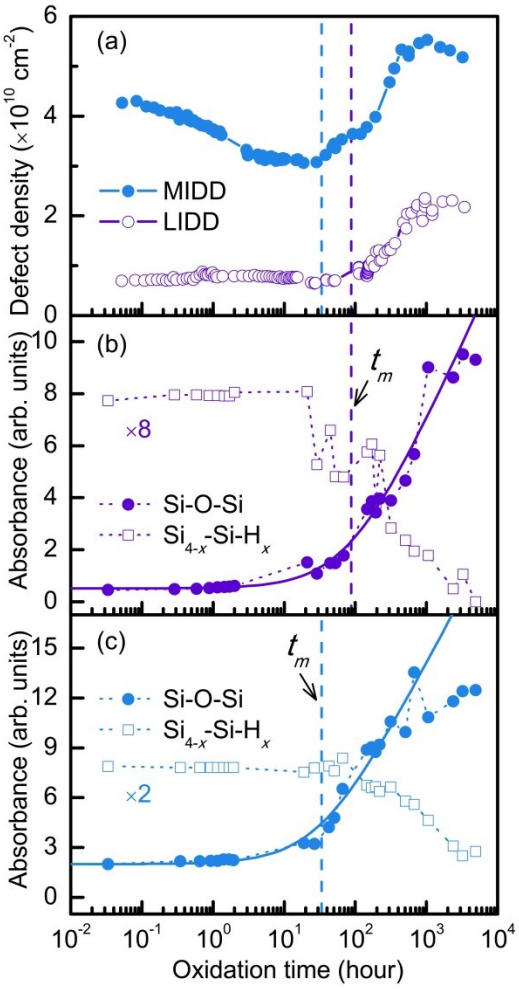

Figure 5.5. Temporal evolution for LIDD and MIDD SiNCs. (a) total defect density and (b-c) integrated FTIR absorbance for characteristic bands for Si-O-Si bridging bonds and surface H stretching bonds. Dashed vertical lines represent induction time, tm, for each sample.

The ESR data can also elucidate the differences in the time evolution of the Si-O-Si band as measured in FTIR spectroscopy. In the LIDD sample, the low-frequency peak shifts to higher energy and increases in intensity, consistent with increasing stoichiometry of the surface Si oxide. For the MIDD sample, a growth and shift of the main peak similar to those observed for the LIDD SiNCs is observed during the induction period. However, after the induction period the higher-frequency shoulder gradually overtakes the peak initially at 1026 cm^{-1}. Similar behavior is observed in the literature and is attributed to two mechanisms: (1) for changes in stoichiometry the main O peak shifts towards higher wave numbers, saturating at ~ 1078.5 cm^{-1} for the stoichiometric SiO_2,[54] and (2) for thin films of SiO_2 a similar shift and shoulder appearance is

attributed to localized compressive stress and SiO_2 restructuring.[55] It is reasonable to conclude that a complete oxide monolayer does not form until the end of the induction period and the onset of defect creation. Then, as the oxide layer grows, additional O incorporation causes compressive stress to form in the surface layer, which is consistent with the appearance of the high-frequency shoulder in the Si-O-Si band. For the MIDD SiNCs, more initial defects lead to more sites available for O incorporation and a larger amount of disorder in the oxide layer. This causes a much larger compressive stress to form, even though the defect creation rate remains the same as that of the LIDD sample, consistent with the much larger and dominant high-frequency shoulder in the Si-O-Si band of the MIDD sample.

5.4. REFERENCES

(1) Sze, S. M. *Physics of semiconductor devices*; New York, Wiley-Interscience: New York, 2005.

(2) Erogbogbo, F.; Tien, C.-A.; Erogbogbo, F.; Chang, C.-W.; Adjei-Baffour, P.; Law, W.-C.; Swihart, M. *Nature Precedings* **2012**, 1–16.

(3) O'Farrell, N.; Houlton, A.; Horrocks, B. R. *International Journal of Nanomedicine* **2006**, *1*, 451–72.

(4) Erogbogbo, F.; Yong, K.-T.; Roy, I.; Xu, G.; Prasad, P. N.; Swihart, M. T. *ACS nano* **2008**, *2*, 873–8.

(5) Biteen, J. S.; Lewis, N. S.; Atwater, H. A.; Polman, A. *Applied Physics Letters* **2004**, *84*, 5389.

(6) Godefroo, S.; Hayne, M.; Jivanescu, M.; Stesmans, A.; Zacharias, M.; Lebedev, O. I.; Van Tendeloo, G.; Moshchalkov, V. V *Nature nanotechnology* **2008**, *3*, 174–8.

(7) Luppi, M.; Ossicini, S. *Physical Review B* **2005**, *71*, 1–15.

(8) Vasiliev, I.; Chelikowsky, J.; Martin, R. *Physical Review B* **2002**, *65*, 2–5.

(9) Pi, X. D.; Mangolini, L.; Campbell, S. A.; Kortshagen, U. R. *Physical Review B (Condensed Matter and Materials Physics)* **2007**, *75*, 85421–85423.

(10) Liptak, R. W.; Kortshagen, U. R.; Campbell, S. A. *Journal of Applied Physics* **2009**, *106*, 064313.

(11) Winters, B. J.; Holm, J.; Roberts, J. T. *Journal of Nanoparticle Research* **2011**, *13*, 5473–5484.

(12) Ogata, Y.; Tsuboi, T.; Sakka, T.; Naito, S. *Journal of Porous Materials* **2000**, *7*, 63–66.

(13) Kato, Y.; Ito, T.; Hiraki, A. *Applied Surface Science* **1989**, *41/42*, 614–618.

(14) Holm, J.; Roberts, J. T. *Langmuir* **2007**, *23*, 11217–24.

(15) Deal, B. E.; Grove, A. S. *Journal of Applied Physics* **1965**, *36*, 3770.

(16) Stegner, A. R.; Pereira, R. N.; Lechner, R.; Klein, K.; Wiggers, H.; Stutzmann, M.; Brandt, M. S. *Physical Review B (Condensed Matter and Materials Physics)* **2009**, *80*, 165326 (10 pp.).

(17) Stesmans, A.; Nouwen, B.; Afanas'ev, V. *Physical Review B* **1998**, *58*, 15801–15809.
(18) Pierreux, D.; Stesmans, A. *Physical Review B* **2002**, *66*, 1–9.
(19) Schoisswohl, M.; Cantin, J. L.; Von Bardeleben, H. J.; Amato, G. *Applied Physics Letters* **1995**, *66*, 3660.
(20) Stegner, A. R.; Pereira, R. N.; Klein, K.; Lechner, R.; Dietmueller, R.; Brandt, M. S.; Stutzmann, M.; Wiggers, H. *Physical Review Letters* **2008**, *100*, 026803.
(21) Niesar, S.; Stegner, A. R.; Pereira, R. N.; Hoeb, M.; Wiggers, H.; Brandt, M. S.; Stutzmann, M. *Applied Physics Letters* **2010**, *96*, 193112.
(22) Gupta, A.; Swihart, M. M. T.; Wiggers, H. *Advanced functional materials* **2009**, *19*, 696–703.
(23) Delerue, C.; Allan, G.; Lannoo, M. *Physical Review B* **1993**, *48*, 11024–11036.
(24) Ledoux, G.; Guillois, O.; Porterat, D.; Reynaud, C.; Huisken, F.; Kohn, B.; Paillard, V. *Physical Review B* **2000**, *62*, 15942–15951.
(25) Švrček, V.; Sasaki, T.; Shimizu, Y.; Koshizaki, N. *Applied Physics Letters* **2006**, *89*, 213113.
(26) Dohnalová, K.; Kůsová, K.; Pelant, I. *Applied Physics Letters* **2009**, *94*, 211903.
(27) Ledoux, G.; Gong, J.; Huisken, F. *Applied Physics Letters* **2001**, *79*, 4028.
(28) Dinh, L.; Chase, L.; Balooch, M.; Siekhaus, W.; Wooten, F. *Physical Review B* **1996**, *54*, 5029–5037.
(29) Prokes, S.; Carlos, W.; Veprek, S.; Ossadnik, C. *Physical Review B* **1998**, *58*, 15632–15635.
(30) Prokes, S. M.; Carlos, W. E. *Journal of Applied Physics* **1995**, *78*, 2671.
(31) Houston, M. R.; Maboudian, R. *Journal of Applied Physics* **1995**, *78*, 3801.
(32) Gräf, D.; Grundner, M.; Schulz, R.; Mühlhoff, L. *Journal of Applied Physics* **1990**, *68*, 5155.
(33) Miura, T.; Niwano, M.; Shoji, D.; Miyamoto, N. *Journal of Applied Physics* **1996**, *79*, 4373.
(34) Cerofolini, G. F.; Meda, L. *Journal of Non-Crystalline Solids* **1997**, *216*, 140–147.
(35) Cerofolini, G. F.; Mascolo, D.; Vlad, M. O. *Journal of Applied Physics* **2006**, *100*, 054308.
(36) Yamasaki, T.; Kato, K.; Uda, T. *Physical Review Letters* **2003**, *91*, 3–6.
(37) Niwano, M.; Kageyama, J.; Kurita, K.; Kinashi, K.; Takahashi, I.; Miyamoto, N. *Journal of Applied Physics* **1994**, *76*, 2157.
(38) Kato, K.; Yamasaki, T.; Uda, T. *Physical Review B* **2006**, *73*, 9–12.
(39) Niesar, S.; Pereira, R. N.; Stegner, A. R.; Erhard, N.; Hoeb, M.; Baumer, A.; Wiggers, H.; Brandt, M. S.; Stutzmann, M. *Advanced Functional Materials* **2012**, *22*, 1190–1198.
(40) Anthony, R. J.; Rowe, D. J.; Stein, M.; Yang, J.; Kortshagen, U. *Advanced Functional Materials* **2011**, *21*, 4042–4046.
(41) Unpublished Research **2010**.
(42) Wimbauer, T.; Ito, K.; Mochizuki, Y.; Horikawa, M.; Kitano, T.; Brandt, M. S.; Stutzmann, M. *Applied Physics Letters* **2000**, *76*, 2280.
(43) Brodsky, M.; Title, R. *Physical Review Letters* **1969**, *23*, 581–585.
(44) Marra, D. C.; Edelberg, E. A.; Naone, R. L.; Aydil, E. S. *Journal of Vacuum Science & Technology A: Vacuum, Surfaces, and Films* **1998**, *16*, 3199.
(45) W Theiss *Surface Science Reports* **1997**, *29*, 91–192.
(46) Holm, J.; Roberts, J. T. *Journal of the American Chemical Society* **2007**, *129*, 2496–2503.

(47) Lucovsky, G.; Yang, J.; Chao, S.; Tyler, J.; Czubatyj, W. *Physical Review B* **1983**, *28*, 3234–3240.
(48) O'Keeffe, P.; Aoyagi, Y.; Komuro, S.; Kato, T.; Morikawa, T. *Applied Physics Letters* **1995**, *66*, 836.
(49) Bodlaki, D. *Journal of Applied Physics* **2004**, *95*, 4675.
(50) Aharoni, C.; Tompkins, F. C. *Advances in Catalysis* **1970**, *21*, 1–49.
(51) Kageshima, H.; Shiraishi, K. *Physical Review Letters* **1998**, *81*, 5936–5939.
(52) Yang, D.-Q.; Gillet, J.-N.; Meunier, M.; Sacher, E. *Journal of Applied Physics* **2005**, *97*, 024303.
(53) Pi, X. D.; Gresback, R.; Liptak, R. W.; Campbell, S. A.; Kortshagen, U. R. *Applied Physics Letters* **2008**, *92*, 2008–2010.
(54) Fitch, J.; Kim, S.; Lucovsky, G. *Journal of Vacuum Science & Technology A: Vacuum, Surfaces, and Films* **1990**, *8*, 1871–1877.
(55) San Andrés, E.; Del Prado, A.; Martínez, F. L.; Mártil, I.; Bravo, D.; López, F. J. *Journal of Applied Physics* **2000**, *87*, 1187.

6. CONCLUDING REMARKS

The thesis highlighted the motivation to understand semiconductor NC impurities, the challenges involved in studying such material systems, and the technology employed to do so. Chapter 1 provided a general summary of SiNC synthesis techniques while identifying the advantages for using a capacitively-coupled, low pressure, RF nonthermal plasma for SiNC synthesis. Chapters 2-4 focused on the *intentional* addition of impurities, and Chapter 5 discussed inherent impurities in the form of dangling bond defects and oxidation.

Chapter 2 concentrated on the synthesis and characterization of highly P-doped SiNCs exhibiting LSPR in the mid-IR (400 – 2500 cm^{-1}). This was the first demonstration of SiNCs displaying LSPR despite silicon's importance in a variety of applications. The chapter explained that extremely high concentrations of PH_3 within the synthesis plasma are required for sufficient electrically active dopant incorporation within the SiNC, upwards of X_{PH3} ~ 50%. These results agree with previous reports indicating the difficulty associated with NC doping due to dopant segregation to the NC surface. It was found that only about 10% of the dopant delivered to the plasma resides in the NC core, and a fraction of that became electrically active. Interfacial scattering, particle-particle interactions, dielectric medium interactions, and trapped free carriers were identified to explain the reduced experimental LSPR frequency compared to theoretical predicted frequencies.

Chapter 3 explained the synthesis of doped SiGeNC alloys for thermoelectric applications. It was shown that NCs could be truly alloyed such that only a single phase is identified using XRD, and that by invoking Vegard's law, the composition of the SiGeNC matches nicely with the flow ratio of the semiconductor precursors in the plasma. Furthermore, P- and B-doping incorporation was measured using EDX, with doping incorporation efficiency of P and B from the plasma precursors to the NC of 29% and 16%, respectively. A NC impaction process was used for thin film deposition and was shown to produce very uniform and reproducible films for subsequent

post-processing and thermoelectric property measurement. The impaction process may also be used to produced layered films of any phase material and has been proposed as a convenient method for fabricating advanced nanostructured thermoelectric devices.

Chapter 4 described research using P-doped SiNCs to form emitter layers for pn-junction type solar cells with a c-Si wafer base. Important aspects of this research include; NC film post processing, e.g. annealing, etching, infilling; photovoltaic device fabrication; and optical characterization. High temperature annealing processes sintered or melted the NC films producing solar cells with large J_{sc} but fairly low η (2-4%) due to poor fill factors and low V_{oc}. NC films infilled with a dielectric by means of ALD showed η ~1% without the need for any high temperature annealing. The ALD infill process worked best with an HfO_2 infill followed by an AZO top coat which also acted as the transparent top contact of a pn-junction cell. Lastly, a two-diode pn-junction model with parasitic resistances including a space charge limited component was proposed to explain the large non-idealities and I-V characteristics of these cells.

Chapter 5 examined dangling bond defect evolution during oxidation of SiNCs using EPR and FTIR. The oxidation rates of SiNCs was found to be extremely dependent on the initial Si-DB density, with large Si-DB densities leading to more rapid oxidation. The Si-DB density could be correlated to the type of H surface coverage of the SiNCs, with the appearance of more Si-Si-H_3 surface bonds linked to lower Si-DB density. The addition of Si-Si-H_3 species was accomplished by injecting H_2 into the plasma afterglow. It was shown that by using H_2 injection, SiNCs could be produced with extremely low Si-DB densities, ~ 1 EPR-active Si-DB per 100 SiNCs.

7. COMPREHENSIVE BIBLIOGRAPHY

2010 Solar Technologies Market Report; 2011.

Aharoni, C.; Tompkins, F. C. *Advances in Catalysis* **1970**, *21*, 1–49.

Allan, G.; Delerue, C. *Physical Review B* **2008**, *77*, 1–10.

Anthony, R. J.; Cheng, K.-Y.; Holman, Z. C.; Holmes, R. J.; Kortshagen, U. R. *Nano letters* **2012**, *12*, 2822–5.

Anthony, R. J.; Rowe, D. J.; Stein, M.; Yang, J.; Kortshagen, U. *Advanced Functional Materials* **2011**, *21*, 4042–4046.

Anthony, R.; Kortshagen, U. *Physical Review B* **2009**, *80*, 1–6.

Anthony, R.; Thimsen, E.; Johnson, J.; Campbell, S.; Kortshagen, U. *Mater. Res. Soc. Symp. Proc.* **2006**, *892*, 5–8.

Bai, W.; Yu, K.; Zhang, Q.; Zhu, X.; Peng, D.; Zhu, Z.; Dai, N.; Sun, Y. *Physica E: Low-dimensional Systems and Nanostructures* **2008**, *40*, 822–827.

Baldwin, R. K.; Pettigrew, K. A.; Ratai, E.; Augustine, M. P.; Kauzlarich, S. M. *Chemical communications* **2002**, 1822–3.

Bapat, A.; Perrey, C. R.; Campbell, S. A.; Barry Carter, C.; Kortshagen, U. *Journal of Applied Physics* **2003**, *94*, 1969.

Batson, P.; Heath, J. *Physical Review Letters* **1993**, *71*, 911–914.

Beard, M. C.; Knutsen, K. P.; Yu, P.; Luther, J. M.; Song, Q.; Metzger, W. K.; Ellingson, R. J.; Nozik, A. J. *Nano Letters* **2007**, *7*, 2506–2512.

Beard, M. C.; Midgett, A. G.; Hanna, M. C.; Luther, J. M.; Hughes, B. K.; Nozik, A. J. *Nano letters* **2010**, *10*, 3019–27.

Beard, M.; Knutsen, K.; Yu, P.; Luther, J.; Song, Q.; WK *Nano Lett* **2007**, *4*, 4–10.

Behr, M. J.; Mkhoyan, K. A.; Aydil, E. S. *ACS nano* **2010**, *4*, 5087–94.

Bell, L. E. *Science* **2008**, *321*, 1457–61.

Bermejo, D.; Cardona, M. *Journal of Non-Crystalline Solids* **1979**, *32*, 421–430.

Biteen, J. S.; Lewis, N. S.; Atwater, H. A.; Polman, A. *Applied Physics Letters* **2004**, *84*, 5389.

Bodlaki, D. *Journal of Applied Physics* **2004**, *95*, 4675.

Borgarello, E.; Kiwi, J.; Graetzel, M.; Pelizzetti, E.; Visca, M. *Journal of the American Chemical Society* **1982**, *104*, 2996–3002.

Brodsky, M.; Title, R. *Physical Review Letters* **1969**, *23*, 581–585.

Buonsanti, R.; Llordes, A.; Aloni, S.; Helms, B. A; Milliron, D. J. *Nano Letters* **2011**, *11*, 4706–10.

Bux, S. K.; Blair, R. G.; Gogna, P. K.; Lee, H.; Chen, G.; Dresselhaus, M. S.; Kaner, R. B.; Fleurial, J.-P. *Advanced Functional Materials* **2009**, *19*, 2445–2452.

Canham, L. T. *Applied Physics Letters* **1990**, *57*, 1046.

Cerofolini, G. F.; Mascolo, D.; Vlad, M. O. *Journal of Applied Physics* **2006**, *100*, 054308.

Cerofolini, G. F.; Meda, L. *Journal of Non-Crystalline Solids* **1997**, *216*, 140–147.

Chen, H.-T.; Padilla, W. J.; Zide, J. M. O.; Gossard, A. C.; Taylor, A. J.; Averitt, R. D. *Nature* **2006**, *444*, 597–600.

Cheng, K.-Y.; Anthony, R.; Kortshagen, U. R.; Holmes, R. J. *Nano letters* **2011**, *11*, 1952–6.

Chino, H. U.; Kamoto, Y. O.; Awahara, T. K.; Orimoto, J. M. *Applied Physics* **2000**, *39*, 1675–1677.

Choi, W. K.; Teh, L. K.; Bera, L. K.; Chim, W. K.; Wee, A. T. S.; Jie, Y. X. *Journal of Applied Physics* **2002**, *91*, 444.

Chrastina, D.; Cecchi, S.; Hague, J. P.; Frigerio, J.; Samarelli, A.; Ferre–Llin, L.; Paul, D. J.; Müller, E.; Etzelstorfer, T.; Stangl, J.; Isella, G. *Thin Solid Films* **2013**.

Conibeer, G.; Green, M.; Cho, E.-C.; König, D.; Cho, Y.-H.; Fangsuwannarak, T.; Scardera, G.; Pink, E.; Huang, Y.; Puzzer, T.; Huang, S.; Song, D.; Flynn, C.; Park, S.; Hao, X.; Mansfield, D. *Thin Solid Films* **2008**, *516*, 6748–6756.

Dalpian, G.; Chelikowsky, J. *Physical Review Letters* **2006**, *96*, 1–4.

Darma, Y.; Takaoka, R.; Murakami, H.; Miyazaki, S. *Nanotechnology* **2003**, *14*, 413–415.

Deal, B. E.; Grove, A. S. *Journal of Applied Physics* **1965**, *36*, 3770.

Delerue, C.; Allan, G.; Lannoo, M. *Physical Review B* **1993**, *48*, 11024–11036.

Di, D.; Perez-Wurfl, I.; Conibeer, G.; Green, M. A. *Solar Energy Materials and Solar Cells* **2010**, *94*, 2238–2243.

Dinh, L.; Chase, L.; Balooch, M.; Siekhaus, W.; Wooten, F. *Physical Review B* **1996**, *54*, 5029–5037.

DiSalvo, F. J. *Science* **1999**, *285*, 703–706.

Dismukes, J. P.; Ekstrom, L.; Steigmeier, E. F.; Kudman, I.; Beers, D. S. *Journal of Applied Physics* **1964**, *35*, 2899.

Dohnalová, K.; Kůsová, K.; Pelant, I. *Applied Physics Letters* **2009**, *94*, 211903.

Dresselhaus, M. S.; Chen, G.; Tang, M. Y.; Yang, R. G.; Lee, H.; Wang, D. Z.; Ren, Z. F.; Fleurial, J.-P.; Gogna, P. *Advanced Materials* **2007**, *19*, 1043–1053.

Erogbogbo, F.; Liu, T.; Ramadurai, N.; Tuccarione, P.; Lai, L.; Swihart, M. T.; Prasad, P. N. *ACS nano* **2011**, *5*, 7950–9.

Erogbogbo, F.; Tien, C.-A.; Erogbogbo, F.; Chang, C.-W.; Adjei-Baffour, P.; Law, W.-C.; Swihart, M. *Nature Precedings* **2012**, 1–16.

Erogbogbo, F.; Yong, K.-T.; Roy, I.; Xu, G.; Prasad, P. N.; Swihart, M. T. *ACS nano* **2008**, *2*, 873–8.

Erwin, S.; Zu, L.; Haftel, M. I.; Efros, A. L.; Kennedy, T. A.; Norris, D. J. *Nature* **2005**, *436*, 91–4.

Fage-Pedersen, J.; Larsen, A.; Mesli, A. *Physical Review B* **2000**, *62*, 10116–10125.

Fitch, J.; Kim, S.; Lucovsky, G. *Journal of Vacuum Science & Technology A: Vacuum, Surfaces, and Films* **1990**, *8*, 1871–1877.

Friedlander 1927-, S. K. (Sheldon K. *Smoke, dust, and haze : fundamentals of aerosol dynamics*; New York : Oxford University Press: New York, 2000.

Fujii, M.; Mimura, A.; Hayashi, S.; Yamamoto, Y.; Murakami, K. *Physical Review Letters* **2002**, *89*, 1–4.

Fujii, M.; Yamaguchi, Y.; Takase, Y.; Ninomiya, K.; Hayashi, S. *Applied Physics Letters* **2004**, *85*, 1158.

Galli, F. Charge and Energy Interactions between Nanoparticles and Low Pressure Plasmas, 2010.

Garcia, G.; Buonsanti, R.; Runnerstrom, E. L.; Mendelsberg, R. J.; Llordes, A.; Anders, A.; Richardson, T. J.; Milliron, D. J. *Nano letters* **2011**, *11*, 4415–20.

Ghosh, A. K. A.; Fishman, C.; Feng, T. *Journal of Applied Physics* **1980**, *51*, 446–454.

Girshick, S. L. *Journal of Nanoparticle Research* **2008**, *10*, 935–945.

Glass, J. A.; Wovchko, E. A.; Yates, J. T. *Surface Science* **1996**, *348*, 325–334.

Godefroo, S.; Hayne, M.; Jivanescu, M.; Stesmans, A.; Zacharias, M.; Lebedev, O. I.; Van Tendeloo, G.; Moshchalkov, V. V *Nature nanotechnology* **2008**, *3*, 174–8.

Goldstein, A. N. *Applied Physics A: Materials Science & Processing* **1996**, *62*, 33–37.

Goldstein, A. N.; Echer, C. M.; Alivisatos, A. P. *Science* **1992**, *256*, 1425–7.

Golusda, E.; Hessenthaler, P.; Mollekopf, G.; Stafast, H. *Applied Surface Science* **1993**, *69*, 258–261.

Gorla, C. R.; Liang, S.; Tompa, G. S.; Mayo, W. E.; Lu, Y. *Journal of Vacuum Science & Technology A: Vacuum, Surfaces, and Films* **1997**, *15*, 860.

Govoni, M.; Marri, I.; Ossicini, S. *Nature Photonics* **2012**, *6*, 672–679.

Gräf, D.; Grundner, M.; Schulz, R.; Mühlhoff, L. *Journal of Applied Physics* **1990**, *68*, 5155.

Gresback, R.; Holman, Z.; Kortshagen, U. R. *Applied Physics Letters* **2007**, *91*, 93119.

Gresback, R.; Hue, R.; Gladfelter, W. L.; Kortshagen, U. R. *Nanoscale research letters* **2011**, *6*, 68.

Gresback, R.; Nozaki, T.; Okazaki, K. *Nanotechnology* **2011**, *22*, 305605.

Grove, A. S.; Leistiko, O.; Sah, C. T. *Journal of Applied Physics* **1964**, *35*, 2695.

Gupta, A.; Swihart, M. M. T.; Wiggers, H. *Advanced functional materials* **2009**, *19*, 696–703.

Hao, X. J.; Cho, E.-C.; Flynn, C.; Shen, Y. S.; Conibeer, G.; Green, M. A. *Nanotechnology* **2008**, *19*, 424019.

Hicks, L.; Dresselhaus, M. S. *Physical Review B* **1993**, *47*, 727–731.

Hinds, W. C. *Aerosol Technology: Properties, Behavior, and Measurement of Airborne Particles*; John Wiley and Sons, Inc, 1999; Vol. 2nd.

Holm, J.; Roberts, J. T. *Journal of Physical Chemistry C* **2009**, *113*, 15955–15963.

Holm, J.; Roberts, J. T. *Journal of the American Chemical Society* **2007**, *129*, 2496–2503.

Holm, J.; Roberts, J. T. *Journal of Vacuum Science & Technology A:* **2010**, *28*, 161.

Holm, J.; Roberts, J. T. *Langmuir* **2007**, *23*, 11217–24.

Holman, Z. C.; Kortshagen, U. R. *Nanotechnology* **2010**, *21*, 335302.

Houston, M. R.; Maboudian, R. *Journal of Applied Physics* **1995**, *78*, 3801.

Iiduka, R.; Heya, A.; Matsumura, H. *Solar Energy Materials and Solar Cells* **1997**, *48*, 279–285.

Irmscher, K.; Klose, H.; Maass, K. *Journal of Physics C: Solid State Physics* **1984**, *17*, 6317–6329.

Ito, M.; Imakita, K.; Fujii, M.; Hayashi, S. *Journal of Physics D: Applied Physics* **2010**, *43*, 505101.

Jain, P. K.; Huang, X.; El-Sayed, I. H.; El-Sayed, M. A. *Accounts of Chemical Research* **2008**, *41*, 1578–86.

Jana, T.; Ray, S. *Thin Solid Films* **2000**, *376*, 241–248.

Joshi, G.; Lee, H.; Lan, Y.; Wang, X.; Zhu, G.; Wang, D.; Gould, R. W.; Cuff, D. C.; Tang, M. Y.; Dresselhaus, M. S.; Chen, G.; Ren, Z. *Nano letters* **2008**, *8*, 4670–4.

Joshi, K. U.; Kabiraj, D.; Narsale, A. M.; Avasthi, D. K.; Warang, T. N.; Kothari, D. C. *Surface and Coatings Technology* **2009**, *203*, 2482–2485.

Ju, L.; Geng, B.; Horng, J.; Girit, C.; Martin, M.; Hao, Z.; Bechtel, H. A.; Liang, X.; Zettl, A.; Shen, Y. R.; Wang, F. *Nature nanotechnology* **2011**, *6*, 630–4.

Jurbergs, D.; Rogojina, E.; Mangolini, L.; U; Kortshagen, U. R. *Applied Physics Letters* **2006**, *88*, 233116.

Kageshima, H.; Shiraishi, K. *Physical Review Letters* **1998**, *81*, 5936–5939.

Kato, K.; Yamasaki, T.; Uda, T. *Physical Review B* **2006**, *73*, 9–12.

Kato, Y.; Ito, T.; Hiraki, A. *Applied Surface Science* **1989**, *41/42*, 614–618.

Kelzenberg, M. D.; Boettcher, S. W.; Petykiewicz, J. A.; Turner-Evans, D. B.; Putnam, M. C.; Warren, E. L.; Spurgeon, J. M.; Briggs, R. M.; Lewis, N. S.; Atwater, H. A. *Nature materials* **2010**, *9*, 239–44.

Kim, S.-K.; Cho, C.-H.; Kim, B.-H.; Park, S.-J.; Won Lee, J. *Applied Physics Letters* **2009**, *95*, 143120.

Kittel, C. *Introduction to solid state physics*; New York : Wiley: New York, 1976.

Knipping, J.; Wiggers, H.; Rellinghaus, B.; Roth, P.; Konjhodzic, D.; Meier, C. *Journal of Nanoscience and Nanotechnology* **2004**, *4*, 1039–1044.

Kortshagen, U. *Journal of Physics D: Applied Physics* **2009**, *42*, 113001.

Kreibig, U.; Vollmer, M. *Optical Properties of Metal Clusters*; Springer: Berlin Heidelberg, 1995.

Kriegel, I.; Jiang, C.; Rodríguez-Fernández, J.; Schaller, R. D.; Talapin, D. V; Da Como, E.; Feldmann, J. *Journal of the American Chemical Society* **2012**, *134*, 1583–90.

Kundu, J.; Le, F.; Nordlander, P.; Halas, N. J. *Chemical Physics Letters* **2008**, *452*, 115–119.

Lacour, F.; Guillois, O.; Portier, X.; Perez, H.; Herlin, N.; Reynaud, C. *Physica E: Low-dimensional Systems and Nanostructures* **2007**, *38*, 11–15.

Ledoux, G.; Gong, J.; Huisken, F. *Applied Physics Letters* **2001**, *79*, 4028.

Ledoux, G.; Guillois, O.; Porterat, D.; Reynaud, C.; Huisken, F.; Kohn, B.; Paillard, V. *Physical Review B* **2000**, *62*, 15942–15951.

Li, S. Q.; Guo, P.; Zhang, L.; Zhou, W.; Odom, T. W.; Seideman, T.; Ketterson, J. B.; Chang, R. P. H. *ACS nano* **2011**, *5*, 9161–9170.

Liptak, R. W.; Kortshagen, U. R.; Campbell, S. A. *Journal of Applied Physics* **2009**, *106*, 064313.

Littau, K. A.; Szajowski, P. J.; Muller, A. J.; Kortan, A. R.; Brus, L. E. *The Journal of Physical Chemistry* **1993**, *97*, 1224–1230.

Liu, C.-Y.; Holman, Z. C.; Kortshagen, U. R. *Advanced Functional Materials* **2010**, *20*, 2157–2164.

Liu, C.-Y.; Holman, Z. C.; Kortshagen, U. R. *Nano Letters* **2009**, *9*, 449–452.

Liu, C.-Y.; Kortshagen, U. R. *Nanoscale* **2012**, *4*, 3963–8.

Lucovsky, G.; Yang, J.; Chao, S.; Tyler, J.; Czubatyj, W. *Physical Review B* **1983**, *28*, 3234–3240.

Luppi, M.; Ossicini, S. *Physical Review B* **2005**, *71*, 1–15.

Luque, A.; Hegedus, S. *Handbook of photovoltaic science and engineering*; John Wiley & Sons Inc: Hoboken, NJ, 2003.

Luque, A.; Marti, A.; Nozik, A. J. *MRS Bulletin* **2007**, *32*, 236–241.

Luther, J. M.; Jain, P. K.; Ewers, T.; Alivisatos, A. P. *Nature materials* **2011**, *10*, 361–6.

Mangolini, L.; Kortshagen, U. R. *Advanced Materials* **2007**, *19*, 2513–2519.

Mangolini, L.; Kortshagen, U. R. *Physical Review E (Statistical, Nonlinear, and Soft Matter Physics)* **2009**, *79*, 26405.

Mangolini, L.; Thimsen, E.; Kortshagen, U. R. *Nano Letters* **2005**, *5*, 655–659.

Manthiram, K.; Alivisatos, A. P. *Journal of the American Chemical Society* **2012**, *134*, 3995–8.

Marra, D. C.; Edelberg, E. A.; Naone, R. L.; Aydil, E. S. *Journal of Vacuum Science & Technology A: Vacuum, Surfaces, and Films* **1998**, *16*, 3199.

Meier, C.; Gondorf, A.; Luttjohann, S.; Lorke, A.; Wiggers, H. *Journal of Applied Physics* **2007**, *101*, 103112–8.

Minnich, A. J.; Dresselhaus, M. S.; Ren, Z. F.; Chen, G. *Energy & Environmental Science* **2009**, *2*, 466.

Miura, T.; Niwano, M.; Shoji, D.; Miyamoto, N. *Journal of Applied Physics* **1996**, *79*, 4373.

Morant, C.; Galán, L.; Sanz, J. M. *Surface and Interface Analysis* **1990**, *16*, 304–308.

Murray, C. B.; Norris, D. J.; Bawendi, M. G. *Journal of the American Chemical Society* **1993**, *115*, 8706–8715.

Nanda, K. K. *European Journal of Physics* **1998**, *19*, 471–472.

Nelson, J. *The physics of solar cells*; London : Imperial College Press: London, 2003; p. 363.

Niesar, S.; Pereira, R. N.; Stegner, A. R.; Erhard, N.; Hoeb, M.; Baumer, A.; Wiggers, H.; Brandt, M. S.; Stutzmann, M. *Advanced Functional Materials* **2012**, *22*, 1190–1198.

Niesar, S.; Stegner, A. R.; Pereira, R. N.; Hoeb, M.; Wiggers, H.; Brandt, M. S.; Stutzmann, M. *Applied Physics Letters* **2010**, *96*, 193112.

Niwano, M.; Kageyama, J.; Kurita, K.; Kinashi, K.; Takahashi, I.; Miyamoto, N. *Journal of Applied Physics* **1994**, *76*, 2157.

Nobili, D.; Armigliato, A.; Finetti, M.; Solmi, S. *Journal of Applied Physics* **1982**, *53*, 1484.

Nolasco, J. C.; Cabré, R.; Ferré-Borrull, J.; Marsal, L. F.; Estrada, M.; Pallarès, J. *Journal of Applied Physics* **2010**, *107*, 044505.

Norris, D. J.; Efros, A. L.; Erwin, S. C. *Science* **2008**, *319*, 1776–9.

Nozik, A. J. *Nano letters* **2010**, *10*, 2735–41.

Nozik, A. J. *Nature Nanotechnology* **2009**, *4*, 548–549.

Nozik, A. J. *Physica E* **2002**, *14*, 115–120.

O'Farrell, N.; Houlton, A.; Horrocks, B. R. *International Journal of Nanomedicine* **2006**, *1*, 451–72.

O'Keeffe, P.; Aoyagi, Y.; Komuro, S.; Kato, T.; Morikawa, T. *Applied Physics Letters* **1995**, *66*, 836.

Ogata, Y.; Tsuboi, T.; Sakka, T.; Naito, S. *Journal of Porous Materials* **2000**, *7*, 63–66.

Pallarès, J.; Cabré, R.; Marsal, L. F.; Schropp, R. E. I. *Journal of Applied Physics* **2006**, *100*, 084513.

Park, S.; Cho, E.; Song, D.; Conibeer, G.; Green, M. A. *Solar Energy Materials and Solar Cells* **2009**, *93*, 684–690.

Pavesi, L.; Dal Negro, L.; Mazzoleni, C.; Franzò, G.; Priolo, F. *Nature* **2000**, *408*, 440–4.

Perego, M.; Bonafos, C.; Fanciulli, M. *Nanotechnology* **2010**, *21*, 025602.

Pereira, R. N.; Rowe, D. J.; Anthony, R. J.; Kortshagen, U. *Physical Review B* **2011**, *83*, 155327.

Perez-Wurfl, I. H.; Hao, X.; Gentle, A.; Kim, D.; Conibeer, G.; Green, M. A. *Applied Physics Letters* **2009**, *95*, 153506.

Petropoulos, J. P.; Cristiani, T. R.; Dongmo, P. B.; Zide, J. M. O. *Nanotechnology* **2011**, *22*, 245704.

Pi, X. D.; Gresback, R.; Liptak, R. W.; Campbell, S. A.; Kortshagen, U. R. *Applied Physics Letters* **2008**, *92*, 2008–2010.

Pi, X. D.; Kortshagen, U. R. *Nanotechnology* **2009**, *20*.

Pi, X. D.; Mangolini, L.; Campbell, S. A.; Kortshagen, U. R. *Physical Review B (Condensed Matter and Materials Physics)* **2007**, *75*, 85421–85423.

Pierreux, D.; Stesmans, A. *Physical Review B* **2002**, *66*, 1–9.

Platzer, M. D. *U . S . Solar Photovoltaic Manufacturing : Industry Trends , Global Competition , Federal Support*; 2012.

Prokes, S. M.; Carlos, W. E. *Journal of Applied Physics* **1995**, *78*, 2671.

Prokes, S.; Carlos, W.; Veprek, S.; Ossadnik, C. *Physical Review B* **1998**, *58*, 15632–15635.

Puigdollers, J.; Voz, C.; Orpella, A.; Martín, I.; Soler, D.; Fonrodona, M.; Bertomeu, J.; Andreu, J.; Alcubilla, R. *Journal of Non-Crystalline Solids* **2002**, *299-302*, 400–404.

Rodríguez-Lorenzo, L.; De la Rica, R.; Álvarez-Puebla, R. A.; Liz-Marzán, L. M.; Stevens, M. M. *Nature materials* **2012**, *11*, 604–607.

Rogak, S. N.; Flagan, R. C. *Journal of Colloid and Interface Science* **1990**, *134*, 206–218.

Rose, A. *Physical Review* **1955**, *97*, 1538–1544.

Ruddy, D. A.; Erslev, P. T.; Habas, S. E.; Seabold, J. A.; Neale, N. R. *The Journal of Physical Chemistry Letters* **2013**, *4*, 416–421.

Salivati, N.; Shuall, N.; Baskin, E.; Garber, V.; McCrate, J. M.; Ekerdt, J. G. *Journal of Applied Physics* **2009**, *106*, 063121.

San Andrés, E.; Del Prado, A.; Martínez, F. L.; Mártil, I.; Bravo, D.; López, F. J. *Journal of Applied Physics* **2000**, *87*, 1187.

Sark, W. van; Meijerink, A. In *Third Generation Photovoltaics*; 2011; pp. 1–28.

Saß, M.; Annen, a.; Jacob, W. *Journal of Applied Physics* **1997**, *82*, 1905.

Satake, T.; Yamamoto, M.; Natio, S.; Mabuchi, M.; Kaneda, A.; Kurahashi, M.; Hashino, T. *Journal of the Chemical Society, Faraday Transactions* **1993**, *89*, 3611.

Satta, A.; Janssens, T.; Clarysse, T.; Simoen, E.; Meuris, M.; Benedetti, A.; Hoflijk, I.; De Jaeger, B.; Demeurisse, C.; Vandervorst, W. *Journal of Vacuum Science & Technology B: Microelectronics and Nanometer Structures* **2006**, *24*, 494.

Schierning, G.; Theissmann, R.; Wiggers, H.; D; Sudfeld, D.; Ebbers, A.; Franke, D.; Witusiewicz, V. T.; Apel, M. *Journal of Applied* **2008**, *103*, 1–6.

Schoisswohl, M.; Cantin, J. L.; Von Bardeleben, H. J.; Amato, G. *Applied Physics Letters* **1995**, *66*, 3660.

Schrotter, J.; Cardenas, A.; Smaihi, M.; Hovnanian, N. *Journal of Sol-Gel Sci. and Tech.* **1995**, *4*, 195–204.

Schultz, O.; Glunz, S. W.; Willeke, G. P. *Progress in Photovoltaics: Research and Applications* **2004**, *12*, 553–558.

Semonin, O. E.; Luther, J. M.; Choi, S.; Chen, H.-Y.; Gao, J.; Nozik, A. J.; Beard, M. C. *Science (New York, N.Y.)* **2011**, *334*, 1530–3.

Shen, P.; Uesawa, N.; Inasawa, S.; Yamaguchi, Y. *Journal of Materials Chemistry* **2010**, *20*, 1669.

Shpaisman, H.; Niitsoo, O.; Lubomirsky, I.; Cahen, D. *Solar Energy Materials and Solar Cells* **2008**, *92*, 1541–1546.

Slack, G. A. In *CRC Handbook of Thermoelectrics*; Rowe, D. M., Ed.; CRC Press: Boca Raton, Fl, 1995; pp. 407–440.

Snyder, G. J.; Toberer, E. S. *Nature materials* **2008**, *7*, 105–14.

Song, Y. J.; Lee, H.-G.; Teng, L.; Anderson, W. A. *MRS Proceedings* **2011**, *638*, F14.22.1.

Stegner, A. R.; Pereira, R. N.; Klein, K.; Lechner, R.; Dietmueller, R.; Brandt, M. S.; Stutzmann, M.; Wiggers, H. *Physical Review Letters* **2008**, *100*, 026803.

Stegner, A. R.; Pereira, R. N.; Lechner, R.; Klein, K.; Wiggers, H.; Stutzmann, M.; Brandt, M. S. *Physical Review B (Condensed Matter and Materials Physics)* **2009**, *80*, 165326 (10 pp.).

Stesmans, A.; Nouwen, B.; Afanas'ev, V. *Physical Review B* **1998**, *58*, 15801–15809.

Stoib, B.; Langmann, T.; Matich, S.; Antesberger, T.; Stein, N.; Angst, S.; Petermann, N.; Schmechel, R.; Schierning, G.; Wolf, D. E.; Wiggers, H.; Stutzmann, M.; Brandt, M. S. *Applied Physics Letters* **2012**, *100*, 231907.

Švrček, V.; Sasaki, T.; Shimizu, Y.; Koshizaki, N. *Applied Physics Letters* **2006**, *89*, 213113.

Švrček, V.; Slaoui, A.; Muller, J. C. *Thin Solid Films* **2004**, *451-452*, 384–388.

Sze, S. M. *Physics of semiconductor devices*; New York, Wiley-Interscience: New York, 2005.

Tan, D.; Xu, B.; Chen, P.; Dai, Y.; Zhou, S.; Ma, G.; Qiu, J. *RSC Advances* **2012**, 8254–8257.

The Information Network *The Global Market for Equipment and Materials for IC Manufacturing*; 2012.

Tiwari, S.; Rana, F.; Hanafi, H.; Hartstein, A.; Crabbé, E. F.; Chan, K. *Applied Physics Letters* **1996**, *68*, 1377.

Trumbore, F. *The Bell System Technical Journal* **1960**, *39*, 205–233.

Tsouroutas, P.; Tsoukalas, D.; Zergioti, I.; Cherkashin, N.; Claverie, A. *Journal of Applied Physics* **2009**, *105*, 094910.

Unpublished Research **2010**.

Van Buuren, T.; Dinh, L. N.; Chase, L. L.; Siekhaus, W. J.; Terminello, L. J. *Physical Review Letters* **1998**, *80*, 3803–3806.

Vasiliev, I.; Chelikowsky, J.; Martin, R. *Physical Review B* **2002**, *65*, 2–5.

Vineis, C.; Shakouri, A.; Majumdar, A.; Kanatzidis, M. G. *Advanced Materials* **2010**, *22*, 3970–80.

Von Behren, J.; Van Buuren, T.; Zacharias, M.; Chimowitz, E. H. H.; Fauchet, P. M. M. *Solid State Communications* **1998**, *105*, 317–322.

W Theiss *Surface Science Reports* **1997**, *29*, 91–192.

Wang, X. W.; Lee, H.; Lan, Y. C.; Zhu, G. H.; Joshi, G.; Wang, D. Z.; Yang, J.; Muto, A. J.; Tang, M. Y.; Klatsky, J.; Song, S.; Dresselhaus, M. S.; Chen, G.; Ren, Z. F. *Applied Physics Letters* **2008**, *93*, 193121.

Wijngaards, D. D. L.; Wolffenbuttel, R. F. *IEEE Transactions on Electron Devices* **2005**, *52*, 1014–1025.

Wilcoxon, J. P.; Samara, G. A.; Provencio, P. N. *Physical Review B* **1999**, *60*, 2704.

Wimbauer, T.; Ito, K.; Mochizuki, Y.; Horikawa, M.; Kitano, T.; Brandt, M. S.; Stutzmann, M. *Applied Physics Letters* **2000**, *76*, 2280.

Winters, B. J.; Holm, J.; Roberts, J. T. *Journal of Nanoparticle Research* **2011**, *13*, 5473–5484.

Yamasaki, T.; Kato, K.; Uda, T. *Physical Review Letters* **2003**, *91*, 3–6.

Yang, D.-Q.; Gillet, J.-N.; Meunier, M.; Sacher, E. *Journal of Applied Physics* **2005**, *97*, 024303.

Yang, J.; Banerjee, A.; Guha, S. *Solar Energy Materials and Solar Cells* **2003**, *78*, 597–612.

Yu, B.; Zebarjadi, M.; Wang, H.; Lukas, K.; Wang, H.; Wang, D.; Opeil, C.; Dresselhaus, M.; Chen, G.; Ren, Z. *Nano letters* **2012**, *12*, 2077–82.

Zamanipour, Z.; Shi, X.; Dehkordi, A. M.; Krasinski, J. S.; Vashaee, D. *Physica Status Solidi (a)* **2012**, *10*, 2049–2058.

Zebarjadi, M.; Esfarjani, K.; Dresselhaus, M. S.; Ren, Z. F.; Chen, G. *Energy & Environmental Science* **2012**, *5*, 5147.

Zebarjadi, M.; Joshi, G.; Zhu, G.; Yu, B.; Minnich, A. *Nano Letters* **2011**, *11*, 2225–2230.

Zhang, N.; Yi, R.; Shi, R.; Gao, G.; Chen, G.; Liu, X. *Materials Letters* **2009**, *63*, 496–499.

Zhang, X.; Brynda, M.; Britt, R. D.; Carroll, E. C.; Larsen, D. S.; Louie, A. Y.; Kauzlarich, S. M. *Journal of the American Chemical Society* **2007**, *129*, 10668–9.

Zhao, J.; Wang, A.; Green, M. A.; Ferrazza, F. *Applied Physics Letters* **1998**, *73*, 1991–1993.

8. APPENDICES

8.1. SUBSTRATE PREPARATION AND DEVICE FABRICATION

8.1.1. SINGLE NC LAYER SOLAR CELLS

The following is the process used in the UMN Nanofabrication Center to prepare the solar cell substrates used in Chapter 4 for single NC layer devices. It has been adapted and modified from a process developed by Zachary Holman.

1. Begin by cleaning a 100 mm, lightly-doped (1-10 Ω-cm) Si wafer with 300 nm oxide layer, using an acetone-methanol-isopropanol-DI water rinse cycle (2x) then drying with compressed N_2.
2. Prebake wafer to > 100 °C for 2 min to remove excess water.
3. Spin coat HDMS at 5000 rpm for 40 s.
    a. Start with spin speed at 0 rpms to avoid wafer damage.
    b. Ensure wafer is centered and held to chuck before ramping speed.
4. Spin photoresist S1813 at 5000 rpm for 40 s.
5. Soft bake at 115 °C for 2 min.
6. Expose using following conditions: 4 s, hard contact, alignment gap = 20 μm. Follow standard aligner/exposure procedure, making sure mask is inserted with the metallic side towards the substrate. Two masks are available for different active area windows, a 3 mm x 3 mm, and a 300 μm x 300 μm.
7. Develop in CD-26 for 45 s, rinse and dry immediately. Active area should be clear.
8. Bake at 125 °C for 2 min.
9. Etch in 10:1 buffered oxide etch (BOE) for 8 min to remove oxide from active area.
10. Immediately rinse in DI water, place in rinse bath, and dry with compressed N_2.
11. Two cycles in solvent baths to remove remaining photoresist
12. Evaporate 200 nm (2 Å/s) of aluminum on unpolished side for back-side contact, using e-beam evaporator. In some experiments where the NC layer was annealed to high temperature, it was necessary to add the back contact as the last step. In this case, the entire device should be etched in BOE for a very short period of time to remove as much native oxidation without removing the NC layer. This should be dome immediately prior to metal deposition.
13. Immediately before NC deposition, etch native oxide from active area by placing in 10:1 BOE for 30 s. Rinse with DI water immediately, and load into deposition chamber as quickly as possible.
14. After NC layer deposition and processing, top contacts were deposited in one of two ways:
    a. Sputter deposition of 60 nm of ITO at 5 mTorr under 20:1 Ar:O flows at 180 °C substrate temperature.
    b. Atomic layer deposition of 100nm of Al:ZnO (20:1) at 180 °C.

8.1.2. CONDUCTIVITY MEASUREMENTS

The following is the “lift-off” process used to fabricate the interdigitated electrodes on glass substrates for conductivity measurements. Reduce baking times from 5 min to 2 min to convert process to one using Si wafers. It has been adapted and modified from a process developed by Zachary Holman.

1. Begin with a 100 mm glass wafer, and clean using an acetone-methanol-isopropanol-DI water rinse cycle (2x) then drying with compressed N_2.
2. Treat glass wafer with ozone plasma for five minutes if additional organic cleaning is desired.
3. Prebake wafer to > 100 °C for 5 min to remove excess water.
4. Spin lift-off resist (LOR 3A) at 5000 rpm for 40 s.
5. Soft bake at 190 °C for 5 min. Set hot plate to temp before adding wafer.
6. Let wafer cool, then spin photoresist S1813 at 5000 rpm for 40 s.
7. Soft bake at 115 °C for 2 min only.
8. Expose using following conditions: 4 s, hard contact, alignment gap = 20 μm. Follow standard aligner/exposure procedure, making sure mask is inserted with the metallic side towards the substrate.
9. Develop in CD-26 for 45 s to remove S1813, rinse with DI water, dry with compressed N_2.
10. Check features using microscope. If necessary to start over, begin with step 1.
11. Bake at 125 °C for 5 min.
12. Develop in CD-26 for 15 s to remove LOR-3A, rinse with DI water, dry with compressed N_2.
13. Check features using microscope. If necessary to start over, begin with step 1.
14. Evaporate 100 nm (2 Å/s) of aluminum using e-beam evaporator.
15. Soak in photoresist stripper 1165 overnight to gently remove lift-off layer. Sometimes heating to 60 °C or gentle sonication will help in generating sharper and less damaged features.
16. Check features using microscope to ensure lift-off worked properly.

8.2. SCIENTIFIC "EXCURSIONS" IN NANOPARTICLE TECHNOLOGY

This appendix outlines several short, preliminary, or unfinished scientific investigations I have undertaken while pursuing my degree. While not directly related to my thesis research, I felt the inclusion of the results obtained from this work was important enough to be documented in case such a topic would be revisited by another researcher.

8.3. INKJET PRINTING (IP)

8.3.1. BACKGROUND

Development of liquid-phase deposition techniques for nanoscale materials is necessary to enable roll-to-roll processing or flexible/inexpensive substrate technologies. Drop casting is relatively crude compared to other techniques, but is favored in some small-scale laboratory applications and to study the drying kinetics of simple colloidal systems. Spin coating is typically used to deposit photoresists during photolithography procedures, as the film thickness can be easily correlated to spin speed and time. For this reason, researchers have looked into spin-coating as a way to deposit colloidal dispersions of SiNCs.[1–3] Even though many commercial systems for spin coating exist, and repeatable procedures have been established, spin coating is still limited to smaller samples, as high rotational speeds require even balancing of the sample. Si and glass wafers work well, up to around 6 inches in diameter. Processing is limited to batches, and much of the liquid initially applied to the substrate is spun off, in order to get complete, even coverage. As an alternative, techniques for colloidal NC deposition, such as transfer printing,[4] screen printing,[5,6] and mist deposition[7,8] are being investigated for applications that require large area coverage.

Complementary to processes which cover large areas, ink-jetting technologies have been proposed as a potential liquid-phase deposition technique because of the deposition precision afforded and advances in electromechanical control. For this reason, researchers have found inkjet printing of colloidal nanomaterials to be useful in rapid prototyping[9], panel displays[10], and thin film transistor applications[11]. In particular, the solar cell industry has been very interested in inkjet printing for fine patterning of top contacts from colloidal silver nanoparticles on conventional c-Si solar cells[12] and on organic solar cells[13], as an alternative to lithographic processes which require deposition of costly materials and subsequent removal of unwanted sections (e.g. lift-off process). The fundamental theory behind inkjet printing focuses on the fluid dynamics of the ink. A pressure wave is created in the ink, either by a thermal expansion or by a physical deformation. This pressure wave forces ink through a small nozzle where the ink is ejected. As the ink leaves the nozzle, the pressure wave is negated or reversed, and due to Rayleigh instability, a drop breaks off from the fluid jet. This drop has sufficient speed to travel towards the intended substrate, and impact with a velocity determined by the amplitude of the initial pressure wave.

It is convenient to organize the challenges of inkjet printing into three categories: material compatibility, device compatibility, and drying kinetics. First, material compatibility deals with the challenges in working with two phase systems, such as ink solubility, wetting characteristics, surface tension, NC surface chemistry, agglomeration, oxidation, and long-term ink stability. Second, device compatibility means the colloidal ink intended for inkjet deposition must be compatible with the inkjet device itself. Inkjet devices typically have a range of fluid properties that a solvent must possess to be effectively jetted. Third, the drying kinetics of the colloidal system are directly related to the fluid properties of the ink. Therefore, before one can engineer inks with favorable drying properties, potential solvents must form stable colloidal solutions with the NCs (so large agglomerates do not clog the inkjet device) and have favorable properties for the jetting process.

Consider inkjet printing onto a piece of paper; the ink is delivered to a spot on the paper, and is subsequently absorbed. The pigment particles contained in the ink are absorbed into the fibers of the paper, and once the delivery solvent dries, the particles remain attached to the paper. This is a very different picture than that of most inkjet-printed colloidal semiconductors. Now consider inkjet printing on a sheet of glass. The drop of ink is impacted onto the glass, and depending on the impaction speed, remains a drop, spreads, or even splashes. The surface energy of the glass could be such that the drop does not spread at all, but remains a sphere as it evaporates. If the drop spreads, spatial resolution decreases. Furthermore, there is no fibrous matrix to hold the NCs in place as the solvent dries, so the NCs are subject to the flows inherent in the drying drop. The fact that the NCs "go with the flow" inside drying drops is one of the biggest challenges in inkjet printing and is referred to as the "coffee ring effect". The "coffee ring effect" is more formally known as pattern formation in drying drops, or sometimes just the "ring effect". The effect is a direct consequence of a solute drying in the presence of a single solvent system. As a liquid drop dries, the line between the liquid and the solid upon which it rests (known as the "contact line") remains stationary. In the terminology of drying kinetics, this is referred to as "pinning". Simultaneously, it is known that under normal conditions, the solvent will evaporate preferentially from the contact line. This preferential evaporation is caused by a difference in the environment an evaporated molecule sees after it leaves the liquid/gas interface. Molecules on the edge see more gas to diffuse into, where molecules evaporating from the center only see an escape directly above them. If they diffuse downwards, they will be reabsorbed into the liquid[14]. Thus, as molecules evaporate from the contact line, more molecules from the interior of the drop flow to the contact line to replace the ones that have evaporated, and in the process carry solute particles towards the edge. This continues either until the drop has completely dried or the angle between the liquid-gas interface and liquid-solid interface reaches a critical value, at which point the contact line is said to slip. If there is enough solute left after the contact line slips, the process will start over again until the drop has dried completely. The resulting pattern resembles that of a dried coffee drop, hence the name.

As one might imagine, effectively depositing a thin, continuous layer of semiconductor material from a solvent requires understand of ring effect kinetics. In fact, it was first studied for semiconductor materials a little over a decade ago[15]. Researchers used CdS and CdSe/CdS NCs, 5 nm in diameter, dispersed in pyridine. The result of the research was to characterize and model drying kinetics for such a system, however no conclusions were made as to whether quality films could be made with such a process. Further studies focused more on the drop drying kinetics, and less on the challenges involved in practical applications.[14–16] The studies involved polystyrene microspheres dispersed in a variety of solvents, and although the research wasn't device oriented, the studies introduced the concept of pinning and showed how different drying drop patterns could be by changing solvents, initial concentrations, etc. Studies since then have involved the use of silica particles because of their convenient imaging properties and ability to self-assemble,[17–19] alumina and zirconia particles to study ceramic deposition for fuel cell and sensor technology,[20] and fluorescent PMMA particles to track the flow of solvent during the drying process.[21] Most recently, Gupta et al. have demonstrated the printing of luminescent Si-NCs on a large scale, however small scale features were not demonstrated.[22] However, the question still remains; how does one make a continuous film from drying drops? The answer is, for a one-solvent system it is very difficult, daresay impossible. Contact line pinning and preferential evaporation will always drag particles to the contact line. However, if the flow inside the drop could be controlled and minimized while the droplet evaporates, perhaps continuous, even deposition could occur.

The requirement for even deposition becomes a two-solvent system. In a two solvent system, the properties of the solvents can be selected to induce a counter-flow to the normally induced evaporative one. This counter-flow can slow down particle transport to the contact line, eliminate completely, or sometimes even reverse it, such that particles congregate near the center of the drop.[23] Specifically, this flow is known as Marangoni flow, and is the result of a surface tension gradient. The surface tension gradient is induced due to the thermal gradient that

exists in an evaporating drop. Since the process of evaporation requires consumption of latent heat, and the heat conduction path in the drop is longer in the center than near the contact line, the surface temperature of the drop is lower near the center. This in turn decreases the surface tension at the center of the drop, establishing a gradient. Subsequently, a Marangoni flow is induced from regions of low surface tension (edge) to regions of high surface tension (center). In general, a Marangoni flow is induced even in a single solvent system, however, the effect compared to the convective flow towards the contact line is minimal. If a two solvent system is used instead, the properties of the solvents can be selected such that the magnitude of the Marangoni flow is comparable to the convective outward flow. Consider a two solvent system, with a high- and low-boiling point solvent. Both solvents will preferentially evaporate from the contact line, however, the low boiling point solvent will evaporate faster, eventually leaving a higher concentration of the high boiling point solvent near the contact line. If the solvents are selected such that the high boiling point solvent has a *lower* surface tension than the low boiling point solvent, then one has artificially induced a surface tension gradient, and the subsequent Marangoni flow.[23] Marangoni flow has been studied for two solvent systems of pristine solvents,[24,25] organosiloxane-based organic-inorganic hybrid materials,[23] silver, silver sulfide, cobalt, copper, cadmium sulfide, and ferrite nanoparticles,[26,27] and silica particles ejected from an inkjet device[18]. One study focused on using inkjet deposition of polystyrene spheres to demonstrate effectiveness for LED applications.[28] The study demonstrated the ability of a two solvent system and an inkjet device to form an ordered array of polymer dots. In another study, researchers used an inorganic/organic hybrid material with an inkjet deposition procedure to fabricate thin film transistors.[23] A recent study investigated the use of self-assembly due to Marangoni flow from an inkjetted drop.[29] Researchers used an organic molecule and varied the flow velocity to induce self-assembled molecular crystallization.

8.3.2. OBJECTIVE

The purpose of this study was to develop a system to inkjet print colloidal SiNCs. This involved identification of challenges associated with current ink formulations and their compatibility with printing processes, identification of suitable solvents for ink formulation, and a preliminary understand of drying kinetics of nanoscale materials at a microscopic scale.

8.3.3. RESULTS

The inkjet deposition system consists of a MicroFab Inc, piezo-electric inkjet device (MJ-ATP-01). The piezo-electric crystal is driven by a MicroFab, Inc. JetDrive III device controller. The controller supplies a voltage pulse to the piezo-electric crystal to induce a pressure wave in the reservoir ink. The controller uses a PC interface to adjust the voltage waveform. Underneath the device, two Standa motorized translation stages (8MT167-100-4247) were mounted at 90° to each other to provide a PC controlled two-axis stage for printing lines, films, and other designs. The stages were controlled using a custom designed LabVIEW program. A ceramic-plate heater was mounted to the top stage to allow heating during deposition. Inks were filtered using a 0.2 µm porous filter before inkjetting. The entire deposition system was placed inside a glovebox with a N_2 ambient to avoid oxidation of the NCs. A diagram of the system and a close-up image can be found in Figure IP(a,b).

Initial experiments tested the feasibility of printing 1-dodecene hydrosilylated, 5 nm SiNCs dispersed in toluene or mesitylene. Films were deposited on glass for optical characterization and a bare Si wafer for scanning electron microscopy (SEM) using a JEOL 6500 microscope. Thickness profiles were measured using a Dektak 3030 Surface Profiler. On optical micrograph and digital photograph of the resulting films is shown in Figure IP(c,d). Films made from a single pass of the inkjet system were too thin to see, however, multiple passes of the inkjet device produced very rough films. This is because the initial drop landed on a clean substrate, and wetting properties were favorable. However, as the drop dried, the inevitable ring pattern formed, and subsequent layers did not wet as evenly. Eventually the ring patterns overlapped and produced a very rough film profile, as shown in Figure IP(e). Efforts to increase the NC

concentration of the ink resulted in increased susceptibility of the inkjet device to clog. Terpineol was added as an anti-coagulant, however the alcohol group in terpineol rapidly oxidized the SiNCs and the resulting agglomeration caused so much clogging that the terpineol actually had the opposite effect from intended. Furthermore, it was found that many of these films cracked upon rapid thermal annealing at 700 °C, due to the removal of 1-dodecene sections from the film interior. The cracking was observed using SEM as shown in Figure IP(f).

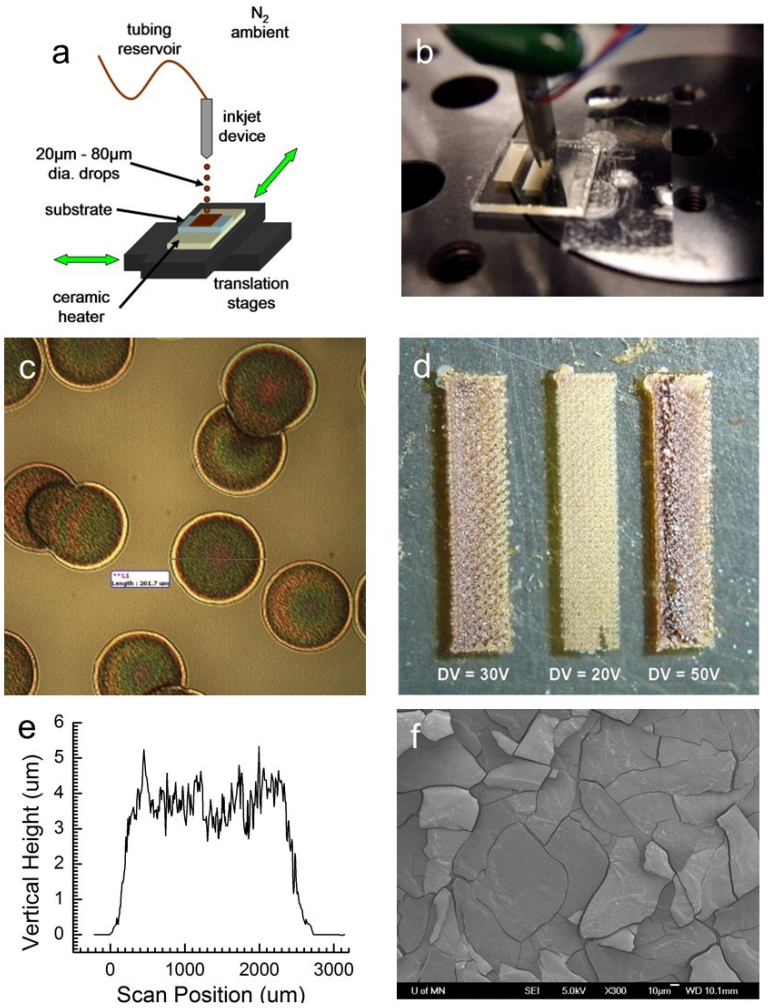

Figure IP (a-f). (a,b)Inkjet printing system diagram and close-up photo of inkjet deposition, (c,d) inkjetted drops and films of 1-dodecene hydrosilylated 5 nm SiNCs dispersed in toluene: (d) illustrates the large build-up of NCs near the drop edge, (c) three films made by varying the driving voltage (DV) of the inkjet device. In each film, the left edge was printed first, and in the 30V and 50V case, a build-up of NCs occurs during drying due to a laterally-induced ring effect within the film, (e) thickness profile of an inkjet printed film of 5 nm 1-dodecene functionalized, SiNCs dispersed in mesitylene, (f) SEM of SiNC film from inkjet deposition after rapid thermal annealing at 700 °C

Serendipitously, it was discovered that 5 nm GeNCs produced from germanium tetrachloride and dispersed in 1,2-dichlorobenzene (1,2-DCB) formed stable colloids without any ligand attachment. Since the ligands were causing many of the problems with inkjetting SiNCs, it was decided that developing an understanding of the GeNC/1,2-DCB colloid could help later on if suitable solvents were discovered for of SiNCs (1,2-DCB did not produce a stable colloid with SiNCs). From the previous experiments, single solvent ink formulations were ruled insufficient for inkjetting, so the next set of experiments focused on two solvent systems and the associated

drying kinetics. Lim et al. proposed in their study on molecular crystallization and Marangoni flows that a mixture of 1,2-DCB and chlorobenzene (CB) could reduce the ring effect.[29] Consequently, inks of varying composition of 1,2-DCB and CB were made and printed to evaluate if the ring effect could be reduced for drying drops of GeNC colloids. In this case, inks *were not* filtered before inkjetting, so the effect of the additional CB on agglomeration could be observed more easily. Even without filtering, the GeNC/1,2-DCB/CB inks printed much easier than the SiNC/toluene inks, with less clogging occurrences. Inks were printed on gold coated Si for SEM. Qualitatively, it appears as though the introduction of CB did reduce the ring effect, and in fact almost reversed it. Figure IP(g-i) shows a SEM image of one drop deposited from pure 1,2-DCB and one drop deposited from a 2:1 ratio of CB:1,2-DCB. The pure 1,2-DCB ink shows an increased buildup of agglomerated NCs near the edge of the drop, while the mixed ink shows the buildup near the center. This is interesting because the combination of 1,2-DCB and CB satisfies the boiling point (BP) condition of Marangoni flow, but does not satisfy the surface tension (ST) condition (high BP-low ST / low BP-high ST, see Table B1). Nonetheless, since NC transport is limited by the viscosity of the ink, it was theorized that increasing the mass loading would slow down NC transport and lead to more even coverage within the interior of the drop. Figure IP(i) shows the effect of increasing the GeNC loading by a factor of five. A much more even coverage is achieved, however not a continuous coverage. It must also be noted that agglomeration has occurred, as the GeNC sizes appear to be almost 1 μm in diameter, instead of the 5 nm as-synthesized primary GeNCs.

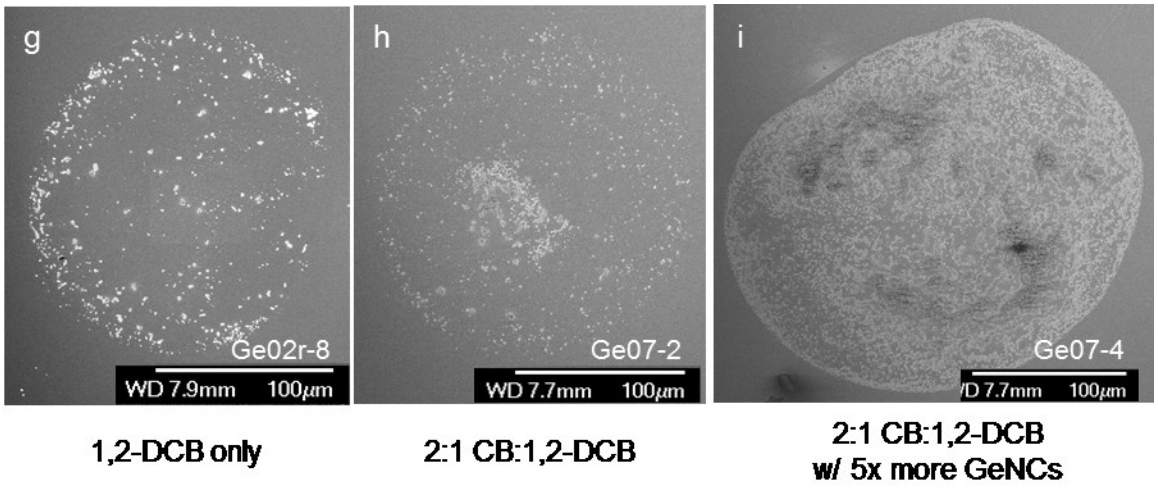

Figure IP(g-i). Ring patterns from dried drops of GeNCs dispersed in varying amounts of 1,2-DCB and chlorobenzene, and at varying mass concentrations

Table IP1. Fluid properties of GeNC inks

Solvent	*Boiling Point [°C]*	*Surface Tension [mN/m]*
1,2-DCB	180	36.6
Chlorobenzene	131	33.0

8.3.4. CONCLUSIONS

From the inkjetting experiments, two main conclusions should be drawn. The first is that ink formulation is crucial to successfully inkjet print colloidal NC inks. The compatibility of the solvents with the NC and the inkjet device limit the number of solvent candidates available for engineering inks which exploit induced flows for even NC deposition within individual drops and films. Based on this, we also conclude that much more research is needed to identify suitable solvents for SiNCs and GeNCs to form stable colloidal inks. The opportune discovery of 1,2-DCB allowed us to perform preliminary inkjetting experiments, however, to proceed successfully it would be useful to have a library of compatible solvents for ink formulation. Likely, this will require consideration of how material properties such as NC concentration, surface chemistry, surface charge, and size affect the colloidal ink stability.

8.3.5. REFERENCES

(1) Lechner, R.; Stegner, A. R.; Pereira, R. N.; Dietmueller, R.; Brandt, M. S.; Ebbers, A.; Trocha, M.; Wiggers, H.; Stutzmann, M. *Journal of Applied Physics* **2008**, *104*, 53701.

(2) Liu, C.-Y.; Holman, Z. C.; Kortshagen, U. R. *Nano Letters* **2009**, *9*, 449–452.

(3) Nayfeh, O. M.; Antoniadis, D. A.; Mantey, K.; Nayfeh, M. H. *Applied Physics Letters* **2009**, *94*, 043112 (3 pp.).

(4) Kumar, B.; Tan, H. S.; Ramalingam, N.; Mhaisalkar, S. G. *Carbon* **2009**, *47*, 321–324.

(5) Vadivel Murugan, A.; Oh, Y. H.; Ravi, V.; Viswanath, A. K. *Journal of Materials Science* **2006**, *41*, 1459–1464.

(6) Llobet, E.; Ivanov, P.; Vilanova, X.; Brezmes, J.; Hubalek, J.; Malysz, K.; Gràcia, I.; Cané, C.; Correig, X.; Gracia, I.; Cane, C. *Sensors and Actuators, B: Chemical* **2003**, *96*, 94–104.

(7) Moss, R. W.; Lee, D. H.; Vuong, K. D.; Condrate, R.; Condrate Sr., R. A.; Wang, X. W.; DeMarco, M.; Stuckey, J. *Journal of non-crystalline solids* **1997**, *218*, 105–112.

(8) Zhu, T.; Shanmugasundaram, K.; Price, S. C.; Ruzyllo, J.; Zhang, F.; Xu, J.; Mohney, S. E.; Zhang, Q.; Wang, A. Y.; J *Applied Physics Letters* **2008**, *92*, 23111.

(9) Derby, B.; Reis, N. *MRS Bulletin* **2003**, *28*, 815–818.

(10) Arias, A. C.; Daniel, J.; Krusor, B.; Ready, S.; Sholin, V.; Street, R. *JOURNAL OF THE SOCIETY FOR INFORMATION DISPLAY 15*, 485–490.

(11) Barret, M.; Sanaur, S.; Collot, P. *Organic Electronics: physics, materials, applications* **2008**, *9*, 1093–1100.

(12) Kim, D.; Jeong, S.; Park, B. K.; Moon, J. *Applied Physics Letters* **2006**, *89*.

(13) Noguchi, Y.; Sekitani, T.; Yokota, T.; Someya, T. *Applied Physics Letters* **2008**, *93*, 43303.

(14) Deegan, R. D. R.; Bakajin, O.; Dupont, T. T. F.; Huber, G.; Nagel, S. S. R.; Witten, T. A. *Physical Review E - Statistical Physics, Plasmas, Fluids, and Related Interdisciplinary Topics* **2000**, *62*, 756–765.

(15) Maenosono, S.; Dushkin, C. D.; Saita, S.; Yamaguchi, Y. *Langmuir* **1999**, *15*, 957–965.

(16) Deegan, R. D. *Physical Review E (Statistical Physics, Plasmas, Fluids, and Related Interdisciplinary Topics)* **2000**, *61*, 475–485.
(17) Ko, H.-Y.; Park, J.; Shin, H.; Moon, J. *Chemistry of Materials* **2004**, *16*, 4212–4215.
(18) Park, J.; Moon, J. *Langmuir* **2006**, *22*, 3506–3513.
(19) Okubo, T.; Nakagawa, N.; Tsuchida, A. *Colloid and Polymer Science* **2007**, *285*, 1247–1255.
(20) Ramakrishnan, N.; Rajesh, P. K.; Ponnambalam, P.; Prakasan, K. *Journal of Materials Processing Technology* **2005**, *169*, 372–381.
(21) Hu, H.; Larson, R. G. *Journal of Physical Chemistry B* **2006**, *110*, 7090–7094.
(22) Gupta, A.; Khalil, A. S. G.; Winterer, M.; Wiggers, H. In *Technical Proceedings of the 2010 NSTI Nanotechnology Conference and Expo*; IEEE Computer Society: IVG, University of Duisburg-Essen, Lotharstr.1, 47057, Duisburg, Germany, 2010; Vol. 2, pp. 538–541.
(23) Jeong, S.; Kim, D.; Moon, J. *Journal of Physical Chemistry C Letters* **2008**, *112*, 5245–5249.
(24) Pesach, D.; Marmur, A. *Langmuir* **1987**, *3*, 519–524.
(25) Fanton, X.; Cazabat, A. M. *Langmuir* **1998**, *14*, 2554–2561.
(26) Maillard, M.; Motte, L.; Ngo, A. T.; Pileni, M. P. *Journal of Physical Chemistry B* **2000**, *104*, 11871–11877.
(27) Johnson J., D. D.; Kang, B.; Vigorita, J. L.; Amram, A.; Spain, E. M. *Journal of Physical Chemistry A* **2008**, *112*, 9318–9323.
(28) De Gans, B.-J.; Schubert, U. S. *Langmuir* **2004**, *20*, 7789–7793.
(29) Lim, J. A.; Lee, W. H.; Lee, H. S.; Lee, J. H.; Park, Y. D.; Cho, K. *Advanced Functional Materials* **2008**, *18*, 229–234.

8.4. METAL-INDUCED CRYSTALLIZATION OF A-SI/SINC FILMS (MIC)

8.4.1. BACKGROUND

Annealing is usually defined in terms of metallurgy or glassworking, where heat treatment is used to cause a change in material properties or remove stresses. Sintering is usually defined as process by which a powder is heated to a temperature below its melting point until the powder particles adhere to each other. In the case of thin films from SiNCs, annealing may change the surface of the Si, remove defects within the NCs, activate dopants, or reduce film stresses from deposition, while sintering is typically associated with enhancement of grain size and micro-structural changes. Most literature does not make the distinction between annealing and sintering, and perhaps in the case of thin films made from SiNCs, the distinction is hazy because of the unique nature of the material. In an effort to reduce confusion, the term "annealing" will be used in this discussion; however it should be noted that the observations discussed are actually a combination of annealing and sintering.

The use of thermal annealing has been well studied for many materials, including almost all forms of Si. This is usually done in a tube furnace or a rapid thermal annealing furnace. The tube furnace is usually used to bring Si wafers up to temperature for dopant diffusion, oxidation growth, etc, and requires long time scales. A rapid thermal annealing furnace (RTA) is slightly different. During some dopant implantation processes, the crystalline structure of a Si wafer is damaged. A RTA is used to repair these defects on a time scale faster than diffusion can occur. In the case of Si thin films, the literature is sparse regarding the effects of thermal annealing. Several studies focus on thermal annealing of a-Si to create large sized grains, only a few of which are referenced here.[1–4] Some work has focused on μc-Si formed through milling, then annealed under pressure to temperatures just below the bulk melting temperature.[5] A few studies have focused on the effect of melting temperatures due to high temperature annealing of SiNCs,[6,7] however, these studies usually involve only a few NCs to facilitate microscopic characterization. Annealing of thin films deposited from solution phase hydrosilylated NCs had been studied within the Kortshagen group recently.[8] Several results of that study illustrated the challenges inherent with thin film annealing. First of all, it was found that films deposited from hydrosilylated NCs cracked during annealing, and the cracking was typically thickness dependent. The thicker films would routinely crack more often than thin films. This was explained later by Zak Holman, who measured the gas by-products during an annealing process, and found that long sections of the ligand used to hydrosilylate the NCs were being removed from the film.[9] This led to a large volume reduction of matter from the film, and subsequently increased film stresses. The thin films had inherently less matter to lose, and thus less annealing-induced stress, therefore they didn't crack. However, thin films from gas-phase impaction have yet to be studied in depth.

One interesting subset of thermal annealing is a phenomenon known as metal-induced crystallization (MIC). It has been observed that layers of some metals deposited on a-Si will drastically reduce the crystallization temperature of the a-Si film. This is thought to be due to an interaction between the free electrons from the metal and covalent Si bonds near the growing interface.[10] This has been demonstrated in a variety of metals, but most notably nickel,[11] aluminum,[12] and gold[10,13]. It is theorized that the metal easily diffuses through the a-Si and in its wake forms crystallized Si as the free energy of the crystal tries to minimize itself.[13] This type of crystallization could be useful for applications involving heat sensitive substrates, such as plastic or glass, since MIC temperatures are in the 200 - 400 °C range.

Alternatively, laser annealing also seems to be of much more interest to the research community as of late, and for a variety of reasons. One, much higher energy and power densities can be delivered by lasers compared to those delivered by tube or RTA furnaces. Secondly, laser annealing allows precise placement of the energy due to the small size of the beam.

Thirdly, laser light can be tuned to be absorbed in the top layer of a material, so that the penetration depth of the induced heating can be controlled.

Much of the laser annealing literature is focused on the low temperature crystallization of a-Si. For example, a-Si films deposited from RF PECVD was irradiated by an XeCl excimer laser, and the resulting films were studied using Raman scattering.[14] It was concluded that laser irradiation could crystallize the films, but under the right conditions could also force the film to solidify in the amorphous state. In another study, a-Si films from PECVD were irradiated with a CW Nd:YAG laser to study crystallization on glass substrates.[15] The study concluded that good quality poly-Si films could be fabricated using a CW Nd:YAG laser in concert with a pulsed KrF laser. In yet another study, a-Si was irradiated using a method in which the beam from a pulsed Nd:YAG laser was split in three, and then directed towards the film.[16] The three beams produced a 2-D interference pattern on the film, and as a result, the crystallization and grain sizes could be controlled by altering the beam intensities.

While the a-Si literature provides a standard for grain growth and laser operating parameters, laser interactions with nc-Si need to be studied separately. The surface roughness of nc-Si has been studied after irradiation from a CW Ar laser.[17] It was found that the laser energy needed to crystallize a film decreases as the surface roughness increases. Two studies used aqueous dispersions of SiNCs to form thin films.[18,19] The dispersions were deposited on plastic substrate and some were allowed to dry while others remained wet. Then, before they were exposed to CW Nd:YAG laser irradiation. It was found that the wet forming method produced more continuous films than the dry forming method, and neither method led to damage of the underlying substrate.

Lastly, two published studies of laser annealed doped SiNCs formed via microwave plasma synthesis were studied for their thermoelectric and electrical properties. The first study found that thermopower is only observed for films irradiated with a certain threshold energy density.[20] Above this energy density, no enhancement in the thermopower is observed. The study also showed that the thermopower varied with doping concentration, and the optimal doping concentration was around 10^{19} cm^{-3}. The electrical properties study used similar particles but characterized the conductivity of the films.[21] Similar to the thermopower, the electrical conductivity was found to increase dramatically at a certain threshold laser energy density and above this energy density, little increase in the electrical conductivity was observed. Unlike the thermopower, the optimal doping concentration was different for each dopant. B doping needed to be at least 10^{18} cm^{-3} for a 6 order-of-magnitude increase in the conductivity, while phosphorous doping needed to be almost 10^{20} cm^{-3} before a similar increase in electrical conductivity was observed.

8.4.2. RESULTS AND DISCUSSION

Preliminary experiments also provide some qualitative results regarding thermal annealing. For liquid phase deposition films, rapid thermal annealing to 700 °C in air or forming gas almost always produces cracking of the film, as described above. For very thin films, cracking did not occur, however no micro-structural changes were observed with SEM or visually. Lower temperature annealing to 400 °C showed similar effects but required longer annealing times. On the other hand, gas phase impaction deposited films annealed to 400 °C in a N_2 ambient were always easier to image during SEM than those that weren't. SEM imaging is very dependent on the samples ability to disperse the charge from the electron beam used for imaging. Non-conductive samples tend to build up charge on the surface and the incoming electron beam is deflected from its intended location, causing images to turn fuzzy or cloudy, and image resolution to decrease. On the other hand, conductive films are very easy to image as the charge is dissipated very quickly. It is suggested that annealing at 400 °C removes some of the silyl

radicals physi-sorbed to the NC surface that act as charge trap states, and in turn increases image resolution.

Impacted films show no micro-structural change after annealing to 500 °C in N_2 or 1100 °C in air. The exception to this observation is that films deposited on gold coated Si and annealed to 400 and 500 °C in N_2 for 30 min exhibit metal induced crystallization. Deposition and synthesis conditions are given in Table MIC1. Figure MIC(a-e) shows a magnification series of top down SEM images of a MIC films, while Figure MIC(f) shows a cross section at the interface of a crystallized region and an as-deposited region. It appears that the crystallization processes has produced larger grains of crystalline material, but at the same time increased pore size within the film. A photograph of similar films deposited on gold coated Si (Au:Si) and glass is shown in Figure MIC(i). The dark area is the MIC region, and during annealing it can be seen to form with the naked eye. Preliminary XRD experiments suggest that MIC has indeed occurred, as crystallite size is seen to grow when measured via the Scherrer method. The XRD patterns are shown in Figure MIC(g), and a graphical comparison is shown in Figure MIC(h). Crystallite size increases by almost four times in either case. Furthermore, observations during the annealing process indicate the MIC process is heating rate dependent. Films in which the final temperature was achieved quickly exhibited MIC, while slower rates of temperature increase didn't induce MIC in any films.

Table MIC1. Synthesis and deposition conditions for sample Si30e (MIC)

SiH_4 FR	*Ar FR*	*Total Pressure*	*SiH_4 PP*	*Power*	*Film Thickness*
[sccm]	*[sccm]*	*[Torr]*	*[mTorr]*	*[W]*	*[μm]*
0.66	66	2.9	29	180	3.0

Lastly, a few preliminary results regarding the effects of laser annealing will be presented. Several experiments with Nd:YAG pulsed laser annealing of drop cast films were presented by Cram, 2008. Most of the laser annealing and SEM characterization was done by this author and complimentary data will be presented. The focus of that research was on the effect laser annealing has on the conductivity of drop cast films of hydrosilylated SiNCs dispersed in toluene. The laser used was a Continuum Nd:YAG pulsed laser, with 532 nm harmonic being used for all annealing, and all annealing was done in vacuum around 1 Torr. The pulses had a FWHM of 6 ns, were repeated at a frequency of 1 Hz, and had an average energy density of 240 mJ/cm^2 per pulse. An important observation was that laser annealing alone was typically not enough to affect the film structure. As deposited films were usually too transparent to absorb enough laser light. It was found that thermally annealing the films at 400 °C for 30 min in N_2 was necessary before laser annealing. After this pre-anneal step, laser annealing drastically changed the structure of the films. Several SEM images of laser annealed films are presented to qualitatively analyze the process of pulsed laser annealing. Figure MIC(j-k) shows cross sections of a laser annealed film. The irregularities in the film in Figure MIC(j) come from improper beam conditioning, which was near the edge of the beam. Figure MIC(k) was a region of the laser annealed film closer to the center of the beam spot, and it appears that the top layer of the film has melted and solidified, giving a wavy shape to the surface of the film. Figure MIC(l-n) shows a series of films treated with an increasing number of laser pulses. Figure MIC(l) is an as deposited film, with a large contaminant particle in the center for scale. Figures MIC(m,n) have received 5 and 10 pulses, respectively. While 5 pulses seemed to pit the surface slightly, 10 pulses seemed to melt the surface, causing molten Si to solidify in drops of about 300 nm in diameter.

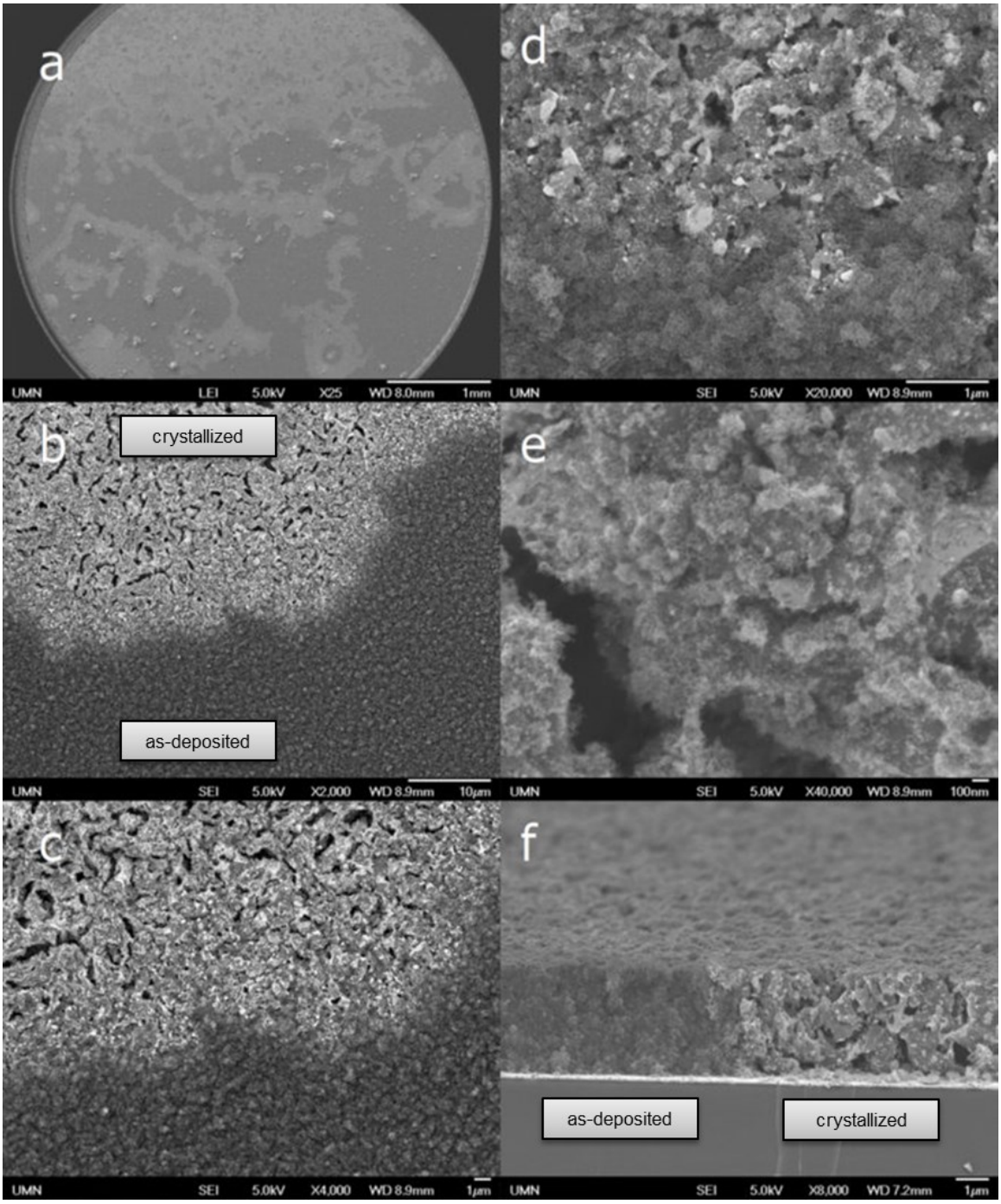

Figure MIC(a-f). A magnification series of MIC observed in a impacted SiNC film (a-e) and a cross section of a MIC region (f).

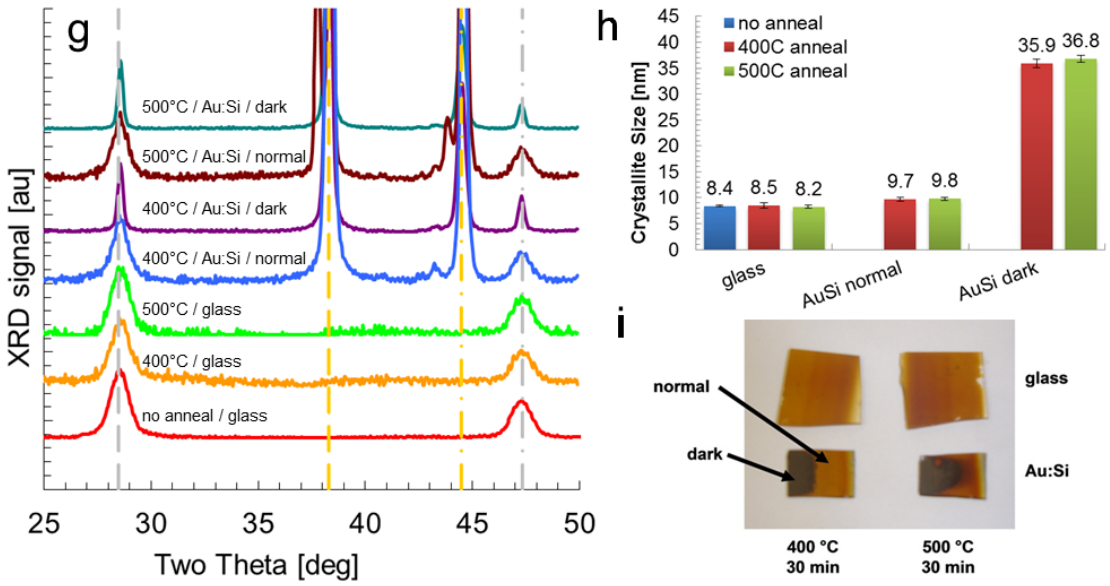

Figure MIC(g-i). (g) XRD patterns of MIC films and (h) graphical comparison of the crystallite sizes as measured via the Scherrer method on the (111) reflection The peaks at 2θ = 28.5°, 47.4° indicate Si planes (111) and (220), the peaks at 2θ = 38.3°, 44.5° are gold (111) and (200) planes. (i) Photograph of SiNC films deposited on glass and gold coated Si where MIC has been observed.

Alternatively, a CW laser diode operating at 834 nm was used to anneal inkjet deposited films. Annealing with the diode laser was done in N_2 at atmospheric pressure. The power density was approximately 20 W/cm^2 although accurately characterizing the spot size was difficult. This beam was much smaller than that of the pulsed laser, as it was focused to achieve a higher power density. As a result, the sample surface needed to be precisely placed at the focal point to achieve sufficient power density. A small laser induced plasma (LIP) was observed when the placement was optimized, and this was used as a standard for subsequent experiments. The laser was scanned over a small region using the two-axis stage at a speed of approximately 1 mm/s. Figure MIC(o) shows a representative sample of a film annealed with the CW diode laser. The annealed region seems to buckle due to the thermally induced stresses associated with the film heating from laser light absorption. Furthermore, the small dusty-like features on the annealed and un-annealed regions suggest that some vaporized Si could have condensed out of the LIP, onto the film surface. Figure MIC(p) shows another SEM image where the laser path cuts through the middle of the film, inducing a large stress that causes the film to buckle. On the far left side of the image, additional cracking similar to that observed during thermal annealing is also observed.

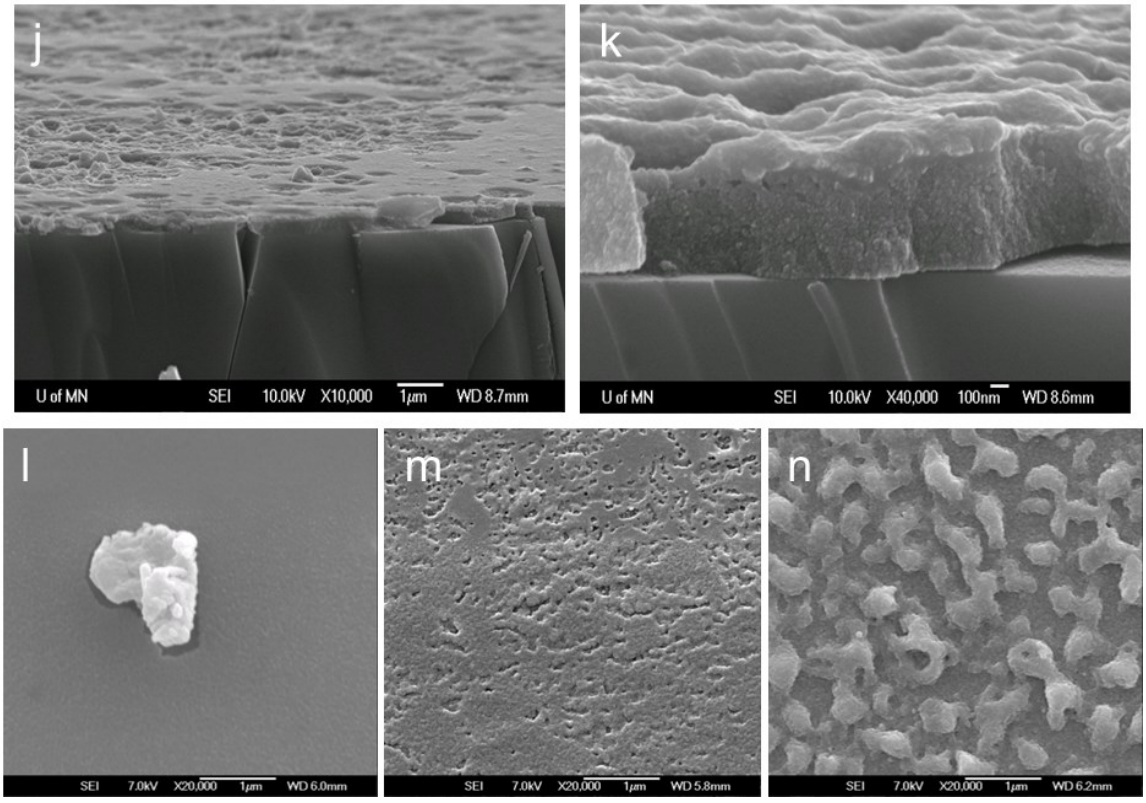

Figure MIC(j-n). Pulsed laser annealed SiNC film from drop cast deposition (j) edge of beam, (k) center of beam. (l-n) Pulsed laser annealed SiNC film from drop cast deposition (l) 0 pulses (m) 5 pulses (n) 10 pulses. The agglomerate in (l) was used for focusing on the very smooth surface, and is not representative of the film.

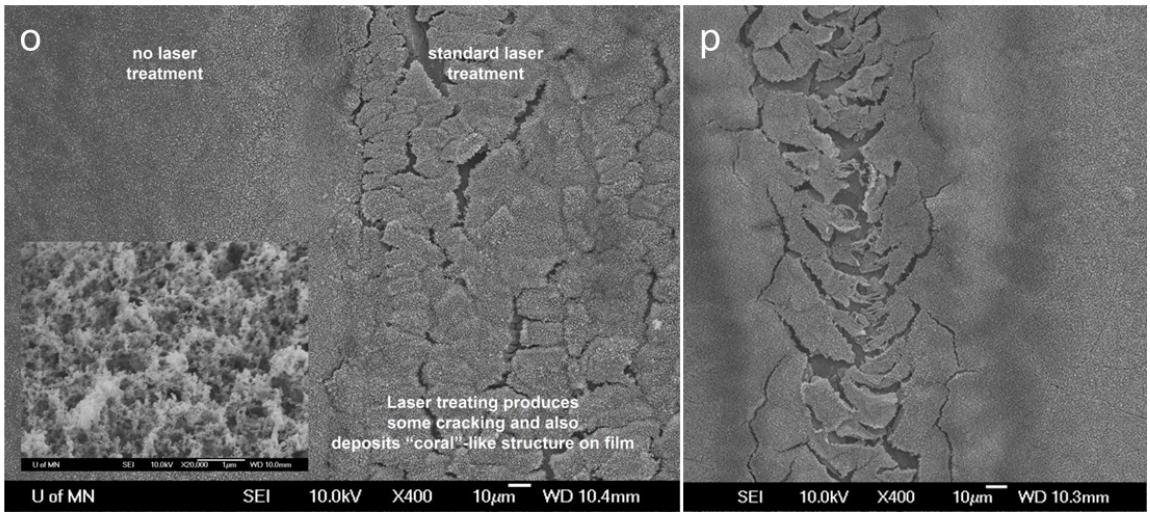

Figure MIC(o-p) (o) SEM image of an inkjet deposited film of SiNCs laser annealed using a CW diode laser operating at 834 nm (inset shows re-deposited material). (p) SEM image of an inkjet deposited film of SiNCs laser annealed using a CW diode laser operating at 834 nm with additional cracking away from the laser path.

8.4.3. REFERENCES

(1) Szekeres, A.; Gartner, M.; Vasiliu, F.; Marinov, M.; Beshkov, G. *Journal of Non-Crystalline Solids* **1998**, *227-230*, 954–957.

(2) Yi, J.; Wallace, R.; Palmer, J.; Anderson, W. A. *Solar Energy Materials and Solar Cells,* **1994**, *33*, 145–155.

(3) Moon, S.-J.; Lee, M.; Grigoropoulos, C. P. *Micro/nanoscale heat transfer* **2002**, *124*, 253–264.

(4) Gamulin, O.; Ivanda, M.; Desnica, U. V; Furic, K. *Journal of Non-Crystalline Solids* **1998**, *227-230*, 943–948.

(5) Gombia, E.; Panizzieri, R.; Salviati, G.; Vidal, J. *Journal of Crystal Growth* **1987**, *84*, 621–628.

(6) Goldstein, A. N. *Applied Physics A: Materials Science & Processing* **1996**, *62*, 33–37.

(7) Schierning, G.; Theissmann, R.; Wiggers, H.; D; Sudfeld, D.; Ebbers, A.; Franke, D.; Witusiewicz, V. T.; Apel, M. *Journal of Applied* **2008**, *103*, 1–6.

(8) Cram, R. A. Silicon films from silicon nanocrystal inks for low-cost printable electronics and photovoltaics, Thesis (M.S.)-- of Minnesota, 2008. Major: Mechanical engineering, 2008.

(9) Holman, Z.; Kortshagen, U. R. *Langmuir* **2009**, *25*, 11883–11889.

(10) Ru-Yuan, Y.; Weng, M. M.-H.; Liang, C.-T. C.; Yan-, S.; Yang, R.-Y.; Su, Y.-K.; Shy, S.-L. *Japanese Journal of Applied Physics* **2006**, *45*, 1146–1148.

(11) Ishida, Y.; Nakagawa, G.; Asano, T. *Japanese Journal of Applied Physics, Part 1: Regular Papers and Short Notes and Review Papers* **2007**, *46*, 6437–6443.

(12) Wang, J. Y.; Wang, Z. M.; Jeurgens, L. P. H.; Mittemeijer, E. J. *Journal of Nanoscience and Nanotechnology* **2009**, *9*, 3364–3371.

(13) Wang, Z.; Jeurgens, L. L. P. H.; Wang, J. J. Y.; Mittemeijer, E. J. *Advanced Engineering Materials* **2009**, *11*, 131–135.

(14) Sameshima, T.; Usui, S. *Applied Physics Letters* **1991**, *59*, 2724–2726.

(15) Sinh, N. D.; Andra, G.; Falk, F.; Ose, E.; Bergmann, J. *Solar Energy Materials and Solar Cells* **2002**, *74*, 295–303.

(16) Dahlheimer, B.; Karrer, U.; Nebel, C. E.; Stutzmann, M. *Journal of Non-Crystalline Solids,* **1998**, *227-230*, 916–920.

(17) Hadjadj, A.; Boufendi, L.; Huet, S.; Schelz, S.; Roca, i. C.; Estrade-Szwarckopf, H.; Rousseau, B. *Journal of Vacuum Science & Technology A (Vacuum, Surfaces, and Films)* **2000**, *18*, 529–535.

(18) Bet, S.; Kar, A. *Materials Science and Engineering B* **2006**, *130*, 228–236.

(19) Bet, S.; Kar, A. *Journal of Electronic Materials* **2006**, *35*, 993–1004.

(20) Lechner, R.; Wiggers, H.; Ebbers, A.; Steiger, J.; Brandt, M. S.; Stutzmann, M. *Physica Status Solidi - Rapid Research Letters* **2007**, *1*, 262–264.

(21) Lechner, R.; Stegner, A. R.; Pereira, R. N.; Dietmueller, R.; Brandt, M. S.; Ebbers, A.; Trocha, M.; Wiggers, H.; Stutzmann, M. *Journal of Applied Physics* **2008**, *104*, 53701.

8.5. BORON PHOSPHIDE NANOPARTICLES (BP)

8.5.1. BACKGROUND

Boron phosphide (BP) is a wide band gap semiconductor (Eg ~ 2.0 eV) and has been studied for its optical properties, such as photoluminescence,[1] but mostly as a potential material for thermoelectrics.[2,3] However, since its discovery in 1957,[4] few researchers have investigated the material. A survey of ISI Web of Knowledge, only returns 104 total citations for the phrase "boron phosphide" since that time. In other words, approximately 2 papers per year are published on boron phosphide.

One of the likely reasons for the dearth of literature regarding boron phosphide is that material synthesis is limited to mainly high temperature CVD processes decomposing phosphine and diborane gases in the presence of H_2 gas.[2,3,5–8] There are some synthesis techniques which do not require high temperatures, however, these processes require catalysts or other non-pure precursors which can unintentionally contaminate or affect the product.[1,9] Molecular beam epitaxy has also been proposed as a potential fabrication technique.[10] Of all these techniques, none have demonstrated production of free-standing BP NCs. The goal of this experiment was to use a nonthermal plasma synthesis technique to decompose diborane and phosphine gases in the presence of H and Ar to form such a material. The following accounts for a single round of preliminary experiments to find plasma conditions which produce BPNCs.

The standard nonthermal plasma synthesis reactor was used, located in the Nanofabrication Facility. A straight, one inch, glass tube was used as the reactor. The phosphine was diluted to 15% in H_2, and the diborane to 10% in H_2, before introduction to reactor tube. It was then mixed with Ar as a carrier gas. The plasma power source was 13.56 MHz rf power supply. The resulting nanoparticle material was impacted on glass substrates. Table BP1 outlines *every* experimental sample and the conditions used to prepare it. The last column of Table BP1 indicates whether or not a powder material was observed as the product of the reaction. Figure BP(a) is a photograph of samples BP1 – BP5 and is annotated with the main synthesis variable that was changed. X-ray diffraction patterns were measured using the samples as is, loaded into a Bruker AXS Microdiffractometer. FITR spectra were measured using a Bruker Alpha FTIR spectrometer in DRIFTS mode. FTIR samples were made by impacting directly from the aerosol phase onto small chips of aluminum coated Si wafer. Samples were exposed to air directly after synthesis, as there was no reason to believe oxidation of BP would be significant. No additional reaction was observed when the samples were exposed.

8.5.2. RESULTS AND DISCUSSION

Under almost all conditions, some sort of powder material was observed to be impacted as a result of the precursor gas decomposition. Only as the conditions started to become B-lean was there little to no observed reaction product. All samples had a slight brown color upon exposure to air, and did not change after several days of ambient exposure. Amorphous B is known to be brown in color. Since BP has a bandgap of approximately 2 eV, NCs of such a material should be almost transparent in nature, neglecting defect absorption. Furthermore, independent experiments show that a PH_3-only plasma will not produce nanoparticles, while a B_2H_6-only plasma will produce. Based on these observations, it is likely that the majority of the experimental conditions resulted in amorphous B nanoparticles. The XRD and FTIR measurements seem to support this conclusion as well. Figure BP(b) shows spectra for a series of samples made under different applied power, and compares those spectra to one from the product of a B_2H_6-only plasma. It is fairly obvious that for high applied power, the BP spectra most match the B_2H_6-only plasma, with significant peaks at 820, 1450, and 2550 cm^{-1}, assigned to B-O stretching, amorphous B-H or B-O, and B_x-H_y stretching, respectively.[11–14] Only at low applied power do some features appear that are different (2400-2500 cm^{-1}), however these

features are likely from additional H in the sample, or reaction of the B with C contamination. The most likely explanation is that additional H exists in the sample, and remains at low applied power because the temperature of the particle does not exceed the H desorption temperature. The apparent oxide content could be from *in situ* etching of the reactor tube from the H plasma, or from ambient exposure, however this would not preclude the formation of crystals. Ambient exposure typically includes the presence of water as observed by –OH stretches in the region of wavenumbers greater than 3200 cm^{-1}, however the absence of any significant absorption in this range tends to suggest the oxide is formed through an *in situ* mechanism instead of through ambient oxidation. Figure BP(c) shows some selected XRD patterns of different sample sets. Under no conditions was any significant amount of crystalline material observed using XRD, as illustrated by the lack of any sharp features in the line pattern.

Unfortunately, none of the experimental conditions produced BP NCs and instead most likely produced amorphous B nanoparticles, possible slightly doped with P. A few comments should be made before proceeding with additional experiments. Because of the dilution of the precursor gases in H_2 prior to injection into the system, the Ar:H ratio is much lower than in other plasma reactions (~4:1 for BP1). The large amount of H in the plasma may be quenching the temperature available to heat and crystallize the particles. Since the precursor dilution is set due to safety considerations, additional experiments may not produce any better results unless the dilution can be modified, or the overall temperature of the plasma increased. In this case, a thermal plasma may be a better choice for synthesizing BP NCs. Nonetheless, interested researchers may want to investigate more B-lean conditions, as these produce less amorphous B nanoparticles, and may eventually lead to stoichiometric BP. Additionally, post-synthesis annealing may be beneficial for crystallizing amorphous particles, and could be accomplished *in situ* with a tube furnace attached to the outlet of the plasma reactor. These considerations were beyond the scope of the preliminary investigations and were not looked into further.

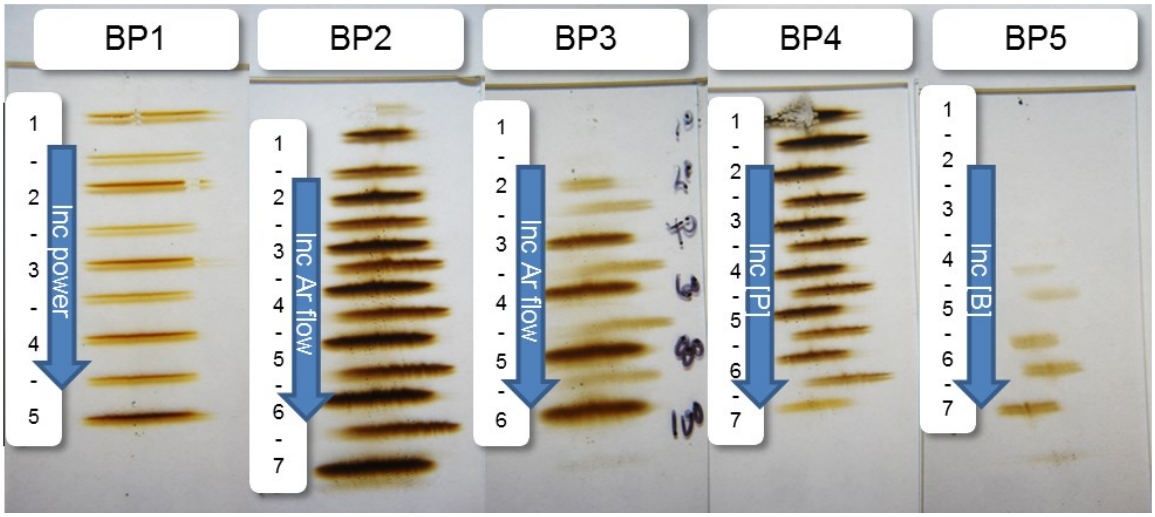

Figure BP(a). Digital photographs of boron phosphide nanoparticles impacted as lines on microscope slide glass for samples sets BP1 – BP5. Each set is labeled with the main synthesis variable. In between lines, powder is collected while the conditions are adjusted. This sacrificial line is ignored in all measurements.

Table BP1. Synthesis conditions for all BP NC trials

Label	Ar flow (sccm)	B_2H_6:H_2 flow (sccm)	PH_3:H_2 flow (sccm)	[B]/[B]+[P]	Power (W)	Deposit time (sec)	NPs observed
BP1-1	20	3	3	57.1%	40	30	yes
BP1-2	20	3	3	57.1%	60	30	yes
BP1-3	20	3	3	57.1%	75	30	yes
BP1-4	20	3	3	57.1%	95	30	yes
BP1-5	20	3	3	57.1%	120	30	yes
BP2-1	0	2	1.5	64.0%	70	60	yes
BP2-2	10	2	1.5	64.0%	120	60	yes
BP2-3	20	2	1.5	64.0%	120	60	yes
BP2-4	30	2	1.5	64.0%	120	60	yes
BP2-5	40	2	1.5	64.0%	120	60	yes
BP2-6	50	2	1.5	64.0%	120	60	yes
BP2-7	60	2	1.5	64.0%	120	60	yes
BP2-8	70	2	1.5	64.0%	120	60	yes
BP3-1	10	1	0.75	64.0%	120	120	yes
BP3-2	20	1	0.75	64.0%	120	120	yes
BP3-3	40	1	0.75	64.0%	120	120	yes
BP3-4	60	1	0.75	64.0%	120	120	yes
BP3-5	80	1	0.75	64.0%	120	120	yes
BP3-6	100	1	0.75	64.0%	120	120	yes
BP4-1	15	2	0	100.0%	120	60	yes
BP4-2	15	2	0.52	83.7%	120	60	yes
BP4-3	15	2	1.01	72.5%	120	60	yes
BP4-4	15	2	1.52	63.7%	120	60	yes
BP4-5	15	2	2.01	57.0%	120	60	yes
BP4-6	15	2	2.52	51.4%	120	60	yes
BP4-7	15	2	3.04	46.7%	120	60	barely
BP5-1	15	0	2.5	0.0%	120	60	no
BP5-2	15	0.25	2.25	12.9%	120	60	no
BP5-3	15	0.5	2	25.0%	120	60	no
BP5-4	15	0.75	1.75	36.4%	120	60	no
BP5-5	15	1	1.5	47.1%	120	60	barely
BP5-6	15	1.25	1.25	57.1%	120	60	yes
BP5-7	15	1.5	1	66.7%	120	60	yes
BP6-1	20	2.2	1.8	62.0%	120	60	yes
BP6-2	20	2.1	1.9	59.6%	120	60	yes
BP6-3	20	2	2	57.1%	120	60	yes
BP6-4	20	1.9	2.1	54.7%	120	60	yes
BP6-5	20	1.8	2.2	52.2%	120	60	yes
BP7-1	20	1.8	2.2	52.2%	135	60	yes
BP7-2	20	1.8	2.2	52.2%	120	60	yes
BP7-3	20	1.8	2.2	52.2%	105	60	yes
BP7-4	20	1.8	2.2	52.2%	90	60	yes
BP7-5	20	1.8	2.2	52.2%	75	60	yes

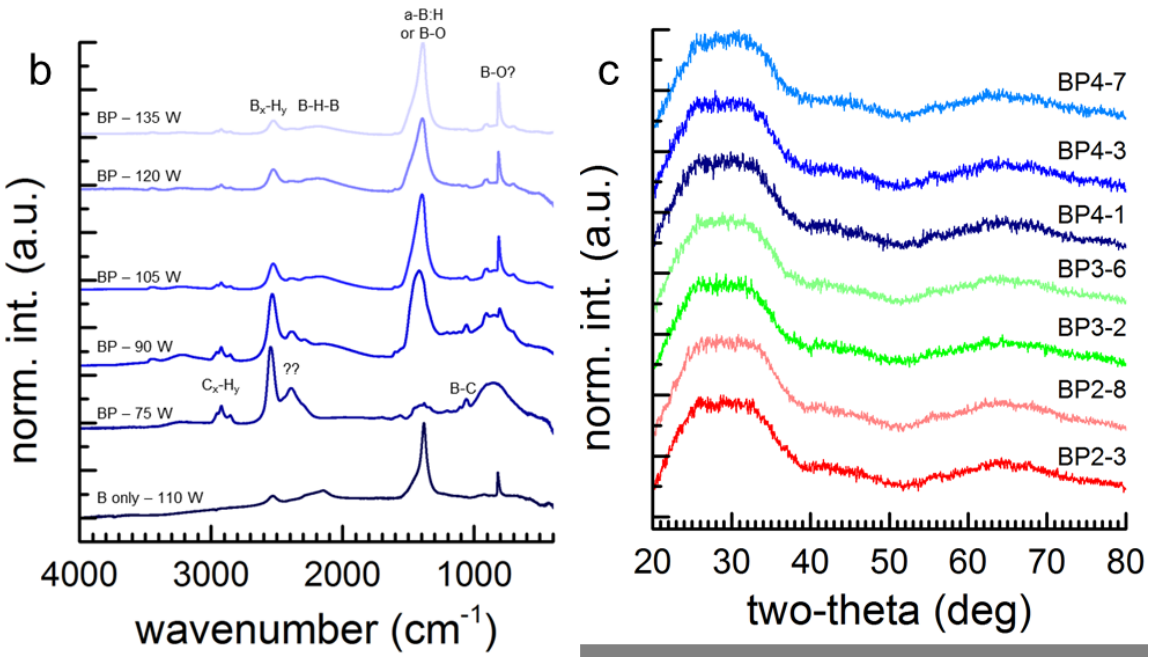

Figure BP(b-c) (b) FTIR spectra (offset for clarity) of samples synthesized with B_2H_6 only ("B only"), and a mixture of B_2H_6 and PH_3 ("BP"). (c) XRD patterns (offset for clarity) for selected samples synthesized with a mixture of B_2H_6 and PH_3.

8.5.3. REFERENCES

(1) Ryan, F. M.; Miller, R. C. *Physical Review* **1966**, *148*, 858–862.

(2) Yugo, S.; Sato, T.; Kimura, T. *Applied Physics Letters* **1985**, *46*, 842.

(3) Kumashiro, K.; Hirata, K.; Sato, K.; Yokoyama, T.; Aisu, T.; Ikeda, T.; Minaguchi, M. *Journal of Solid State Chemistry* **2000**, *154*, 26–32.

(4) Popper, P.; Ingles, T. A. *Nature* **1957**, 1075.

(5) Chu, T. L. *Journal of Applied Physics* **1971**, *42*, 420.

(6) Kumashiro, Y.; Sato, K.; Chiba, S.; Yamada, S.; Tanaka, D.; Hyodo, K.; Yokoyama, T.; Hirata, K. *Journal of Solid State Chemistry* **2000**, *154*, 39–44.

(7) Stone, B.; Hill, D. *Physical Review Letters* **1960**, *4*, 282–284.

(8) Wettling, W.; Windscheif, J. *Solid state communications* **1984**, *50*, 33–34.

(9) Feng, X.; Shi, L.-Y.; Hang, J.-Z.; Zhang, J.-P.; Fang, J.-H.; Zhong, Q.-D. *Materials Letters* **2005**, *59*, 865–867.

(10) Kumashiro, Y.; Yokoyama, T. *Journal of Solid State …* **1997**, *272*, 269–272.

(11) Shin, W. G.; Calder, S.; Ugurlu, O.; Girshick, S. L. *Journal of Nanoparticle Research* **2011**, *13*, 7187–7191.

(12) Buc, D.; Bello, I.; Caplovicova, M.; Mikula, M.; Kovac, J.; Hotovy, I.; Chong, Y. M.; Siu, G. G. *Thin Solid Films* **2007**, *515*, 8723–8727.

(13) Tsai, C. *Physical Review B* **1979**, *19*.

(14) Ong, C.; Chik, K.; Wong, H. K. *Journal of Non-Crystalline Solids* **1989**, *114*, 783–785.